

# **Manipulation of Superconductivity and Charge-Density Wave Formation in the $2H\text{-TaS}_2$ System**

Dissertation

zur

Erlangung der naturwissenschaftlichen Doktorwürde

(Dr. sc. nat.)

vorgelegt der

Mathematisch-naturwissenschaftlichen Fakultät

der

Universität Zürich

Von

**Huanlong Liu**

aus der Volksrepublik China

Promotionskommission

Prof. Dr. Andreas Schilling (Vorsitz)

Prof. Dr. Fabian O. von Rohr

Dr. Hai Lin

Zürich, 2023



# Abstract

At present, the aim of superconductivity research is still expected to provide directions and a theoretical framework for the search for new superconductors, even high-temperature superconductors. Given the difficulty of discovering new superconductors, superconductivity research has focused on the alterations of existing of superconductors and the phases coexisting with superconductivity, such as a charge-density wave (CDW) state. The relationship between superconductivity and CDW has been an important research topic for the detailed understanding of superconductivity. In  $2H$  polytypes of transition metal dichalcogenides (TMDs), the natural CDW and superconductivity coexist without any magnetic order, which provides an ideal platform to further explore the interplay between superconductivity and the CDW state. This thesis presents a systematic study of the  $2H$ -TaS<sub>2</sub> system with the introduction of external atoms and disorder to investigate the CDW state, superconductivity, and their interplay.

In the lithium-intercalated  $2H$ -TaS<sub>2</sub> system, the intercalated lithium can tip the delicate balance between superconductivity and the CDW state, revealing the underlying interactions that give rise to them. The formation of superconductivity and the CDW state has been investigated by electrical and thermal transport properties, in which the CDW formation temperature is continuously suppressed, and the transition temperature of superconductivity ( $T_c$ ) increases with increasing lithium intercalation, indicating that superconductivity and CDW compete with each other in lithium-intercalated  $2H$ -TaS<sub>2</sub>. Furthermore, the electronic contribution to the specific heat and Hall resistivity data further demonstrate that the CDW weakens with lithium intercalation to indirectly increase the charge carrier density and boost superconductivity.

In the hydrated  $2H$ -Li <sub>$x$</sub> (H<sub>2</sub>O) <sub>$y$</sub> TaS<sub>2</sub> system, the intercalated lithium can absorb water into the interlayer of  $2H$ -Li <sub>$x$</sub> TaS<sub>2</sub>. The amount of water is related to the content of the interlayer lithium and remains constant when the lithium content is within a certain range, accompanied by the complete suppression of the CDW state. The superconductivity has been studied by electrical and thermal transport and magnetic properties, showing a dome-shaped dependence on the lithium content  $x$ . The Debye temperatures  $\Theta_D$ , the electron-phonon coupling  $\lambda_{ep}$  and the electron density of states at the Fermi level ( $DOS(E_F)$ ), estimated from the heat capacity data, show a close relationship with the superconductivity, indicating that the lithium intercalation tunes  $T_c$  by changing the  $DOS(E_F)$  in  $2H$ -Li <sub>$x$</sub> (H<sub>2</sub>O) <sub>$y$</sub> TaS<sub>2</sub>, but the simultaneous changes of  $\lambda_{ep}$  and  $\Theta_D$  may also play a certain role.

In the disordered  $2H\text{-TaS}_{2-x}$  system, the level of disorder can be well controlled by the number of structural defects induced by sulphur-vacancies, which influence the evolution of the long-range CDW and superconductivity. Measurements of complementary magnetization, electronic and thermal transport properties show that the long-range CDW is continuously suppressed, leading to strange-metal behaviour with linear resistivity at the endpoint of the long-range CDW, which is accompanied by the emergence of a short-range CDW phase. The superconductivity shows at first a two-step-like behaviour but reaches a maximum at the endpoint of long-range CDW with a single homogeneous phase, suggesting an interplay between superconductivity and CDW order. Moreover, the results suggest that the observed strange-metal behaviour, which could arise from the short-range charge density fluctuations, is a signature of quantum criticality with Planckian dissipation.

# Contents

Abstract .....	I
Chapter 1 Introduction .....	1
1.1 Superconductivity .....	1
1.1.1 A Brief History of Superconductivity .....	1
1.1.2 Meissner-Ochsenfeld effect.....	3
1.1.3 Ginzburg-Landau (GL) Theory .....	5
1.1.4 The Bardeen-Cooper-Schrieffer (BCS) Theory .....	9
1.2 Charge-density waves (CDWs) .....	10
1.2.1 CDW in two-dimensional systems .....	12
1.3 Tantalum disulfide .....	14
1.3.1 Crystal structure .....	14
1.3.2 Interplay between CDW and superconductivity in the $2H$ -TaS <sub>2</sub> system .....	16
1.4 Scope of the thesis .....	23
Chapter 2 .....	24
Experimental Methods and Technology .....	24
2.1 Solid-state synthesis .....	24
2.2 Measurement techniques .....	24
2.2.1 Powder X-ray diffraction (PXRD) .....	24
2.2.2 Thermogravimetric Analysis (TGA).....	25
2.2.3 Scanning Electron Microscope (SEM) and Energy Dispersive X-ray Spectrometer (EDS).....	25
2.2.4 Transmission Electron Microscopy (TEM).....	26
2.2.5 Raman.....	26
2.2.6 Inductively Coupled Plasma Mass Spectrometry (ICP-MS).....	28
2.3 Physical Property Measurement System (PPMS) .....	29
2.3.1 Electrical transport .....	29
2.3.2 Heat capacity .....	31
2.3.3 Magnetism .....	31
Chapter 3 The superconductivity and charge-density wave formation in lithium-intercalated $2H$ -TaS <sub>2</sub> .....	33
3.1 Introduction .....	33
3.2 Experiments .....	34
3.3 Results and discussion .....	34

3.3.1 Characterization of structure .....	34
3.3.2 Electrical transport .....	36
3.3.3 Hall resistivity .....	37
3.3.4 Superconducting characteristic parameters .....	39
3.3.5 Heat capacity .....	41
3.4 Summary.....	42
3.5 Related Publication.....	43
Chapter 4 Superconductivity in hydrated $\text{Li}_x(\text{H}_2\text{O})_y\text{TaS}_2$ .....	44
4.1 Introduction .....	44
4.2 Experiments .....	45
4.3 Results and discussion .....	45
4.3.1 Crystal structure .....	45
4.3.2 Electrical transport and magnetism .....	47
4.3.3 Superconducting characteristic parameters .....	49
4.3.4 Heat capacity .....	52
4.3.5 Discussion .....	54
4.4 Summary.....	55
4.5 Related Publication.....	55
Chapter 5 Signatures of a charge-density wave quantum-critical point in superconducting $2H\text{-TaS}_{2-x}$ induced by disorder.....	56
5.1 Introduction .....	56
5.2 Experiments .....	58
5.3 Characterization of Structure.....	58
5.4 Transport measurements.....	62
5.5 Raman measurements .....	65
5.6 Heat capacity .....	67
5.7 Electronic phase diagram.....	69
5.8 Summary.....	73
Chapter 6 Conclusion .....	74
Bibliography.....	76
Publication List .....	93
Curriculum Vitae.....	94
Acknowledgments.....	95

# Chapter 1

## Introduction

Condensed matter physics deals with the macroscopic and microscopic physical properties of matter. In particular, it is concerned with the condensed phase of materials, which occurs whenever the number of constituents in a system is extremely large and the interactions between the constituents are strong. According to P. W. Anderson, the description of the properties of materials is based on two principles: The principle of adiabatic continuity and the principle of spontaneously broken symmetry[1]. Adiabatic continuity means that a complicated system can be replaced by another simpler system and retain the same essential properties, for example Landau's Fermi liquid theory[2]. On the other hand, phase transitions to states with qualitatively different properties can often be characterized by broken symmetries. A representative charge density wave (CDW), for example, is an ordered state that breaks translational symmetry, often inducing a metal-insulator transition[3, 4]. Alternatively, when the electron-electron pairing mediated by a "glue" condenses to the same quantum ground state and gives rise to superconductivity, global gauge symmetry is absent[5, 6]. In this thesis I focus on the study of superconductivity and CDW formation and their interplay with each other. Therefore, a brief broad overview of some background concepts will be introduced here.

## 1.1 Superconductivity

### 1.1.1 A brief history of superconductivity

Superconductivity was discovered in 1911 by Heike Kamerlingh Onnes at the University of Leiden in the Netherlands. He observed that the electrical resistance of mercury (Hg) was zero when the temperature was cooled below 4.2 K (Fig. 1.1a)[7, 8]. Since then, the door to superconductivity has been opened. After 40 years, in 1957, the well-known Bardeen-Cooper-Schrieffer (BCS) theory was proposed to explain the phenomena of superconductivity, which involves a pairing between electrons (Cooper pairs) induced by electron-phonon interactions[9]. Disappointingly, according to the McMillan limit[10], the Cooper pair in the BCS framework can only survive temperatures below 40 K. After three-decades-long unsuccessful search for elevated-temperature superconductivity, the high-temperature superconducting material with  $T_c \sim 35$  K,  $\text{La}_{2-x}\text{Ba}_x\text{CuO}_4$ , was discovered in 1986 by K. A. Müller and J. G. Bednorz (Fig. 1.1b)[11], which further promoted the development of superconductivity, and the era of high-temperature superconductors began. This important discovery leads to a whole family of high-

temperature superconductors, the so-called cuprate or copper-oxide superconductors, which share one or several  $\text{CuO}_2$  layers as a common structural feature and consist of conducting Cu-O layers and interlayered charge-storage layers[12]. Within a year, the  $T_c$  was rapidly increased to  $\sim 90$  K in the system by Wu et al.[13], above the boiling temperature of nitrogen ( $\sim 77$  K), allowing for potential large-scale applications. To date, the highest atmospheric superconductivity of all known superconductors has been pushed to  $\sim 133$  K by Prof. Andreas Schilling et al. in the compound  $\text{HgBa}_2\text{Ca}_2\text{Cu}_3\text{O}_8$ [14]. In 2008, a new superconductor was found in  $\text{LaFeAsO}_{1-x}\text{F}_x$  with  $T_c \sim 26$  K by Kamihara et al.[15], and the  $T_c$  was also promoted up to 55 K in  $\text{SmFeAsO}_{0.85}\text{F}_{0.15}$ [16, 17], which aroused great research interest in the iron-based superconductors and added a new system to the family of high-temperature superconductors. Recently, a landmark discovery of superconductivity was reported in  $\text{Nd}_{0.8}\text{Sr}_{0.2}\text{NiO}_2$  films with  $T_c$  in the range of 9-15 K[18]. This discovery of superconductivity has motivated researchers to search for other nickelate superconductors with higher  $T_c$  and to compare them with cuprate superconductors. Indeed, superconductivity has been reported in single crystals of  $\text{La}_3\text{Ni}_2\text{O}_7$  with a maximum  $T_c$  of  $\sim 83$  K under physical pressure[19], providing a new family of compounds to investigate the mechanism of high-temperature superconductivity.

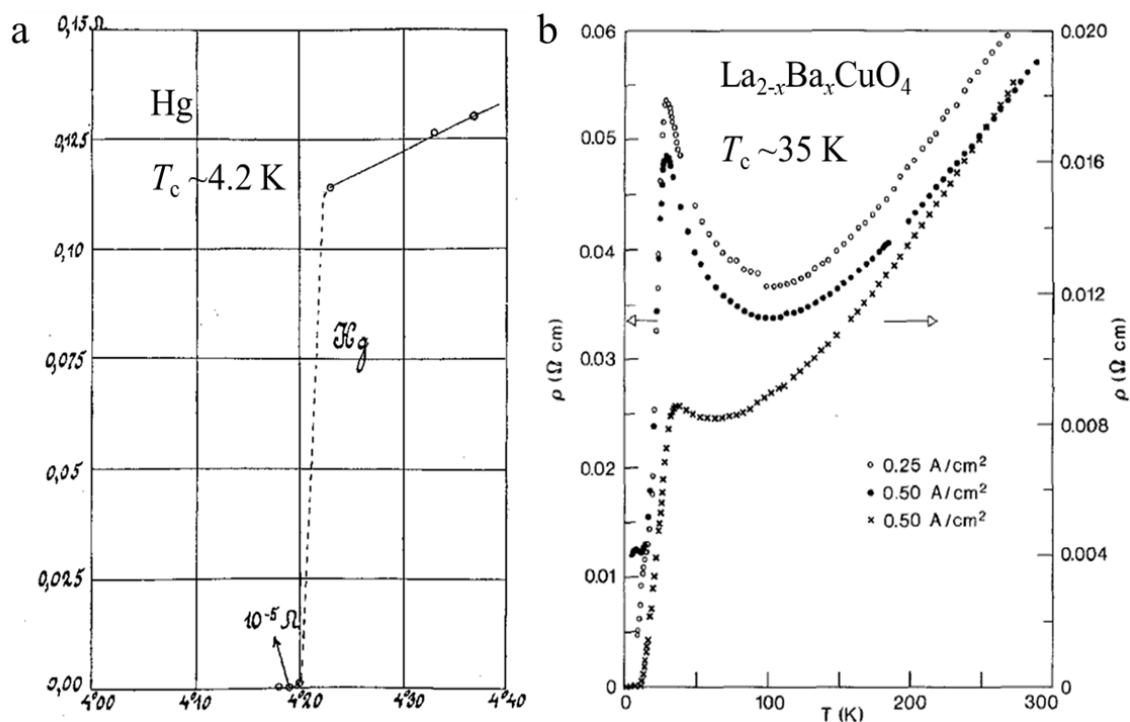


Fig. 1.1 (a) The first observation of superconductivity by measuring the resistivity of Mercury[8]. (b) Temperature-dependent resistivity of the first of a new class of high-temperature superconductors[11]. Both were the most important milestones in superconductivity and were awarded with Nobel Prizes.



### 1.1.2 Meissner-Ochsenfeld effect

For a superconductor, apart from the zero-resistance state (the resistivity  $\rho = 0$ ), the second important characteristic is the Meissner-Ochsenfeld effect, discovered by W. Meissner and R. Ochsenfeld in 1933[20]. The ideal experimental processes are shown in Fig. 1.2. For a material in a magnetic field, it enters the superconducting state once the temperature drops to  $T_c$  and the magnetic flux cannot enter inside of a superconductor. As a superconductor in a magnetic field is cooled below  $T_c$ , the magnetic flux within the material is completely expelled. If the magnetic field is below a critical field  $B_c$ , a superconductor exhibits perfect diamagnetism. The external magnetic field may be made so strong, however, that it prevents a transition to the superconducting state, and the Meissner-Ochsenfeld effect does not occur.

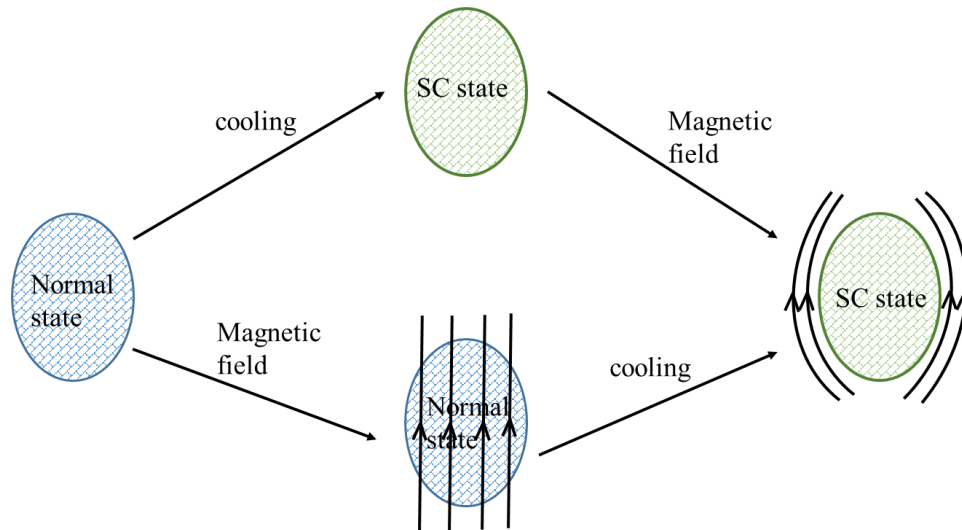


Fig.1.2 Schematic diagram of the Meissner-Ochsenfeld effect (SC = superconducting).

The magnetic flux or induction  $\mathbf{B}$  of a material is defined as

$$\mathbf{B} = \mu_0(\mathbf{H} + \mathbf{M}), \quad (1-1)$$

where  $\mu_0$  is the permeability of the vacuum, and  $\mathbf{H}$  is the applied magnetic field. The magnetization  $\mathbf{M}$  can be expressed by

$$\mathbf{M} = \chi\mathbf{H}, \quad (1-2)$$

where  $\chi$  is the magnetic susceptibility. These two equations (1-1) and (1-2) give the relationship

$$\mathbf{B} = \mu_0\mathbf{H}(1 + \chi). \quad (1-3)$$

The  $\chi$  is -1 for a perfectly diamagnetic superconductor and corresponds to  $\mathbf{B} = 0$  inside the superconductor.

### 1.1.3 London theory

In 1935, F. London and H. London gave the first theoretical description of the behaviour of a superconductor in a magnetic field[21]. For a perfect conductor with  $\rho = 0$ , the motion of the supercurrent carriers obeys classical mechanics with mass  $m$  and charge  $e$  in the presence of an electric field  $\mathbf{E}$ ,

$$m \frac{\partial}{\partial t} \mathbf{v}_s = e\mathbf{E}, \quad (1-4)$$

where  $\mathbf{v}_s$  is the velocity of the superconducting carriers. Here we assume that the electron mass remains the same during the transition from the normal to the superconducting state of a material. The magnetic field induced supercurrent density  $\mathbf{j}_s$ , which couples to the local density of superconducting carriers  $n_s$ , can be estimated to

$$\mathbf{j}_s = n_s \mathbf{v}_s e. \quad (1-5)$$

Substituting into equation (1-4) gives

$$\frac{\partial}{\partial t} \mathbf{j}_s = \frac{n_s e^2}{m} \mathbf{E}, \quad (1-6)$$

which is known as the "first London equation". The above equation (1-6) can be rewritten as

$$\nabla \times \frac{\partial}{\partial t} \mathbf{j}_s = \left( \frac{n_s e^2}{m} \right) \nabla \times \mathbf{E}. \quad (1-7)$$

Since  $\nabla \times \mathbf{E} = -\partial \mathbf{B} / \partial t$  based on Maxwell's laws, the equation (1-7) can be rewritten as

$$\left( \frac{m}{n_s e^2} \right) \nabla \times \frac{\partial}{\partial t} \mathbf{j}_s + \frac{\partial}{\partial t} \mathbf{B} = 0. \quad (1-8)$$

So,

$$\left( \frac{m}{n_s e^2} \right) \nabla \times \mathbf{j}_s + \mathbf{B} = 0. \quad (1-9)$$

This is the "second London equation". Inside a superconductor, the relationship between  $\mathbf{j}_s$  and the magnetic field can be described by another Maxwell equation

$$\nabla \times \mathbf{B} = \mu_0 \left( \mathbf{j}_s + \frac{\partial}{\partial t} \mathbf{D} \right). \quad (1-10)$$

The displacement current density  $\frac{\partial \mathbf{D}}{\partial t}$  is ignored compared to  $\mathbf{j}_s$  due to the weak change of the magnetic field with time.

Therefore, by setting  $\lambda_L = (m/\mu_0 m_s e^2)^{1/2}$ , the above equations become

$$\lambda_L^2 (\nabla \times \nabla \times \mathbf{B}) + \mathbf{B} = 0. \quad (1-11)$$

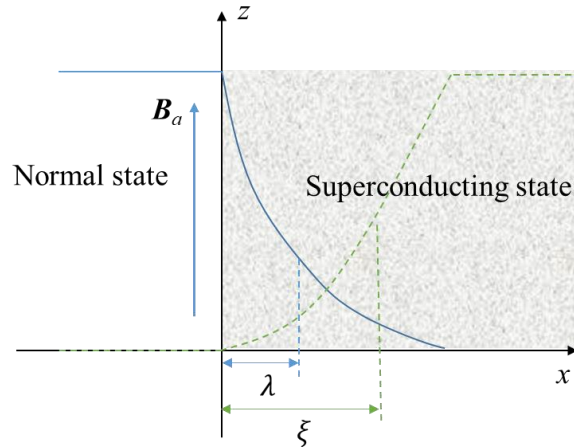


Fig. 1.3 A superconducting slab in an external field.

To further illustrate the variation of  $\mathbf{B}$  at the superconductor interface, consider a semi-infinite superconductor with a planar interface in Fig. 1.3, and the above equation can be transformed to

$$\mathbf{B}(x) = \mathbf{B}(0) \exp(-x/\lambda_L), \quad (1-12)$$

where  $\mathbf{B}(0)$  is the magnetic flux outside the superconductors. This equation indicates that the magnetic flux  $\mathbf{B}$  inside the superconductors decays exponentially with  $x$ . The corresponding relationship between  $\mathbf{j}_s$  and  $\mathbf{B}$  is also given by

$$\mathbf{j}_s = \frac{\mathbf{B}(0)}{\mu_0 \lambda_L} \exp(-x/\lambda_L). \quad (1-13)$$

This means that the superconducting current flows close to the surface of the superconductor within  $\lambda_L$ .

### 1.1.3 Ginzburg-Landau (GL) Theory

In 1950, L. D. Landau and V. L. Ginzburg [22] proposed a more general theory of superconductivity, which is still used today. The phenomenological GL theory further describes the physical properties of superconductors, which are characterized by a complex order

parameter  $\psi$ . This theory assumes that the superconducting current is carried by superconducting electrons of mass  $m^*$ , charge  $e^*$ , and density  $n_s$ , where  $m^* = 2m$ ,  $e^* = 2e$ , and  $n_s = 2n$  in terms of the free electron values  $m$ ,  $e$ , and  $n$ , respectively. In addition, the order parameter  $\psi$  to describe the superconducting electron is defined as  $n_s = |\psi|^2 = \psi^*\psi$ , which goes to zero at the transition temperature  $T_c$ . The free energy  $F$  can be expanded in powers of  $\psi$ ,

$$F = F_n + \alpha(T)|\psi|^2 + \frac{\beta(T)}{2} |\psi|^4 + \dots \quad (1-14)$$

where the order parameter  $\psi$  is a constant throughout the sample. If  $\psi$  has a spatial variation, then the spatial derivative of  $\psi$  must be added to the above equation, thus

$$F_s = F_n + \alpha(T)|\psi|^2 + \frac{\beta(T)}{2} |\psi|^4 + \frac{1}{2m^*} |-i\hbar\nabla\psi + e^*\mathbf{A}\psi|^2 + \frac{|\mathbf{B}|^2}{2\mu_0}, \quad (1-15)$$

where  $F_n$  is the Helmholtz free energy density in the normal state;  $\alpha$  and  $\beta$  are material dependent phenomenological parameters to be determined experimentally;  $\mathbf{A}$  is the vector potential related to the applied magnetic field  $\mathbf{B}$ . The free energy differences between normal and superconducting states as a function of the order parameter are illustrated in Fig. 1.4.

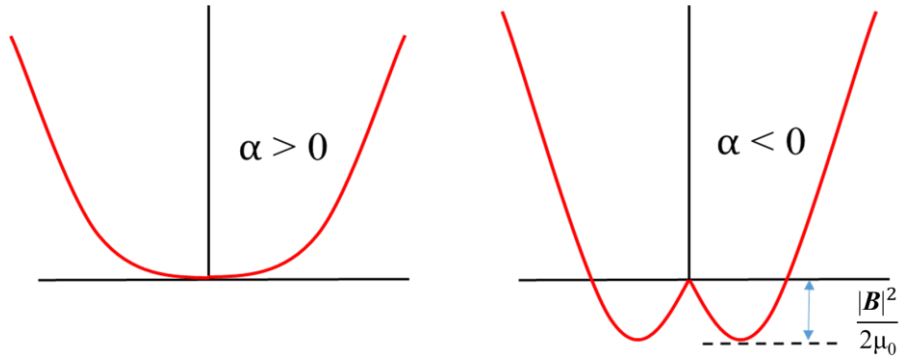


Fig. 1.4 GL free-energy function when  $T > T_c$  ( $\alpha > 0$ ) and when  $T < T_c$  ( $\alpha < 0$ ).

In the stable state, the GL equation can be derived by minimizing the variation of the free energy with  $\psi$  and  $\mathbf{A}$

$$\frac{1}{2m^*} (-i\hbar\nabla - e^*\mathbf{A})^2\psi + \alpha(T)\psi + \beta(T)|\psi|^2\psi = 0 \quad (1-16)$$

and,

$$\mathbf{j}_s = \frac{-ie^*\hbar}{2m^*} (\psi^*\nabla\psi - \psi\nabla\psi^*) - \frac{e^{*2}}{m^*} |\psi|^2\mathbf{A}. \quad (1-17)$$

These are called the GL equations.

To obtain the analytical solution in the interface between the superconducting and normal states, suppose the interface is shown in Fig. 1.3 with the metallic region at  $x < 0$  and the superconducting region at  $x > 0$ . In zero magnetic field,  $\mathbf{B}$  inside a superconductor is zero, i.e.  $\mathbf{A} = \nabla \times \mathbf{B} = 0$ . The first GL equation can then be written as

$$\frac{\hbar^2}{2m^*} \nabla^2 \psi + \alpha(T)\psi + \beta(T)|\psi|^2\psi = 0. \quad (1-18)$$

By setting  $f = \psi/\psi_0$ , where  $|\psi|^2 = -\alpha(T)/\beta(T) > 0$ , the above equation (1-18) can be rewritten as

$$\xi^2(T)\nabla^2 f + f - f^3 = 0. \quad (1-19)$$

With the coherence length  $\xi(T)$  is defined as

$$\xi^2(T) = \frac{\hbar^2}{2m^*|\alpha(T)|}. \quad (1-20)$$

For semi-infinite superconducting samples, with the boundary conditions  $x \rightarrow \infty, f \rightarrow 1$  and  $f \rightarrow 0$  for  $x \rightarrow 0$ , the solution is

$$f(x) = \frac{\psi(x)}{\psi_0} = \tanh \frac{x}{\sqrt{2}\xi(T)}. \quad (1-21)$$

In addition, in a weak magnetic field,  $\psi \approx \psi_0$ . From the second GL equation, it can be obtained

$$\lambda_0^2 = -\frac{m^*}{\mu_0 e^{*2} \psi_0^2} \quad (1-22)$$

with  $\mathbf{j}_s = -\nabla^2 \mathbf{A} = \frac{1}{\lambda_0^2} \mathbf{A}$ .

Ginzburg and Landau introduced a dimensionless parameter  $\kappa$ , which is independent of temperature and is defined as

$$\kappa = \frac{\lambda(T)}{\xi(T)}. \quad (1-23)$$

This  $\kappa$  was used by A. Abrikosov to classify superconductors into two types, distinguished by the surface energy of the superconductor-normal state interface, which is positive for  $\kappa < 1/2$  and negative for  $\kappa > 1/2$ , while the surface energy vanishes for materials with the Ginzburg-Landau parameter  $\kappa = 1/2$ , called type-I and type-II superconductors, respectively.

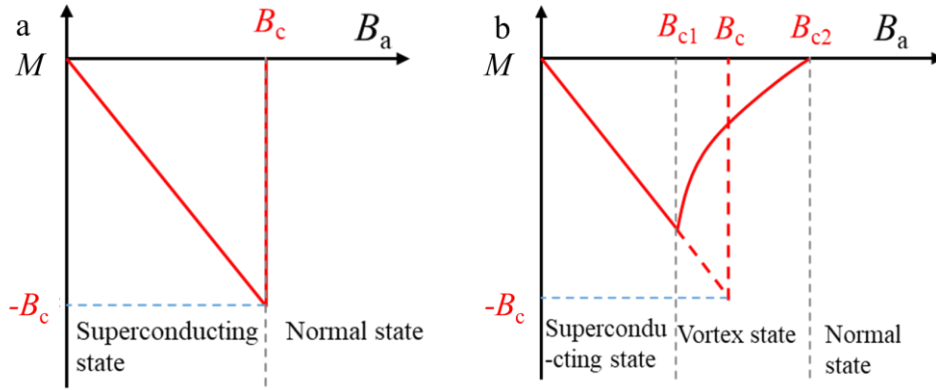


Fig. 1.5 Magnetization curves of type-I and type-II superconductors. (a) Magnetization  $M$  as a function of applied magnetic field  $B_a$  for a type-I superconductor. Perfect diamagnetism is destroyed suddenly at critical field  $B_c$ . (b) Dependence of the magnetization  $M$  on the applied magnetic field  $B_a$  for a type-II superconductor. The specimen is in its vortex states between the lower critical field  $B_{c1}$  and upper critical field  $B_{c2}$ .  $B_c$  is the thermodynamic critical field.

The difference between them can be characterized by their magnetic behaviour. In Fig. 1.5, for a type-I superconductor, the external magnetic field  $B_a$  is excluded outside the superconductor until the superconducting state disappears at  $B_c$ . Above  $B_c$ , the superconductor is in its normal state (Fig. 1.5a). In a type-II superconductor, the material is in the Meissner state below a lower critical field  $B_{c1}$ . When the magnetic field is increased above  $B_{c1}$ , the magnetic field starts to penetrate the interior of the superconductor in form of normal conducting domains containing magnetic flux, called vortices, resulting in the reduction of perfect diamagnetism. The Cooper pairs still exist and the zero-resistance state is still maintained. This state is known as the mixed state. When the  $B_a$  is further increased to an upper critical field  $B_{c2}$ , the complete penetration of the flux leads to the destruction of the zero-resistance state and the superconductor reverts to the normal state. The critical fields are temperature-dependent are

$$B_{c1} = \Phi_0 \ln k / 4\pi\lambda^2, \quad (1-24)$$

$$B_{c2} = \Phi_0 / 2\pi\xi^2, \quad (1-25)$$

$$B_c = \Phi_0 / 2\sqrt{2}\pi\lambda\xi, \quad (1-26)$$

where  $B_c$  is the thermodynamic critical field and  $\Phi_0$  is the flux quantum ( $\Phi_0 = h/2e \approx 2.067 \times 10^{-15}$  Wb).

### 1.1.4 The Bardeen-Cooper-Schrieffer (BCS) Theory

In the BCS theory [9], electron-electron pairing are formed due to the attractive interaction between electrons mediated by lattice vibrations (phonons). As an electron moves through the lattice, it causes a local lattice distortion due to Coulomb interactions. As another electron passes, it is affected by the lattice distortion induced by the first electron, resulting in an indirect attractive interaction between these two electrons mediated by the polarization of the lattice. The resulting "Cooper pair" is composed of two electrons with opposite momenta and spins,  $\{\vec{p}_\uparrow, -\vec{p}_\downarrow\}$ . All Cooper pairs retain the same total momentum due to phase coherence, even when scattered by impurities etc. They can therefore be moved without loss of energy under the action of an applied electric field. At temperatures below  $T_c$ , a significant number of "Cooper pair" condense into a collective quantum state. This condensation leads to the opening of an energy gap in the electronic excitation spectrum, which prevents electrons from scattering and colliding with impurities or lattice defects, resulting in a zero electrical resistance.

BCS theory predicts a second-order phase transition at the transition to superconductivity and a value of  $T_c$  as

$$T_c = \theta_D \exp\left[-\frac{1}{N(0)V}\right], \quad (1-27)$$

which can also be rewritten as

$$T_c = \frac{\theta_D}{1.45} \exp\left[-\frac{1.04(1+\lambda)}{\lambda - \mu^*(1+0.62\lambda)}\right], \quad (1-28)$$

where  $\theta_D$  is the Debye temperature. The  $\mu^*$  is a "renormalized" Coulomb repulsion and  $\lambda$  the electron-phonon coupling constant  $\lambda = N(0)V + \mu^*$ [23, 24] with  $V$  the electron-phonon interaction, and the bare density of states  $N(0)$  known from quasiparticle band theory.

The superconducting gap  $\Delta$  near zero temperature is

$$2\Delta = 3.5 k_B T_c. \quad (1-29)$$

This ratio is predicted to be universal for all superconductors. Close to  $T_c$ , the gap can be expressed as[25]

$$\Delta = 3.2 k_B T_c [1 - (T/T_c)]^{1/2} \quad (1-30)$$

using the mean-field approximation and assuming that the superconductor is weakly coupled.

## 1.2 Charge-density waves (CDWs)

In a physical system, the stability of the system is closely related to the stability of equilibrium. Typically, stable equilibrium states are immune to weak fluctuations, whereas unstable states are very sensitive to external or internal fluctuations. However, if a ground state becomes unstable due to a change in the survival environment, the system will attempt to assume a completely new stable state. A CDW ground state, which develops in low-dimensional metals as a consequence of electron-phonon interactions, is a broken symmetry state of metals[26]. The driving force behind the CDW instability is the reduction of the energy of the electrons in the material due to the establishment of a spontaneous periodic modulation of the crystal lattice[3, 27].

In the one-dimensional model, the simplest form of the CDW state can be understood intuitively through Peierls theory [28]. A one-dimensional homogeneous chain of atoms is shown in Fig.1.6a. The Fermi surface of one-dimensional lattice is not stable at zero temperature due to its geometry and lattice deformation. Considering an one-dimensional lattice with spacing  $a$  and the charge density  $\rho(x)$  is uniform at zero temperature. If there are no particle interactions, the ground state is defined by electrons filled half of the band to Fermi energy  $E_F$  with Fermi wave vector  $k_F = \pm\pi/2a$ . The empty states above the Fermi energy suggest the metallic conductance of the lattice. However, the one-dimensional chain of atoms is unstable at low temperatures, resulting in a lattice distortion if coupling to the underlying lattice (electron-phonon interactions) is considered when the temperature drops below a temperature  $T_{CDW}$ . A periodic lattice distortion takes place which induces a periodic modulation of the electron density (see bottom of Fig. 1.6b). As the two neighbouring atoms move closer together, the period of the lattice becomes doubled[29]. At the points  $k_F = \pm\pi/2a$ , a band gap opens at the Fermi boundary (top of Fig. 1.6b), lowering the energy of the occupied electron states and raising the energy of the empty states, leading to a phase transition from the metallic to the insulating states, called the Peierls transition[30]. The CDW wavelength  $\lambda$  is related to the Fermi wave vector  $k_F$ ,  $\lambda = \pi/k_F$ . The total energy of the distorted electronic system decreases, so the system tends to be stable. This lattice distortion leads to the breaking of the original symmetry of the system, inducing a periodic distribution of the charge density in the system to form the CDW. It can be described by

$$\rho(x) = \rho_0 + \rho_1 \sin(2k_F x + \varphi), \quad (1-32)$$



where  $\rho_0$  is the unperturbed electron density, and  $\rho_1$ ,  $k_F$  and  $\varphi$  are the amplitude, wavevector and phase of the electron density modulation, respectively[31].

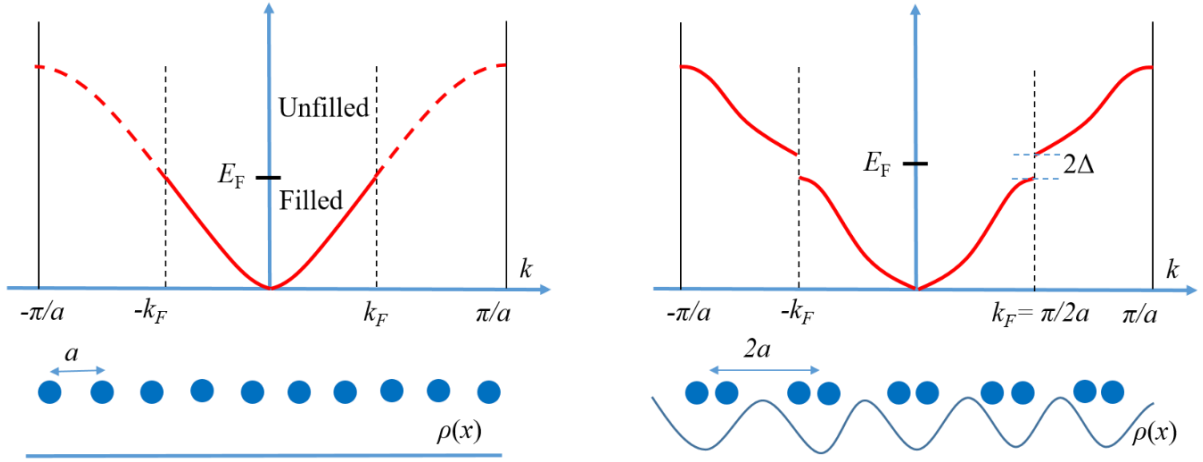


Fig. 1.6 The single particle energy band for the cases (a) when  $T > T_{CDW}$ , the electron and the phonon systems are not coupled, the resulting ions are equally spaced and the charge density is represented by a constant  $\rho(x)$ . (b) When  $T < T_{CDW}$ , the electron and phonons are interacting and the competition between the elastic and electronic energies leads to a static lattice deformation and periodically modulated charge density.

The Peierls transition results from the Kohn anomaly induced by the nesting of Fermi surfaces, where one part of the Fermi surface can completely coincide with another part of the Fermi surface after a certain translation transformation[32]. The nested Fermi surface is unstable, as the corresponding electrons can be excited by the phonons with a wavevector of  $2k_F$  and the phonons acquire a lower frequency, resulting in a phonon softening of the system (Fig. 1.7b). As the temperature reaches the CDW phase transition temperature ( $T_{CDW}$ ), the renormalized phonon frequency at  $2k_F$  decreases to zero[33]. The equilibrium of the system is broken, resulting in a stable distortion. The nesting of the Fermi surface is generally reflected by the Lindhard response function:

$$\chi(q, \omega) = \sum_k \frac{f_k - f_{k+q}}{\varepsilon_k - \varepsilon_{k+q} + \hbar\omega}, \quad (1-33)$$

where  $f_k = f_{\varepsilon_k}$  is the Fermi function. The  $\varepsilon_k$  is the electron energy located at the  $k$  point. The Lindhard response function describes the linear change of the induced charge density at different wavevectors with the applied perturbation potential field. The real part reflects the stability of the electronic system, which varies with the different dimensions in Fig. 1.7a.

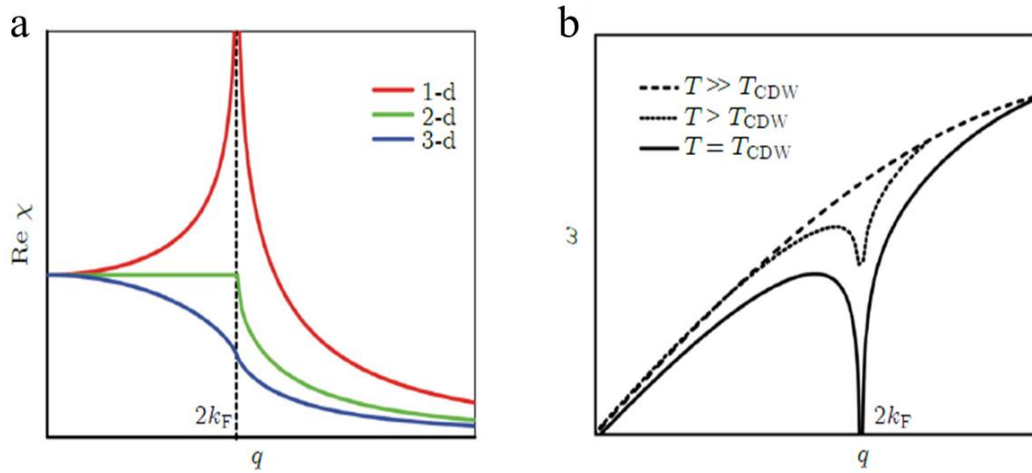


Fig. 1.7 (a) Real part of the Lindhard function for 1D, two-dimensional (2D) and three-dimensional (3D) free electron gas models; (b) process of phonon softening at  $2k_F$ . The data are taken from Ref.[33].

### 1.2.1 CDW in a two-dimensional system

In two-dimensional materials, the origin of the CDW is complicated and controversial due to the complex lattice and electronic structures, including electron-phonon coupling[34], Jahn-Teller effect [35], excitons, etc.[36]. In some two-dimensional materials, the nesting of the Fermi surfaces is due to parallel nearly straight parts of the Fermi surface in the band structure, consistent with Peierls theory, such as in monolayer  $VSe_2$ [37] (Figs. 1.8a-b). In transition metal dichalcogenides (TMDs), the CDW phase transition is not fully consistent with the Peierls phase-transition scenario, especially in the  $2H$  phase[38], including  $2H-TaS_2$ ,  $2H-TaSe_2$ ,  $2H-NbS_2$  and  $2H-NbSe_2$ . The electrical transport shows metallic behaviour, not an insulating state below  $T_{CDW}$ , only the resistivity increases slightly[39-43], although angle-resolved photoemission spectroscopy (ARPES) confirms that the Fermi surface has a certain nesting feature, indicating that the CDW could be explained by Peierls theory[44]. The results of the Lindhard response function  $\chi(q, \omega)$  also show that although the nesting of the Fermi surface is present, the peak is not consistent with the position of the CDW wavevector induced by the nesting of the Fermi surface[45]. Near the CDW wavevector, the real part of the response function has a weak peak, while the imaginary part disappears, which is not consistent with the traditional Peierls phase transition characteristics. The fact that the peak of the real part is not strong enough to excite the CDW, suggests that the nesting of the Fermi surface is not the main factor[46]. Inelastic X-ray scattering experiments in  $2H-NbSe_2$  confirm that the phonon energy at the CDW wave vector decays to zero, leading to a lattice distortion[47]. However, in contrast to the dispersive peak of the Kohn anomaly, the phonon exhibits an overdamped state

in the region near the CDW wavevector (Fig. 1.8c), indicating the electron-phonon coupling that drives the formation of the CDW.

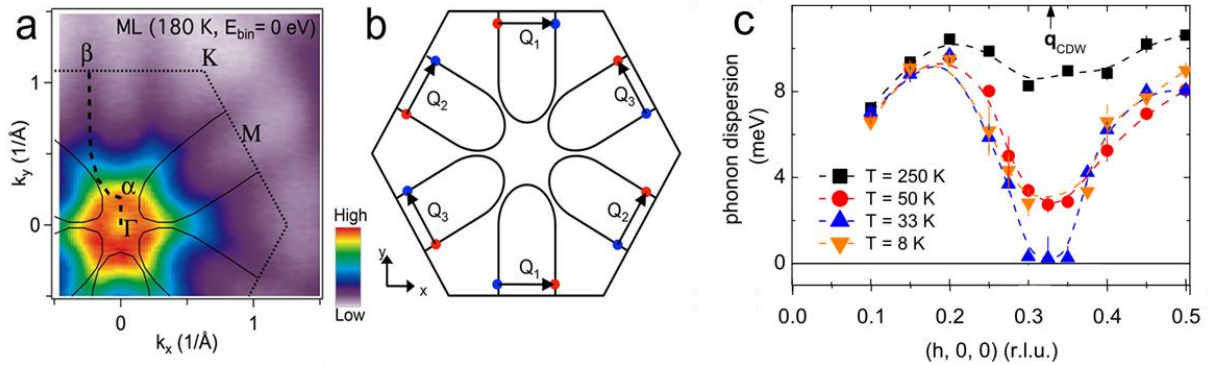


Fig. 1.8 Several mechanisms of CDW transitions: (a) Fermi surface map of monolayer VSe<sub>2</sub> measured by ARPES [37]. (b) Perfect Fermi surface nesting of monolayer VSe<sub>2</sub> [37]. (c) Phonon softening in 2H-NbSe<sub>2</sub> at different temperatures induced by electron-phonon coupling, measured by inelastic X-ray scattering[47].

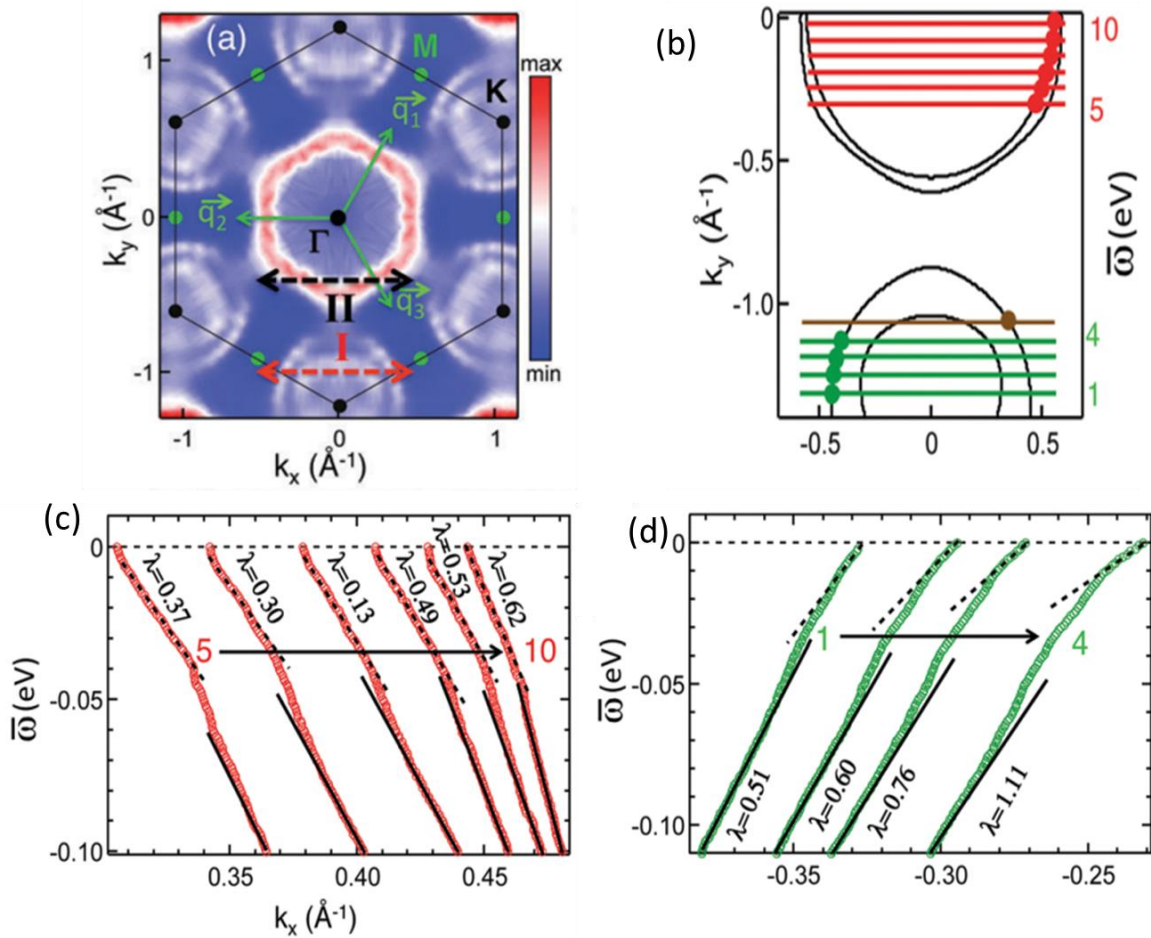


Fig. 1.9 (a) Schematic plots of  $\Gamma$ - and  $K$ -centered Fermi surface sheets. The green and red solid lines show the momentum lines along which the momentum distribution curves constructed to extract the dispersions in (b) and (c). The data are taken from Ref. [44].

Among the family of TMDs,  $2H$ -TaS<sub>2</sub> is considered a prototypical incommensurate CDW material, where the signature of the CDW order has been confirmed by various experiments. Figure 1.9a shows the Fermi surface topology of  $2H$ -TaS<sub>2</sub> in the normal state, from the ARPES data at  $\varpi = 0$ , as a function of the in-plane momentum components  $k_x$  and  $k_y$ , where  $\varpi$  is the electronic energy measured with respect to the chemical potential[44]. The double-walled Fermi surface barrels can be observed around the  $\Gamma$  and K points, which is due to the presence of two formula units per unit cell. In addition, although the Fermi surface of  $2H$ -TaS<sub>2</sub> has a number of nearly parallel regions, their separation is not consistent with the magnitude of the  $\mathbf{q}_{\text{CDW}}$ . For example, the two Fermi surface sheets around the  $\Gamma$  point are too large to be nested by any of the three primary CDW wave vectors  $\mathbf{q}_1$ ,  $\mathbf{q}_2$  and  $\mathbf{q}_3$ . Therefore, simple Fermi surface nesting cannot drive the CDW phase transition in  $2H$ -TaS<sub>2</sub>. In Figs. 1.9b-d, the band dispersions along the K-centered outer Fermi surface sheet and the  $\Gamma$ -centered inner Fermi surface sheet indicate that the CDW transition is rooted in momentum-dependent electron-phonon coupling and that orbital selectivity plays an important role[47, 48].

## 1.3 Tantalum disulfide

### 1.3.1 Crystal structure

TMDs are a class of materials that exhibit interesting electronic and optical properties, and their crystal structure plays a crucial role in determining these properties. They are composed of transition metals (T) and chalcogen atoms (X), typically sulfur (S), selenium (Se), or tellurium (Te) (Fig. 1.10a)[49, 50]. The most common TMDs are TX<sub>2</sub> compounds, which have a unique structure of X-T-X form, a sheet of transition metal atoms in a hexagonal pattern surrounded on adjacent sides by two similar chalcogen sheets. The intralayer bonds between the elements are covalent, while the interlayer bonds between adjacent layers are weak van der Waals forces. The structural phases can also be viewed in terms of the different stacking orders of the three atomic planes (X-T-X) that form the individual layers of these materials in the lattice along the  $c$  axis. The two common thermodynamically stable phases are characterized by either trigonal prismatic ( $2H$ ) or octahedral ( $1T$ ) coordination of the metal atoms (Fig. 1.10b)[51-53]. There are several other ways of stacking the X-T-X, referred to as  $3R$ ,  $4H_b$  and  $6R$ [54-56], showing different physical properties, respectively (Table 1.1). The first number in this notation refers to the number of X-T-X layers in the unit cell, while  $T$ ,  $H$  and  $R$  distinguish the trigonal, hexagonal and rhombohedral symmetry of the structure. Sometimes a subscript is required to further distinguish similar polytypes[57, 58]. In the example of TaS<sub>2</sub>, the  $2H$  phase corresponds

to an S-Ta-S stacking in which the S atoms occupy the same position in different atomic planes and are superimposed in the direction perpendicular to the layer. The Ta atoms are surrounded by six S atoms to form a  $[\text{TaS}_6]$  triangular prism, and neighbouring  $[\text{TaS}_6]$  triangular prisms are connected by edge-sharing in Fig. 1.10b. Details of the crystal data, data collection and structure refinement are summarized in Table 1.2[59].

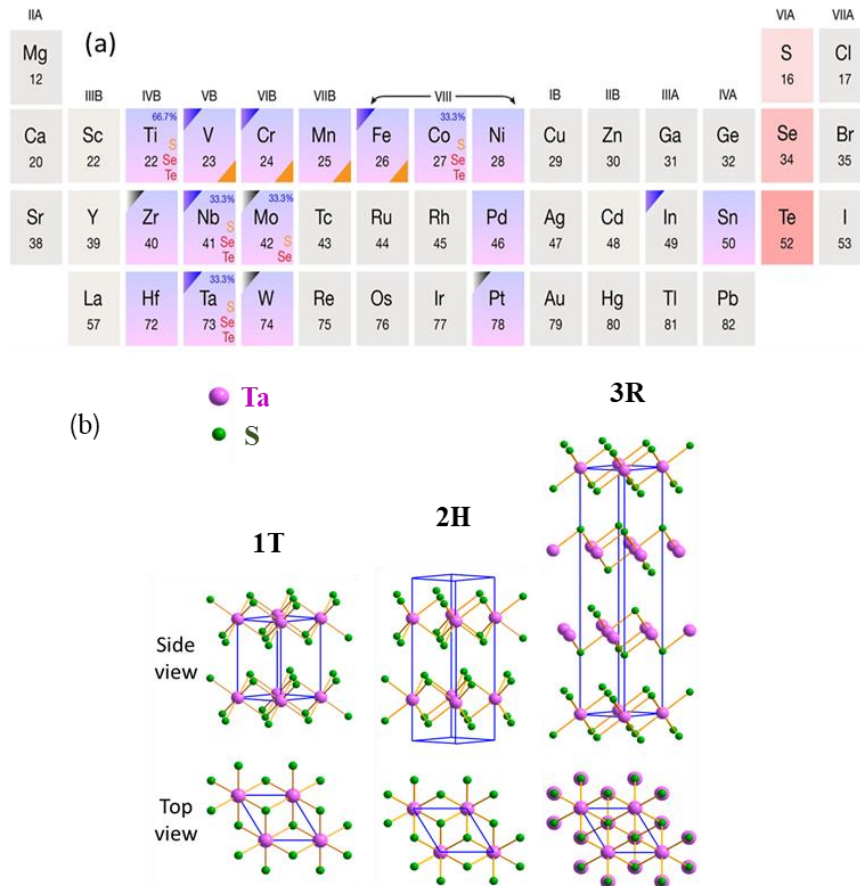


Fig. 1.10 (a) Periodic table showing metal (blue) and chalcogen (red) combinations that form two-dimensional TMDs[50]. (b) Schematics of structural polytypes: 1T (tetragonal symmetry), 2H (hexagonal symmetry) and 3R (rhombohedral symmetry)[53].

Table 1.1 The phases of  $\text{TaS}_2$  and corresponding physical properties, including CDW and superconductivity. The data are taken from Refs. [53], [55] and [56].

Phase	Physical properties	CDW transition temperature	Superconductivity
1T-TaS <sub>2</sub>	Semiconductor	350 K and 180 K	---
2H-TaS <sub>2</sub>	Metal	75 K	0.7 K
4H <sub>b</sub> -TaS <sub>2</sub>	Metal	315 K and 22 K	2.7 K
6R-TaS <sub>2</sub>	Metal	320 K and 305 K	2.6 K

Table 1.2 Crystal data and structure refinement of  $2H$ -TaS<sub>2</sub>. The data are taken from Ref. [59].

Chemical formula	$2H$ -TaS <sub>2</sub>
$M_r$	245.07 (g mol <sup>-1</sup> )
Crystal system	Hexagonal, $P6_3/mmc$
$a, c, V, Z$	3.314(1) Å, 12.097(1) Å, 115.06(5) Å <sup>3</sup> , 2
Radiation type	$\lambda(\text{Mo } K\alpha) = 0.71073$ Å
Density $\rho$	7.073 (g cm <sup>-3</sup> )
$\mu$	485.3 cm <sup>-1</sup>
Crystal size	0.08×0.06×0.0015 mm
Diffractometer	Enraf-Nonius CAD-4F
$T$	295 K
$(\sin \theta)_{\text{max}}/\lambda$	9.949 nm <sup>-1</sup>
$R_F; wR; S; w$	0.032; 0.037; 1.868; 1

### 1.3.2 Interplay between CDW and superconductivity in the $2H$ -TaS<sub>2</sub> system

In bulk  $2H$ -TaS<sub>2</sub>, there is a coexistence of CDW and superconductivity below 0.7 K, estimated from the electrical transport data in Fig. 1.11a. The measured superconducting tunneling conductance of  $2H$ -TaS<sub>2</sub> at 100 mK is shown in Fig. 1.10b[60], indicating that the band is fully gapped with a superconducting gap  $\Delta = 0.28$  meV (Fig. 1.11c). The temperature dependence of  $\Delta$  is also close to the value expected from BCS theory,  $\Delta = 1.76 k_B T_c = 0.265$  meV. The scanning tunnelling microscopy (STM) topography at constant current of  $2H$ -TaS<sub>2</sub> is shown in Fig. 1.11e. The hexagonal atomic S lattice is well observed, together with a remarkable triangular  $3 \times 3$  charge modulation of wavelength 3 times the lattice constant. The Fourier transform of the whole image shows that the CDW modulation is located at one-third of the in-plane reciprocal lattice wavevectors (Fig. 1.11f). The CDW modulation results in hexagons spanned by three vectors parallel to the three symmetry axes of the hexagonal atomic lattice, which are repeated in the topography.

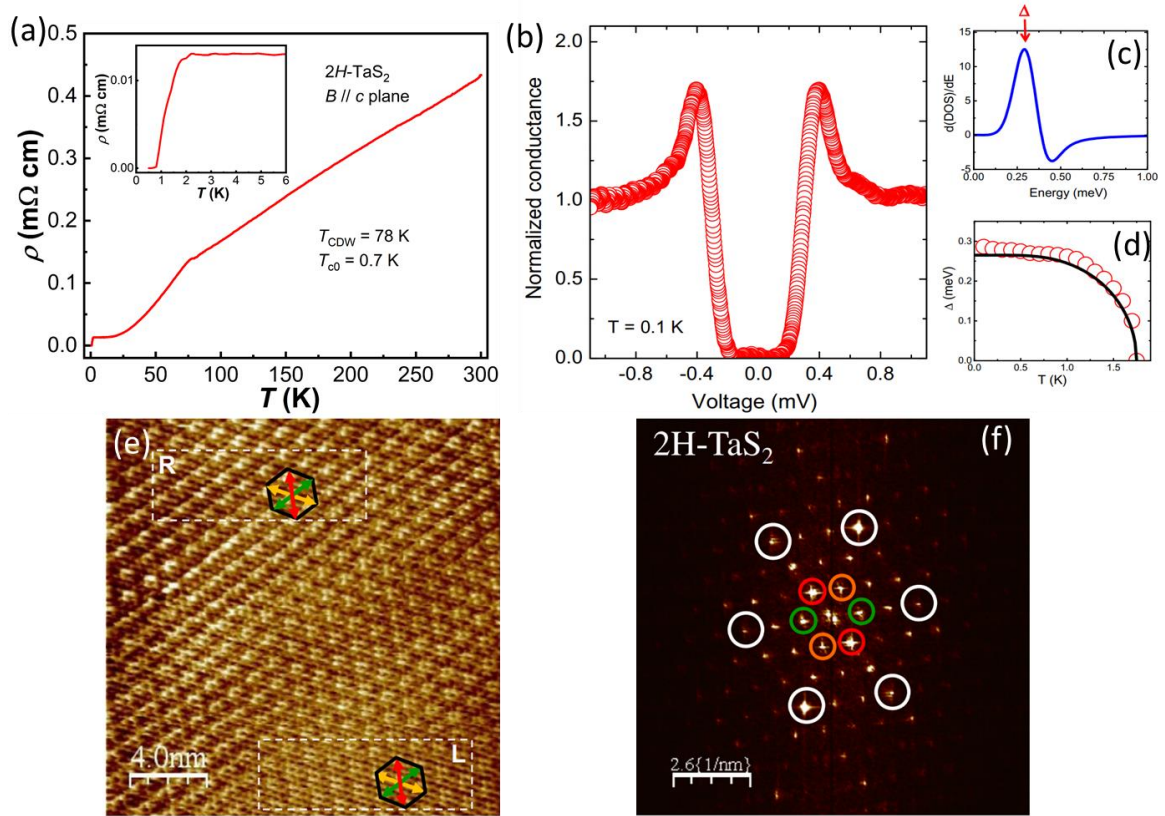


Fig. 1.11 (a) The temperature dependence of the resistivity of  $2H\text{-TaS}_2$  with the superconducting transition magnified in the inset. (b) The normalized tunneling conductance obtained in  $2H\text{-TaS}_2$  at 100 mK. (c) The derivative of the associated local DOS with a peak at  $\Delta = 0.28$  meV, obtained by deconvoluting the temperature from the tunneling conductance. (d) The temperature dependence of  $\Delta$  (red circles) and the expectation from the BCS theory (black line) with  $T_c = 1.75$  K. (e) The STM topography of  $2H\text{-TaS}_2$  measured at 5 mV and 100 mK, and (f) its corresponding Fourier transform. The data are taken from Ref. [60].

In the  $2H\text{-TaS}_2$  system, superconductivity and CDW order are two different electronic states, both arising from electron-phonon coupling and Fermi surface instability [61]. The existence of the CDW phase transition has an influence on the Hall effect, which is confirmed by the Hall coefficient  $R_H$  in thinned layered  $2H\text{-TaS}_2$  [62]. When the thickness exceeds two layers, a broad transition of  $R_H$  is observed from 20 to 70 K with a change of sign at  $\sim 56$  K, which can be explained by a two-carrier model with light holes and heavy electrons (Fig. 1.12a) [63]. This is accompanied by an increase in carrier density with suppression of the CDW state with increasing thickness (inset of Fig. 1.12b). When the thickness is reduced to two layers, the CDW is completely suppressed and both the temperature dependence of  $R_H$  and the change in sign are absent. This behaviour suggests that the suppression of the CDW state may be related to the interlayer coupling [64].

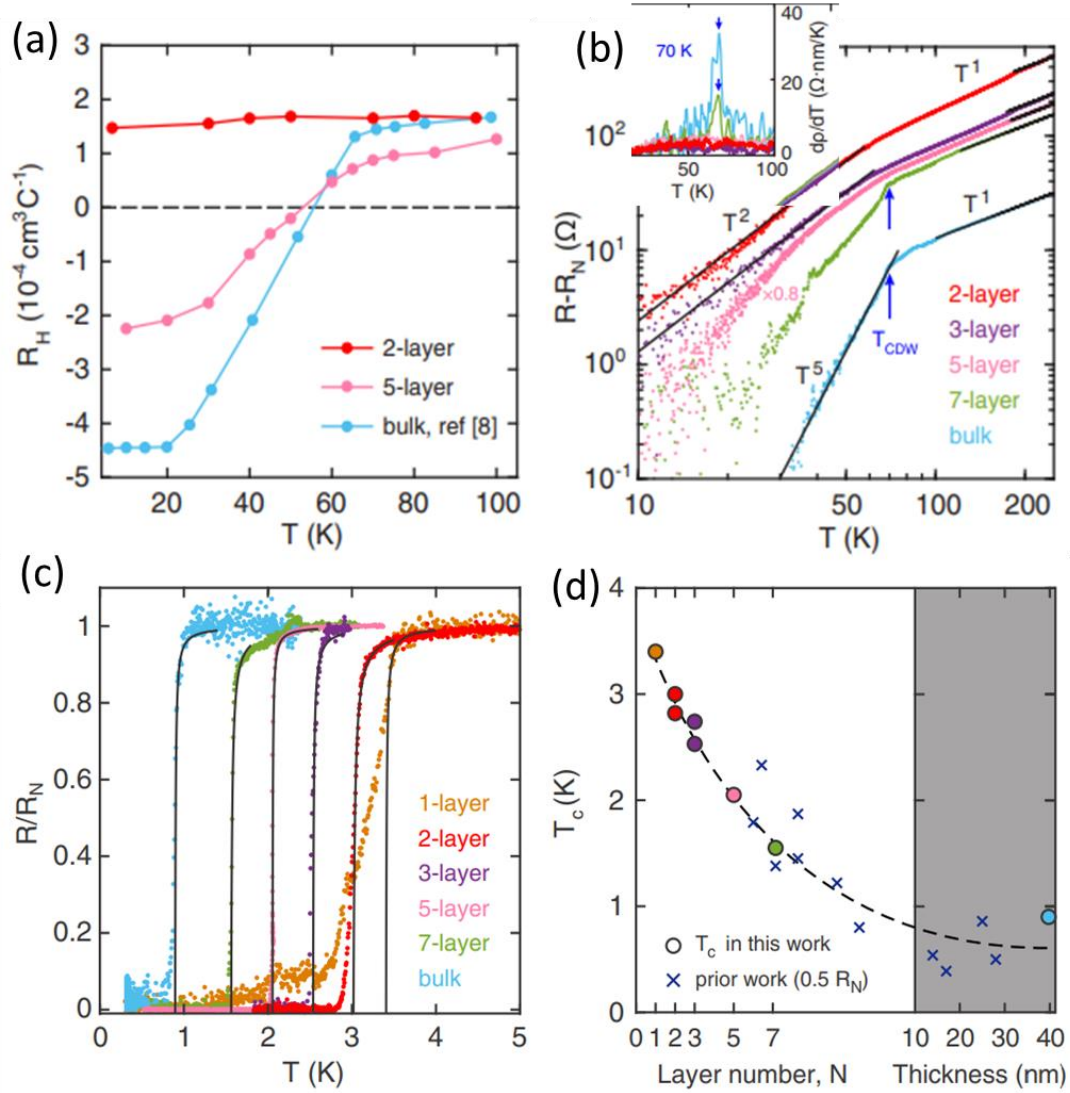


Fig. 1.12 (a) The temperature dependence of the Hall coefficient for different thicknesses of 2H-TaS<sub>2</sub>. (b) Resistance  $R - R_N$  as a function of temperature plotted on a log-log scale, where  $R_N$  is the residual resistance just above the onset temperature of superconductivity. For clarity, the data for five layers are scaled by a factor of 0.8. (c) Normalized Resistance ( $R/R_N$ ) as a function of temperature to show the superconducting transition for different thicknesses. (d)  $T_c$  as a function of thickness. The dashed line guides the eye to the general trend. The data are taken from Ref. [62].

The variation of the CDW can also be identified from the signatures of the electrical transport. As the thickness decreases into the two-dimensional region, the temperature-dependent resistivity changes from  $R \sim T^5$  to  $R \sim T^2$  after the CDW phase transition (Fig. 1.12b). Meanwhile,  $T_c$  strongly increases from 0.8 K for bulk to 3.4 K for monolayer TaS<sub>2</sub> (Figs. 1.12c-d). The variation of  $T_c$  shows a similar trend to that of the CDW order, indicating a close relationship between superconductivity and the CDW state. To further illustrate the interplay between them, the calculated band structures of the normal and CDW phases are plotted in Fig. 1.13a with red (normal phase) and grey (CDW phase) curves, respectively. The CDW



distortions induce a gap opening on the inner pocket around K along  $\Gamma$ -K and K-M due to the reconstruction of electronic structures in the Fermi energy. In Fig. 1.13b, the  $\text{DOS}(E_F)$  clearly increases with decreasing thickness due to the suppression of the CDW order, in agreement with the Hall measurements. Based on McMillan's theory,  $T_c$  can be evaluated using the electronic and phononic structure calculations. The evaluated  $T_c$  as a function of CDW amplitude is plotted in Fig. 1.13c with a maximum  $T_c$  of 3.75 K, which is similar to the experimental results. The increase in  $T_c$  is attributed to the suppression of CDW order, which indirectly leads to an increase in  $\text{DOS}(E_F)$ , indicating the competition between superconductivity and the CDW state.

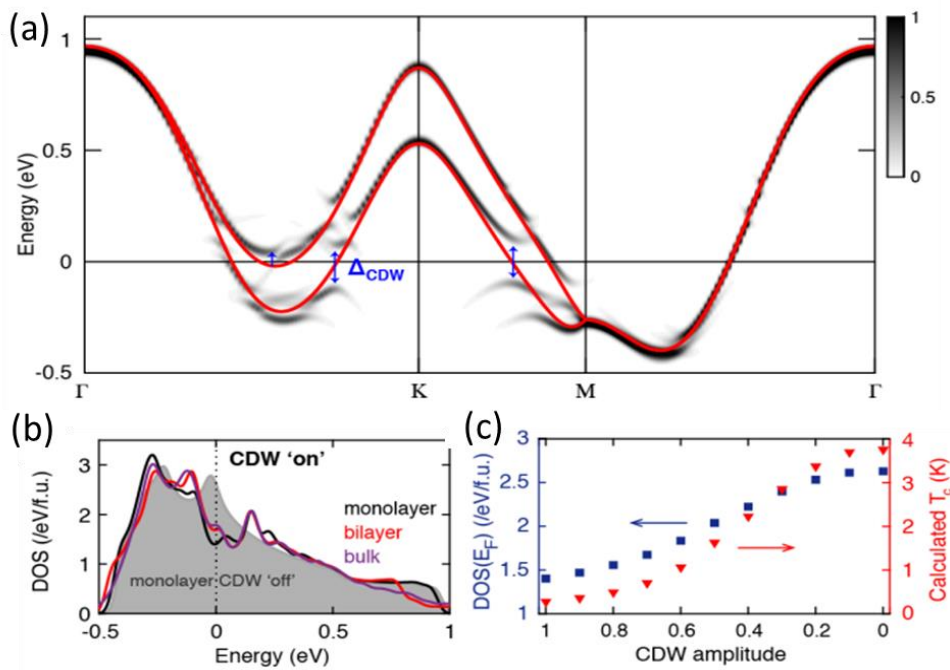


Fig. 1.13 (a) Band structure for monolayer  $2H$ -TaS<sub>2</sub>. (b) Density of states for monolayer/bilayer/bulk in the CDW phase. The monolayer in the normal phase is shown in grey for reference. (c)  $\text{DOS}(E_F)$  as a function of CDW amplitude for the monolayer, and  $T_c$  from McMillan's formalism using the calculated  $\text{DOS}(E_F)$ . The data are taken from Ref. [62].

The enhancement of superconductivity is also observed in the copper (Cu)-intercalated  $2H$ -TaS<sub>2</sub> (Fig. 1.14a). All  $2H$ -Cu<sub>*x*</sub>TaS<sub>2</sub> exhibit normal metallic characteristics in the high-temperatures range. At low temperature the  $T_c$  first increases and then decreases with Cu intercalation. Figure 1.14b shows the subtle changes observed at the CDW transition, where the CDW is completely suppressed for  $x = 0.06$ . All results are summarized in the phase diagram in Fig. 1.14c, where  $T_c$  presents a dome-shape accompanied by the suppression of the CDW with a maximum of  $\sim 4.7$  K close to the endpoint of the CDW. The suppression of the CDW is due to the disorder-induced dramatic decrease in CDW coherence with increasing Cu

intercalation, and the increase in  $T_c$  could be due to the electron doping in  $2H\text{-Cu}_x\text{TaS}_2$ . The exact details of the correlation between the CDW state and superconductivity at the microscopic level have not been experimentally observed, but the competition between superconductivity and the CDW order upon Cu intercalation is unquestionable, which is also similar to that of  $\text{Na}_x\text{TaS}_2$ [65]. Furthermore, a similar behaviour is also found in the isoelectronic substitution in  $2H\text{-TaSe}_{2-x}\text{S}_x$ , accompanied by the suppression of  $T_{\text{CDW}}$  by doping[66].

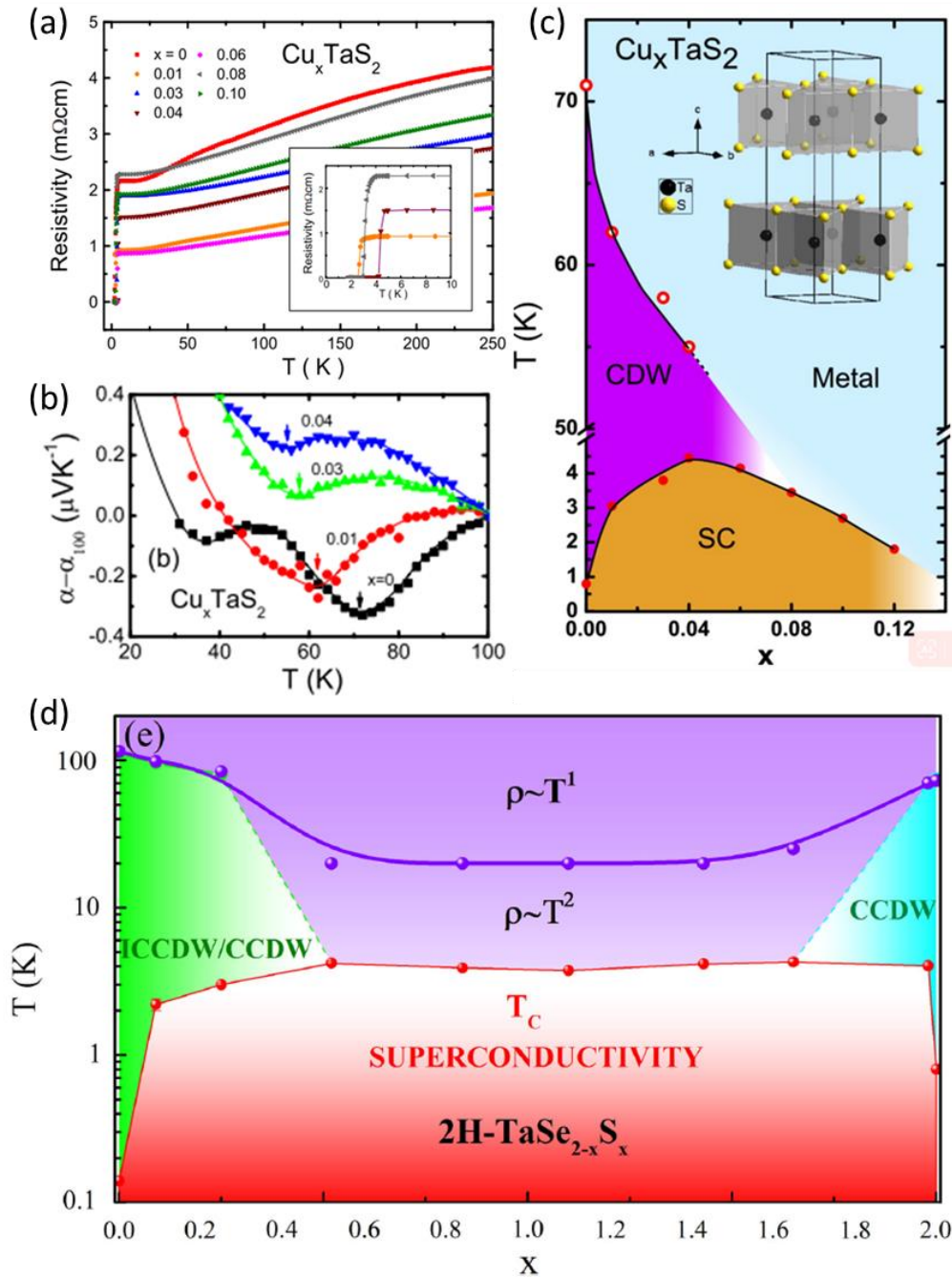


Fig.1.14 (a) Temperature dependent resistivity of polycrystalline  $\text{Cu}_x\text{TaS}_2$ . Inset: detail of superconducting transitions in  $\text{Cu}_x\text{TaS}_2$ . (b) Detail of the behaviour for  $\text{Cu}_x\text{TaS}_2$  in the vicinity of the CDW transition. (c) Electronic phase diagrams for  $\text{Cu}_x\text{TaS}_2$  and (d)  $2H\text{-TaSe}_{2-x}\text{S}_x$ . The data are taken from Refs. [66] and [67].

In Fig. 1.14d, the electronic phase diagram indicates a weak double superconducting dome, reflecting the interplay between CDW and superconductivity, where the  $T_c$  is enhanced up to  $\sim 4.28$  K near the  $2H$ -TaS<sub>2</sub> side. In the intercalated isoelectronic substitution series in  $2H$ -TaSe<sub>2-x</sub>S<sub>x</sub> single crystal alloys, a clear separation of disorder from doping-induced changes is possible. The sulfur substitution could introduce different Ta-S and Ta-Se bond lengths, disorder and wrinkling of the metal plane which could suppress the CDW order and increase the DOS( $E_F$ ), electron-phonon coupling and  $T_c$ [67]. The variation of  $T_c$  is directly correlated with crystallographic disorder and disorder-induced scattering of local CDW fluctuations. The doping-induced disorder tilts the balance of competition between superconductivity and CDW, resulting in an enhancement of superconductivity by a suppression of the CDW order.

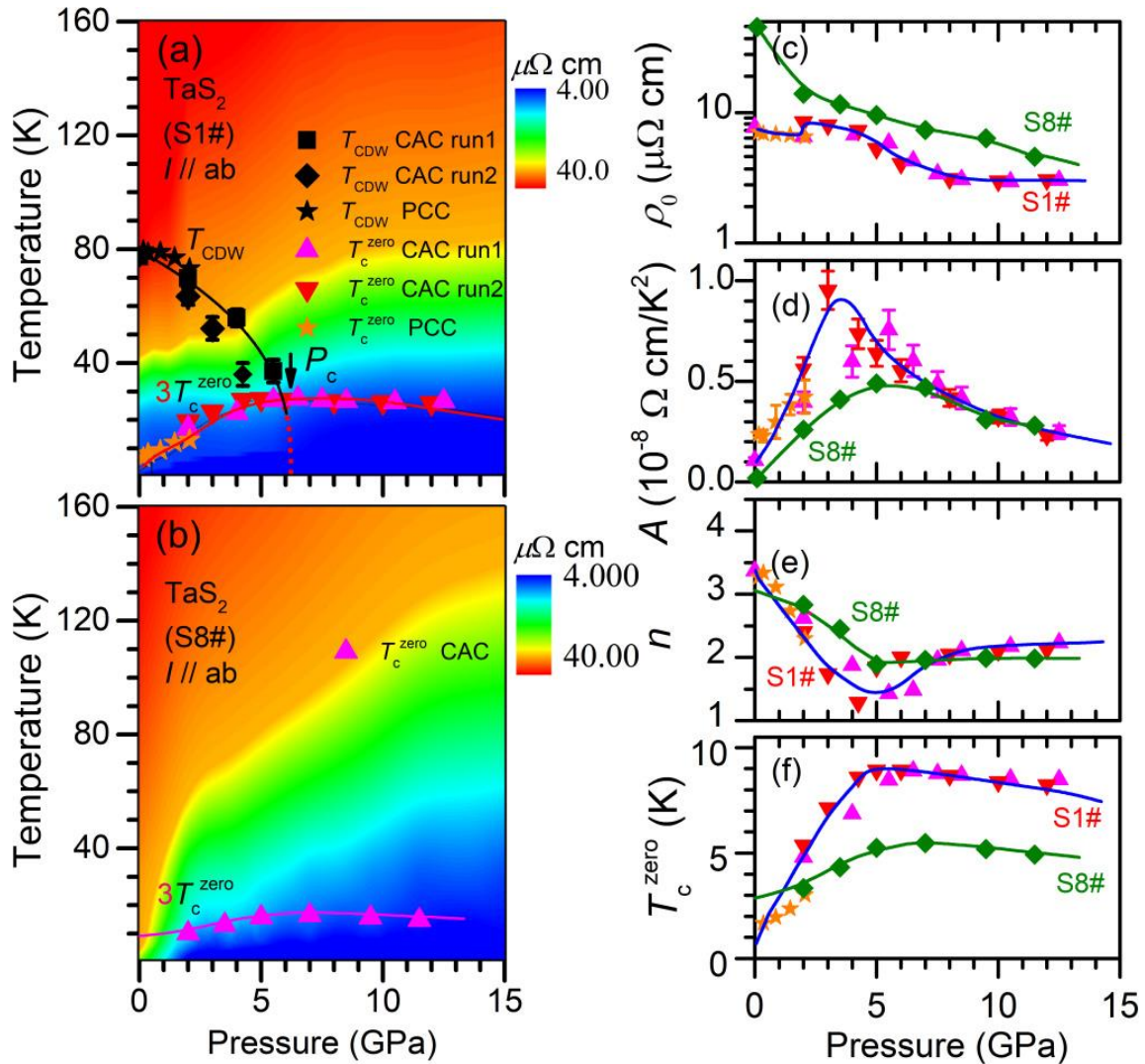


Fig. 1.15 Temperature-pressure phase diagram for (a)  $2H$ -TaS<sub>2</sub>, No. S1 (clean limit) and (b)  $2H$ -TaS<sub>2</sub>, No. S8 (dirty limit). The changing colours describe the tendency of the resistivity. Pressure dependence of parameters in the same scales for Nos. S1 and S8: (c)  $\rho_0$ , (d)  $A$ , (e)  $n$  and (f)  $T_c$ . The lines across the data show the changing trends. The data are taken from Ref. [68].

As mentioned above, doping or intercalation always inevitably introduces disorder into  $2H$ -TaS<sub>2</sub>, which can affect the CDW state, and even the superconductivity, although on very general grounds (Anderson's theorem) s-wave superconductivity is immune to weak disorder[69]. Applying pressure is a cleaner strategy to study the interplay between superconductivity and CDW in bulk  $2H$ -TaS<sub>2</sub>. For the single crystal  $2H$ -TaS<sub>2</sub> marked with S1 in Fig. 1.15a,  $T_c$  is strongly enhanced from 0.8 K to 9.15 K, accompanied by the suppression of  $T_{CDW}$ , and then decreases due to impurity scattering with increasing physical pressure (Fig. 1.15f). In addition, the  $A$  values, estimated from the quantitative analysis by an empirical formula  $\rho = \rho_0 + AT^n$  at low-temperature, show a similar trend to that of  $T_c$  with one order of magnitude increase at the critical pressure in Fig. 1.15d. Accompanying this, the pressure dependence of the thermal exponent  $n$  decreases rapidly from  $\sim 3.36$  to  $\sim 1.29$  at the critical pressure and back to  $\sim 2.10$  with further increase in pressure, suggesting the formation of non-Fermi-liquid behaviour with a pressure-induced collapse of the CDW at the critical pressure and the recovery to Fermi-liquid behaviour (Fig. 1.15e). Both features strongly manifest that the enhanced critical CDW fluctuations at the critical pressure may be an important ingredient for the superconducting pairing. For  $2H$ -TaS<sub>2</sub> in the dirty limit marked with S8 in Fig. 1.15b, the CDW phase transition is absent and  $T_c$  is  $\sim 3.2$  K by electrical transport measurement. Upon physical pressure,  $T_c$  shows a similar dome to S1 with a maximum of 6.43 K near the critical pressure. The pressure dependences of  $T_c$  and  $n$  broaden and become less pronounced as compared to the clean crystals. These features suggest that disorder and the variation of CDW are two independent factors affecting superconductivity. The enhancement of  $T_c$  is associated with the suppression of CDW by pressure and the increase of the DOS( $E_F$ ). Furthermore, the CDW critical fluctuations could be related to the non-Fermi-liquid behavior with strong competitions between the CDW state and superconductivity at critical pressure.

Based on the above discussion,  $T_c$  exhibits a similar dome-shaped dependence of disorder, intercalation and physical pressure, although the lattice parameters and electronic properties are altered differently. The disorder destroys the long-range CDW order, resulting in lattice distortions and a broadening of electronic bands which could partially fill the CDW energy gap. By increasing the interlayer spacing, such as upon Cu or Na intercalation[67, 70], the interlayer van der Waals interaction is weakened, which could increase the charge carrier concentration and enhance the electron-phonon coupling strength. After the collapse of the long-range CDW, strong impurity scattering leads to a decrease of  $T_c$ . Upon applying physical pressure on the other hand, the critical pressure shows a wide range from 7.3 to 17 Gpa, which could be related to the crystal quality and different ways of the pressure measurements[68, 71-73]. In addition,

the maximum of  $T_c$  also shows a large difference between studies on different crystal quality, which emphasizes the importance of the disorder level in the  $2H\text{-TaS}_2$  system.

## **1.4 Scope of the thesis**

The focus of this thesis is on the  $2H\text{-TaS}_2$  system, which exhibits superconductivity, CDW and an interplay with each other, as summarized in this introductory chapter. After an overview of the experimental concepts and methodology in Chapter 2, the investigations of this thesis are outlined. First, the relationship between superconductivity and CDW is presented for lithium-intercalated  $2H\text{-TaS}_2$  (Chapter 3). These results are extended by a detailed study of Li-H<sub>2</sub>O group-intercalated  $2H\text{-TaS}_2$  in Chapter 4. Finally, the effects of defect controlled disorder on superconductivity, the CDW state and quantum criticality in the  $2H\text{-TaS}_2$  system are investigated in Chapter 5.

## Chapter 2

### Experimental Methods

#### 2.1 Solid-state synthesis

Solid-state synthesis is a well-known route to obtain thermodynamically stable phases at high temperatures by solid-state diffusion[74], where the transport of atoms occurs without leaving the solid phase. The parameters involved in the thermodynamics, kinetics and diffusion, determine the outcome of a solid-state synthesis[75]. They can be finely tuned by careful control of experimental conditions such as reaction time, temperature and atmosphere.

To obtain clean and high-quality samples, the pre-treatment of the raw chemicals is key to solid-state synthesis. In our experiment, the appropriate precursors were weighed in the desired quantities and well mixed in a mortar to obtain a homogeneous mixture of reactants. The mixed precursors were then transferred to a suitable environment to anneal and grow crystals at high temperatures. In this thesis, for example, to obtain TaS<sub>2</sub>, a local stoichiometry of 1:2 of Ta to S powder is required. Mixing and grinding can ensure a homogeneous distribution and a high contact area in a glove box filled with argon. To avoid incomplete or side reactions, it is necessary to expose pre-mixed precursor powders to high temperatures for a long time in a sealed quartz tube under vacuum ( $<10^{-3}$  Torr). The final product often consists of a thermodynamically stable phase with micron-sized and dimensionally uniform crystallites in which the *2H* phase is formed at annealed temperature of 1073 K and the *1T* phase is formed at annealed temperature of 1273 K. The alkaline metal such as lithium is highly reactive and flammable in air and must be stored in an inert atmosphere or mineral oil[76]. For this reason, related chemicals such as Li<sub>x</sub>TaS<sub>2</sub> must be stored in a glove box filled with argon gas. The solid reagents Li<sub>2</sub>S, S and Ta powder were mixed, ground and pressed into a pellet which was sealed in a quartz tube under vacuum ( $<10^{-3}$  Torr). The main reaction took place at 1073 K to give the *2H* type Li<sub>x</sub>TaS<sub>2</sub>[77].

#### 2.2 Measurement techniques

##### 2.2.1 Powder X-ray Diffraction (PXRD)

X-ray diffraction is a technique where the atoms of a crystal, due to their uniform spacing, cause an interference pattern of the waves present in an incident X-ray beam. The interference caused

by the scattering of X-rays obeys Bragg's law, and is monitored with a suitably positioned detector (Fig.2.1). It can reflect sample information such as crystal structure, phase purity, cell parameters etc. Powder diffraction data were collected at room temperature using a Stoe STADIP diffractometer with Cu  $K_{\alpha}$  ( $\lambda \sim 1.5406 \text{ \AA}$ ). The Rietveld refinements and profile fits of the diffraction patterns were carried out using the package FullProf SUITE[78] and *autoFP*[79], which is a highly automated software toolkit and has been developed to improve the extent of automation of the widely used Rietveld refinement program FullProf to estimate the fine details of crystal structure and cell parameters.

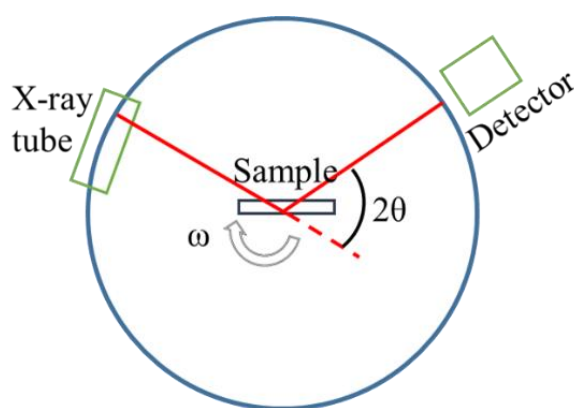


Fig. 2.1 Components of an X-ray diffractometer.

### 2.2.2 Thermogravimetric Analysis (TGA)

TGA is a thermal analysis method in which the weight variation of samples is recorded and studied over a wide range of temperatures. Typically, the temperature is varied at a fixed rate while the reaction atmosphere varies from vacuum, ambient air to inert gases such as nitrogen or argon. The results can indicate physical and chemical properties of the sample, including phase transitions, thermal decomposition, solid-gas reactions, etc. Based on the atmosphere used and for known reaction paths, TGA can also be used to determine the weight percentage of each component in composites. In this thesis, a TGA experiment was carried out on a thermogravimetric analyzer (Q500, TA Instruments) under argon flow to estimate the amount of interlayer water.

### 2.2.3 Scanning Electron Microscope (SEM) and Energy Dispersive X-ray Spectrometer (EDS)

SEM is a common electron microscope used to image the surface (and/or cross-sectional) morphology of samples. A high-energy beam of electrons is used to collect the signals resulting from the interactions between electrons and atoms on the sample surface. The detection of

secondary electrons emitted by atoms is the most commonly used mode to observe the surface topography while the generated X-rays can be recorded by EDS to analyze the elemental composition and distribution.

In this thesis, both the polycrystalline and single crystalline samples were conductive composites. They were fixed directly to an aluminum holder with conductive carbon tape for characterization using a Zeiss GeminiSEM 450 SEM. The SEM images were taken under 15 kV acceleration voltage and 20  $\mu$ A emission current. The EDS equipment is an Oxford X-ray detector (X-MAX80, AZTec Advanced) for elemental analysis of materials.

### 2.2.4 Transmission Electron Microscopy (TEM)

TEM is a type of electron microscopy that produces images by passing a beam of electrons through ultrathin specimens. When magnified and focused by an imaging equipment, TEM can produce extra high-resolution images for characterizing surface morphology and crystal structure. TEM can also be modified for EDS mapping using an EDS detector. In this thesis, samples were loaded on a copper grid with holey carbon films. The bright-field TEM images and elemental mapping were collected using a Thermo Fisher Scientific Talos F200X TEM operating at 200 kV with EDS.

### 2.2.5 Raman measurements

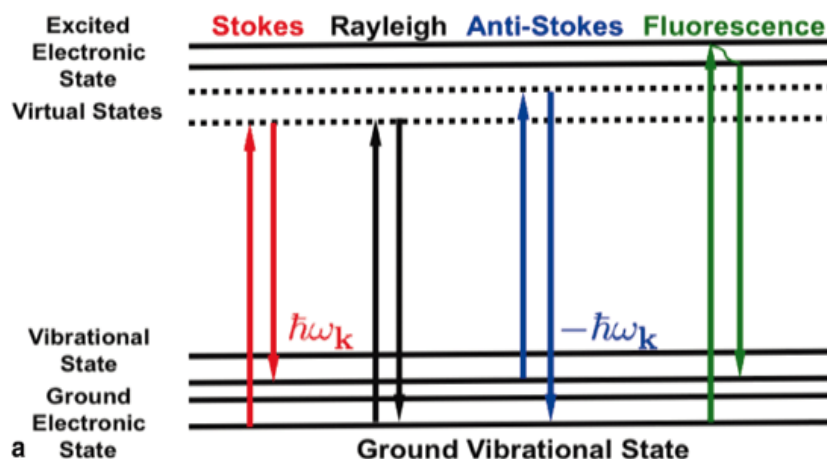


Fig. 2.2 Energy diagram of Raman (Stokes and Anti-Stokes), Rayleigh (elastic scattering) and fluorescence, and corresponding scattering processes. The data are taken from Ref.[80].

Raman spectroscopy, as a common spectroscopic technique, is mainly used to study the vibration of molecules, while rotational or some other low-frequency modes may be included. Raman scattering is an inelastic scattering of light which originates from the change in



electronic polarizability of the system due to the quasi-particle excitations. In Fig. 2.2, when the incident radiation (photons) interacts with the medium, it can be scattered either elastically or inelastically[80]. If the scattered photons have the same energy as that of incident one, it is called Rayleigh scattering; on the other hand, if the scattered photons have more/less energy than the incident one, it is called Anti-Stokes/Stokes Raman scattering. Based on the inelastic scattering of photons, laser photons can interact with molecular vibrations, phonons or other excitations. The resulting energy shifts are recorded to provide details about the vibrational modes in the system.

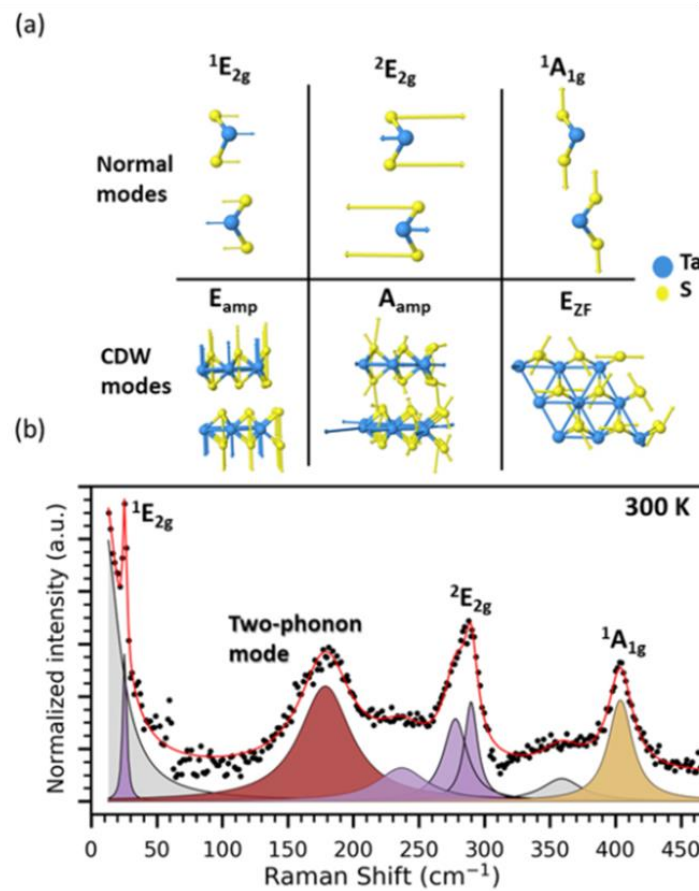


Fig. 2.3 (a) Mode displacement diagrams corresponding to modes in the normal and CDW phase. (b) Raman spectra of bulk  $2H-TaS_2$  with observed modes and their assignments at 300 K. The data are taken from Ref. [189].

Based on the crystal structure of the  $2H-TaS_2$  in Fig. 1.10b, there are nine vibrational modes at the center of the Brillouin zone ( $\Gamma$ -point), three of which are acoustic and six are optical modes, where these optical modes are given by  $\Gamma = A_{1g} + E_{1g} + 2E_{2g} + A_{2u} + E_{1u}$ . Here,  $A_{1g}$ ,  $E_{1g}$  and  $E_{2g}$  are Raman active while  $A_{2u}$ , and  $E_{1u}$  are infra-red active modes [188, 189]. The corresponding the CDW modes and their symmetries, along with their atomic displacements are shown in the top left corner (Fig. 2.3a). The Raman data for  $2H-TaS_2$  in the normal state (above  $T_{CDW}$ ) was

acquired with 532 nm excitation at 300 K (Fig. 2.3b). The data can be fit (red curve) using a combination of eight Voigt functions. Two-phonon mode is shaded brown. Purple and golden shades represent modes with E and A symmetry, respectively. Grey areas represent fits to the laser Rayleigh line and other features not predicted to be part of the material's Raman spectrum. In this thesis, Raman analyses were performed using an inVia™ Raman microscope and a Horiba Labram HR Evolution spectrometer equipped with an Olympus microscope and an ultra-narrow notch filter with laser excitation at 532 nm. The samples were mounted in a He flow cryoVac micro Konti cryostat to measure them at different temperatures.

### 2.2.6 Inductively Coupled Plasma Mass Spectrometry (ICP-MS)

ICP-MS is typically used to analyze samples that are liquids (such as water) or that can be dissolved or acid digested to form a liquid. The ICP-MS instrument uses a plasma to ionize the elements in a sample and then measures the ions using a mass spectrometer. In this thesis, the lithium content of the  $\text{Li}_x\text{TaS}_2$  sample was determined using ICP-MS. Figure 2.4 shows a simple diagram of the instrument. First, a typical calibration was performed using standards prepared at concentrations between 0.1 and 100ng/L for the lithium. The  $\text{Li}_x\text{TaS}_2$  sample was dissolved in nitrohydrochloric acid and diluted for measurement. Liquid samples are nebulised in the sample introduction system to produce a fine aerosol, which is then transferred to the argon plasma. The high-temperature plasma atomises and ionises the sample, generating ions which are then extracted through the interface region and into a set of electrostatic lenses called the ion optics. The ion optics focus and direct the ion beam into the quadrupole mass analyzer. The mass analyzer separates ions according to their mass-to-charge ratio, and these ions are measured on the detector. The interlayer lithium concentration was derived by comparing the measured counts in the sample with the calibration counts[81].

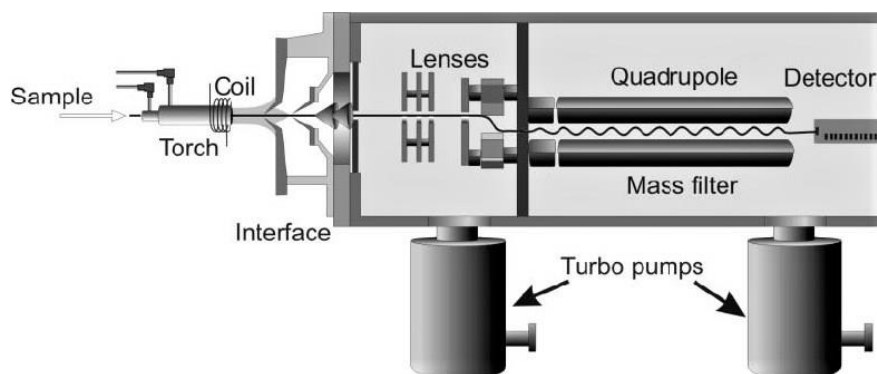


Fig. 2.4 Schematic cross section schematic of an ICP-MS[81].

## 2.3 Physical Property Measurement System (PPMS)

PPMS is an open architecture, variable temperature-field system designed to perform a variety of automated measurements including resistivity, heat capacity, etc. with specially designed measurement options. Sample environment controls include magnetic fields up to  $\pm 9.0$  Tesla and a temperature range of 1.8 - 400 K and even down to 0.4 K with a  $^3\text{He}$  option.

### 2.3.1 Electrical transport

Resistivity measurements were carried out using a standard four-probe technique with gold or silver wires of 25 or 50  $\mu\text{m}$  diameter, in which the two outer probes are used to apply current and the two inner probes are used to measure the resulting voltage drop across the surface of the sample. The wires were attached to the sample using Dupont silver conductive paste. The use of four probes eliminates measurement errors due to the probe resistance, the spreading resistance under each probe and the contact resistance between each metal probe and the sample being measured. The PPMS standard resistivity sample pucks have four contacts: one positive and one negative contact for current and voltage, for each user bridge board channel to which a sample can be wired. Up to three samples can be mounted on a resistivity puck, so the resistivity option can measure up to three samples simultaneously. In this thesis, the typical resistance is in the order of 1 Ohm when measured with a multimeter for any two channels, indicating good contacts to the samples.

Ohm's law gives the relationship between electrical current  $I$  and voltage  $V$

$$R = V/I, \quad (2-1)$$

where  $R$  is the resistance. The resistivity  $\rho$ , which is independent of the sample geometry, is evaluated from

$$\rho = (R \times w \times d)/l, \quad (2-2)$$

where  $w$ ,  $l$  and  $d$  are the width, length and thickness of the sample being measured, respectively (Fig. 2.5).

The Hall effect was first discovered in 1879 by Edwin Herbert Hall, who found that a transverse voltage developed when an electric current passed through a gold film under a magnetic field. It states that when a magnetic field is applied in the direction perpendicular to the current flow,

the Lorentz force causes deflection of the current according to the Lorentz force acting on the charges  $q$  given by

$$\mathbf{F} = q\mathbf{v} \times \mathbf{B}. \quad (2-3)$$

As a result, a negative charge accumulates on one side of the sample and a positive charge accumulates on the other side, creating a potential difference and an electric field across the sample. When the magnetic force  $F_m$  is equal to the electric force  $F_e$  generated by the Hall electric field, a state of equilibrium is achieved (Fig. 2.5)[82], with

$$|\mathbf{F}| = |q\mathbf{v} \times \mathbf{B}| = q V_H/w. \quad (2-4)$$

Combined with  $I = nqvwd$  with the charge carrier density  $n$ , the Hall voltage is given by

$$V_H = \frac{IB}{nqd}. \quad (2-5)$$

The Hall coefficient  $R_H$  is defined as

$$R_H = \frac{V_H d}{IB} = \frac{\rho_{xy}}{B} = \pm \frac{1}{nq}. \quad (2-6)$$

The sign of  $R_H$  reflects the nature of the charge carriers, holes (positive) or electrons (negative).

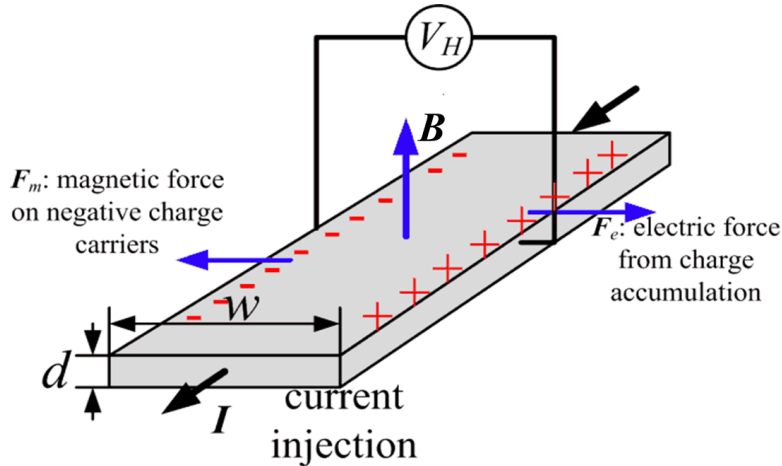


Fig. 2.5 Schematic view of a (n-type) Hall device. A constant current  $I$  and a constant magnetic field  $B$ , perpendicular to the surface are applied. This causes an accumulation of charge carriers transverse to the current direction and a Hall voltage,  $V_H$ .  $F_m$  and  $F_e$  indicate the magnetic and electric forces, respectively. Note that the direction of the current  $I$  in the diagram is that of the conventional current, so the motion of electrons is in the opposite direction[82].

### 2.3.2 Heat capacity

Heat capacity measurements can provide valuable information about the lattice and electronic system of materials. Heat capacity measurements, especially when taken at temperatures well below the Debye temperature, almost directly probe the electronic energy levels of a material and thus allow the density of states or energy levels to be estimated. For the standard heat capacity puck of the PPMS, a platform heater and a platform thermometer are attached to the bottom side of the sample platform. Thin wires provide the electrical connection to the platform heater and platform thermometer and also provide the thermal connection and structural support. The samples were mounted to the platform using a thin layer of N-grease, which provided the necessary thermal contact. The samples were measured under high-vacuum conditions to reduce the amount of gas in the sample chamber to minimize unwanted heat transfer.

### 2.3.3 Magnetic properties

Magnetometry is the measurement of magnetism and its effects. The quantity usually measured is the magnetic moment  $\mathbf{m}$  of a sample. The results presented in this thesis have been measured using a Superconducting Quantum Interference Device (SQUID) magnetometer. SQUID magnetometers can measure the magnetization of a sample as a function of magnetic field and/or temperature. Here, we used a commercial Quantum Design SQUID magnetometer (MPMS3). The MPMS3 utilizes a superconducting magnet (a solenoid made of superconducting wire) to expose samples to magnetic fields of up to  $\pm 7$  Tesla, and allows for sample temperature control from 400 K down to 1.8 K, achieved using liquid helium and liquid nitrogen.

In the work presented in this thesis, samples are mounted on quartz, brass or clear drinking straw sample holders using GE vanish paste. For accurate magnetic moment measurements, the magnetic signature of the sample holder is measured prior to mounting the sample. Once the sample moment is measured, the background signal from the sample holder is subtracted from the measurement. The MPMS3 typically detects the change in magnetic flux created by mechanically moving the sample through a superconducting pick-up coil, which is converted to a voltage.

The sample is centered in the detector coils before a measurement begins. Two types of measurements have been made using the MPMS3 to measure magnetic properties. Magnetic field-dependent magnetization  $M(B)$  at constant temperature, and temperature-dependent magnetization  $M(T)$  at constant magnetic field. The  $M(T)$  measurements can be performed using

zero-field-cooled (ZFC) or field-cooled (FC) protocols. In the ZFC process, a magnetic field is applied before a cold sample is warmed up. In the FC process, a sample is cooled in the presence of an applied magnetic field. Such measurements are particularly useful for studying the Meissner effect and estimating the superconducting volume fraction.

## Chapter 3

### The superconductivity and charge-density wave formation in lithium-intercalated 2H-TaS<sub>2</sub>

The interplay between superconductivity and CDW has been studied for decades, but there is still no consensus including cuprates and TMDs superconductors[83-88]. Since they both originate from electron-phonon coupling and Fermi surface instabilities[89-93], studying their relationship is crucial to understanding superconductivity. Artificially introduced heterogeneous atoms can tip the potential balance between two cooperative electronic states, and reveal the underlying interactions that give rise to them. Here, a series of lithium-intercalated 2H-TaS<sub>2</sub> has been prepared to investigate the variations of superconductivity and CDW with intercalated lithium. A comprehensive measurement has been performed, including bulk resistivity, Hall resistivity, magnetic properties and heat capacity, indicating that superconductivity and CDW coexist and compete with each other. The CDW weakens with increasing intercalated lithium, which indirectly increases the charge carrier density and enhances superconductivity.

#### 3.1 Introduction

The 2H-TaS<sub>2</sub> (pyridine)<sub>1/2</sub>, as the first organic intercalation compound, shows an enhanced  $T_c$  up to 3.5 K, opening the door to study intercalated 2H-TaS<sub>2</sub> in general[94, 95]. To explore the relationship between CDW and superconductivity, various alkali-metal or transition-metal atoms have been introduced into the structure to modify the electronic states of 2H-TaS<sub>2</sub>[42, 67, 70, 96-100]. The  $T_c$  of 2H-Cu<sub>x</sub>TaS<sub>2</sub>, for example, shows an intercalated-Cu dependent dome, in which the CDW is gradually weakened until it disappears at the maximum  $T_c$  on the left side of the dome[67]. This is a common feature of many intercalated 2H-TaS<sub>2</sub> or other two-dimensional materials[43, 67, 87]. The interplay between superconductivity and CDW has been interpreted as a suppression of CDW order being accompanied by an enhancement of superconductivity, suggesting a competitive relationship. However, more detailed explanations for the enhancement of superconductivity have been debated, including enhanced interlayered electron-phonon coupling[101, 102], a variation of the DOS( $E_F$ )[62] and electron doping[67, 103, 104]. Therefore, the details of the effect of intercalation on superconductivity and CDW in 2H-TaS<sub>2</sub> are not yet fully understood.

## 3.2 Experiments

Polycrystalline 2H-Li<sub>x</sub>TaS<sub>2</sub> samples were synthesized by solid-state reaction methods. Stoichiometric amounts of raw materials (99.9% Li<sub>2</sub>S, 99.99% Ta, and 99.9% S powders) were mixed, ground, pressed into tablets, and sealed in evacuated silica tubes. The tubes were then loaded into a muffle furnace and annealed at 800 °C for 12 hours. Finally, they were cooled down to room temperature along with the cooling of the furnace. Single crystals for  $x = 0$  and  $x = 0.007$  were obtained by extending the annealing time. The tubes were heated slowly up to 800 °C, sintered for 72 h, and then slowly cooled down to 600 °C with a cooling rate of 2 °C/h. Finally, the tubes were cooled down in the furnace by auto-switching off the power.

The crystal structure and phase purity were characterized by PXRD measurements, collected on all the as-prepared samples using a Stoe STADIP diffractometer at room temperature with Cu K<sub>α1</sub> radiation. The PXRD patterns were collected in the 2θ range of 5-95°. The Rietveld refinements and fits were performed using the package FullProf SUITE[78]. The cell parameters were estimated using the *autoFP* software[79], which was also validated by the results of that FullProf SUITE software.

The electrical transport was measured using a PPMS equipped with a <sup>3</sup>He insert and a standard four probe. The samples were cut into rectangular shapes and four electrical contacts were applied to each sample with 25-μm-diameter Au wires attached to the samples using Dupont 4929 silver paint. Hall resistivity measurements were performed on one sample mounted in a four-probe configuration using the same contacting technique as for the resistivity measurements. Measurements were taken in a PPMS with scanning magnetic fields from +9.0 T to −9.0 T. The specific heat was measured using the heat-capacity option of the PPMS equipped with a <sup>3</sup>He insert at a zero-magnetic field. Magnetization measurements were performed using a MPMS3 equipped with a 7.0 T superconducting magnet. Magnetic properties were measured in two types of modes: by temperature scanning with a magnetic field of 2.0 mT, both zero-field-cooled (ZFC) and field-cooled (FC) between 1.8 and 5 K, or by magnetic-field scanning from 0 to 10 mT with set temperatures from 1.8 K to 3.6 K and 0.2 K per step.

## 3.3 Results and discussion

### 3.3.1 Characterization of structure

The influence of lithium intercalation on the structure of 2H-TaS<sub>2</sub> is shown in Fig. 3.1. The identity and phase purity of the samples were determined by PXRD. The diffraction patterns of



all lithium-intercalated 2H-TaS<sub>2</sub> samples are shown in Fig. 3.1a, which can be well-fitted to the 2H-type structures ( $P6_3/mmc$ ) for lithium contents below  $x = 0.096$ [59]. The Rietveld refinement for 2H-Li<sub>0.064</sub>TaS<sub>2</sub> is shown in Fig. 3.1b, demonstrating high phase purity. The lithium contents of these polycrystalline 2H-Li<sub>x</sub>TaS<sub>2</sub> samples have been determined by ICP-MS measurements. The slight systematic variation of the (110) peaks with increasing lithium content  $x$  is shown in Fig. 3.1c. For  $x \leq 0.096$ , the cell parameters of  $a$  and  $c$  show only small but systematic changes (Fig. 3.1d), resulting in a shrinking of the unit cell volume. The  $c$  axis shows a regular decrease, which is similar to the trend observed in sodium intercalated NbS<sub>2</sub> and 2H-TaS<sub>2</sub>[70, 98, 106]. This can be taken as an evidence that the lithium atoms are not substituting Ta atoms but are intercalated into the interlayer regions of 2H-TaS<sub>2</sub>. As the lithium content is increased further beyond 0.096, the crystal structure changes. The distance between the two adjacent layers can be determined to be  $\sim 4.4$  Å, which is much larger than for Li<sub>x</sub>TaS<sub>2</sub> with  $x < 0.096$  ( $\sim 3.4$  Å). It is therefore unreasonable to assume that at high lithium contents, only lithium ions exist between the layers. As the samples of Li<sub>x</sub>TaS<sub>2</sub> are air-sensitive, it has been speculated that trace amounts of moisture enter the interlayer regions of TaS<sub>2</sub> for chelation with lithium ions due to the unstable chemical nature of lithium, forming Li<sub>x</sub>(H<sub>2</sub>O)<sub>y</sub>TaS<sub>2</sub>[97, 98]. The study if this system will be the topic of chapter 4 of this thesis.

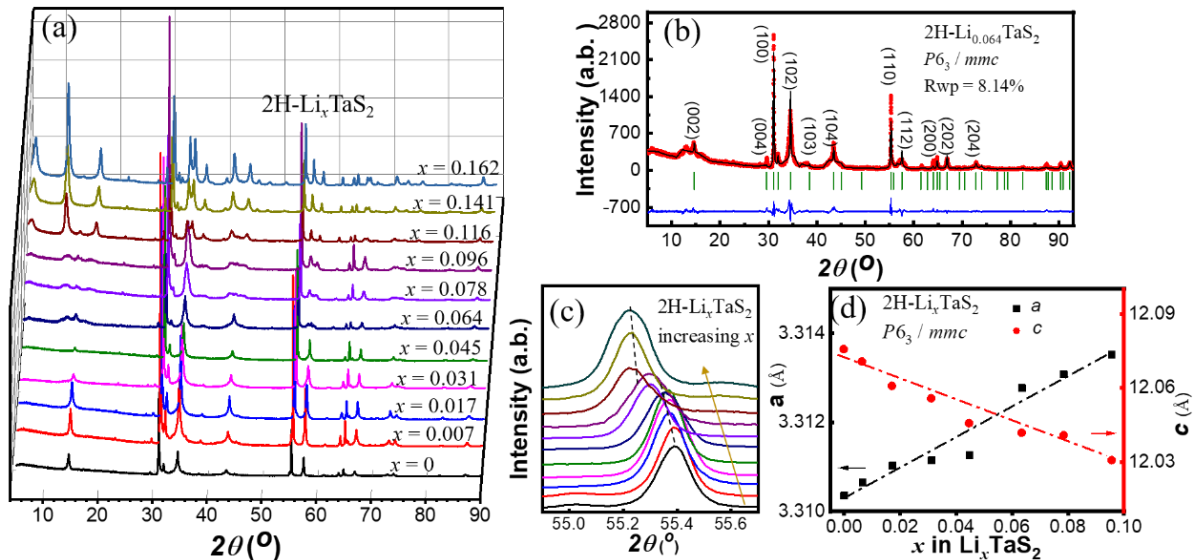


Fig. 3.1 (a) The PXRD pattern at ambient temperature for all samples of 2H-Li<sub>x</sub>TaS<sub>2</sub> ( $0 \leq x \leq 0.162$ ). (b) The PXRD pattern of 2H-Li<sub>0.064</sub>TaS<sub>2</sub>. The red dots are the observed data, while the black solid line represents the calculated intensities. The bottom blue solid line is the difference between the observed and calculated intensities. (c) The enlarged (110) reflections with increasing  $x$ , indicating the variation of cell parameters. (d) The change of the cell parameter for 2H-Li<sub>x</sub>TaS<sub>2</sub> samples ( $0 \leq x \leq 0.096$ ).

### 3.3.2 Electrical transport

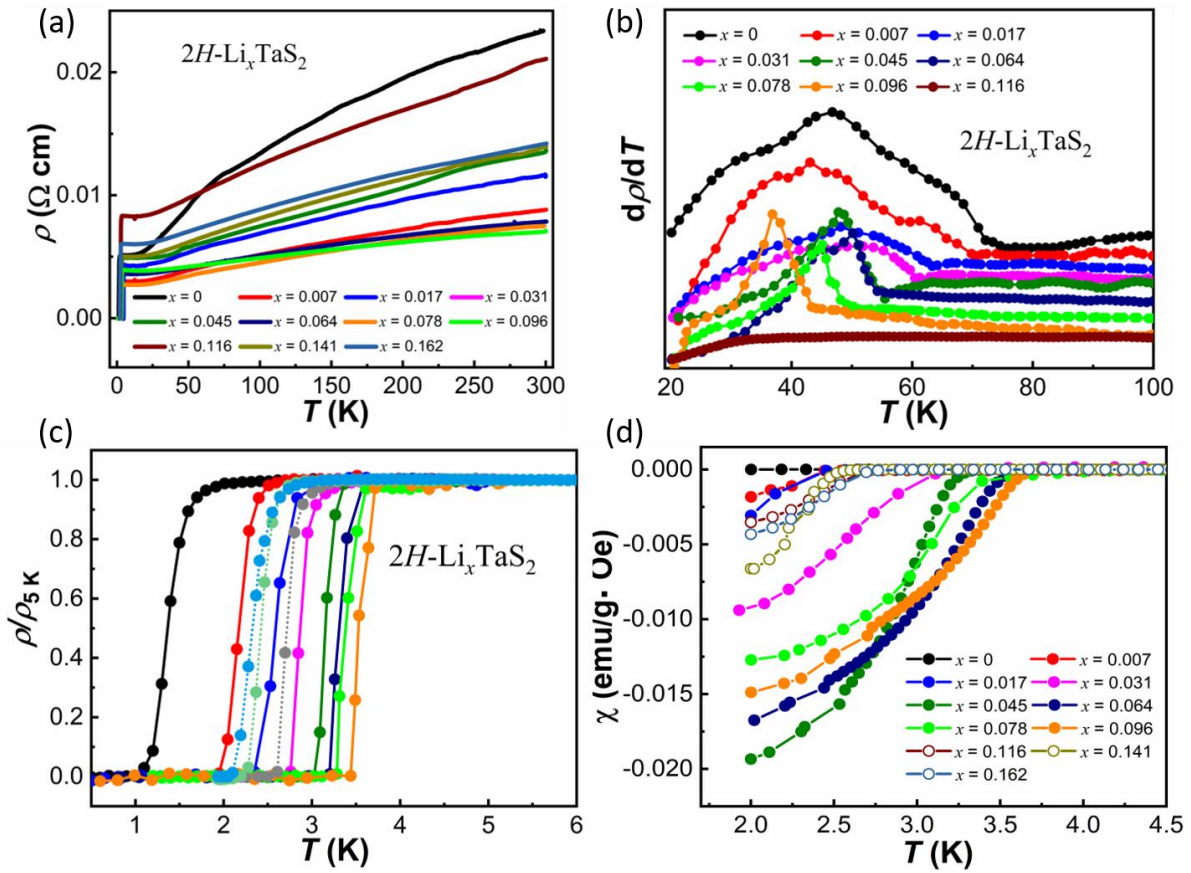


Fig. 3.2 The physical properties for all the samples of nominal composition  $2H\text{-Li}_x\text{TaS}_2$  ( $0 \leq x \leq 0.162$ ). (a) Resistivity in a temperature range between 0.5 and 300 K. (b) Temperature dependence of derivative of resistance, ranging from 20 - 100 K. Some curves have been offset for clarity. The data for  $x = 0.141$  and  $x = 0.162$  are similar to those for  $x = 0.116$  and are therefore not shown. (c) Normalized resistivity  $\rho/\rho_{5K}$ , between 0.5 and 6 K. (d) The temperature-dependent magnetic susceptibilities in 2 mT for ZFC procedures.

Figure 3.2a shows the temperature dependence of the resistivity for the low-lithium intercalation samples for temperatures ranging from 0.5 to 300 K. In the normal state, the resistivity decreases with temperature, showing weakly metallic behaviour. The parent  $2H\text{-TaS}_2$  exhibits a CDW phase transition at a temperature around 75 K, which is in agreement with the corresponding literature value[73, 107], demonstrating the high quality of the  $2H\text{-TaS}_2$  compounds. The evolution of the  $T_{\text{CDW}}$  has been deduced from the minimum in the temperature derivative of the resistivity  $d\rho(T)/dT$  with lithium-intercalation, and it turns out to be strongly reduced with increasing lithium content. The  $T_{\text{CDW}}$  is effectively suppressed by lithium intercalation from 75 K for  $x = 0$  to 41 K for  $x = 0.096$ , and vanishes with a further increase of the lithium content above  $x = 0.1$  in Fig. 3.2b. Figure 3.2c shows the transition to superconductivity for  $2H\text{-Li}_x\text{TaS}_2$  on an extended scale. The pristine  $2H\text{-TaS}_2$  shows a transition

at  $T_c \approx 1.2$  K ( $T_c$  defined by a 50% criterion), which is similar to the reported results of  $T_c$  with zero resistance  $\sim 0.7$  K (Fig. 1.11a) [94]. The  $T_c$  is also determined from the ZFC magnetization by the onset temperature of diamagnetism (Fig. 3.2d), consistent with that of electrical transport. Upon lithium-intercalation,  $T_c$  increases and the CDW ordering temperature  $T_{CDW}$  decreases with increasing  $x$ , demonstrating that there is a correlation between the coexisting superconductivity and CDW phases. The  $T_c$  reaches a maximum of about 3.5 K for  $x = 0.096$  and then decreases for higher lithium contents, which could be attributed to the formation of  $\text{Li}_x(\text{H}_2\text{O})_y$  as a new intercalator, as mentioned above. The resulting phase diagram is summarized and shown in Fig. 3.3, which agree with the electronic phase diagram of  $2H\text{-TaSe}_{2-x}\text{S}_x$ [66].

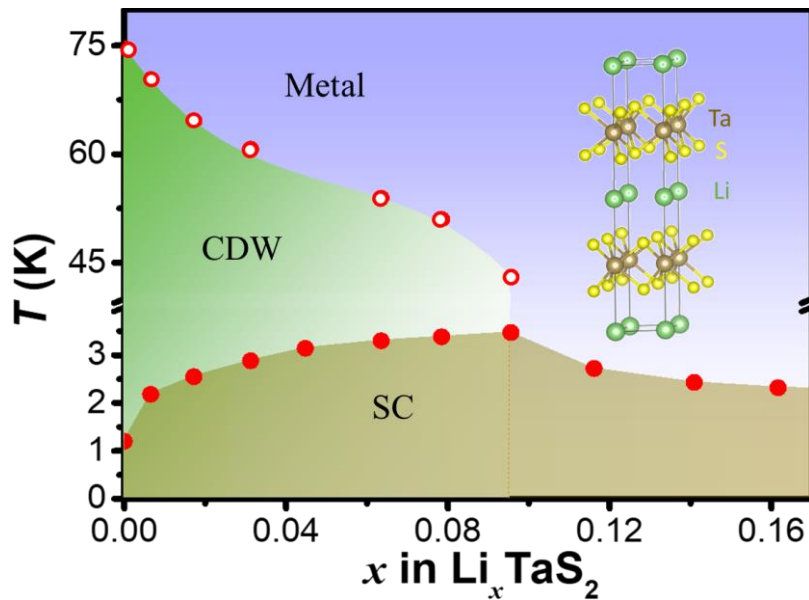


Fig. 3.3 The electronic phase diagram for  $\text{Li}_x\text{TaS}_2$ . The open circles represent the CDW transition temperature, and the filled circles correspond to the superconducting transition temperature. Inset: Crystal structure of  $2H\text{-Li}_x\text{TaS}_2$ .

### 3.3.3 Hall resistivity

Both the CDW state and superconductivity are closely related to the conduction electrons[108, 109]. Hall resistivities were measured to estimate the carrier type and density and to further reveal the electronic effect of lithium-intercalation on CDW and superconductivity in  $2H\text{-Li}_x\text{TaS}_2$ [67]. As the samples with high lithium content became quite unstable it was difficult to obtain large enough crystals. The Hall resistivity was therefore only measured on single crystals with low lithium content, In Figs. 3.4a-b for undoped  $2H\text{-TaS}_2$  and  $2H\text{-Li}_{0.007}\text{TaS}_2$  crystals, respectively. The magnetic field dependent Hall resistivity  $\rho_{xy}$  shows an ideal linear dependence, which allows to evaluate the carrier density in a simple single-band model[110]. These results

are summarized in Fig. 3.4c. The temperature dependent carrier densities of undoped 2H-TaS<sub>2</sub> crystals show a sudden change both in the magnitude and sign as the temperature approaches  $T_{CDW}$ , which is similar to reports on 2H-TaS<sub>2</sub>, NbSe<sub>2</sub> and YBa<sub>2</sub>Cu<sub>3</sub>O<sub>6+δ</sub>[39, 41, 43, 111].

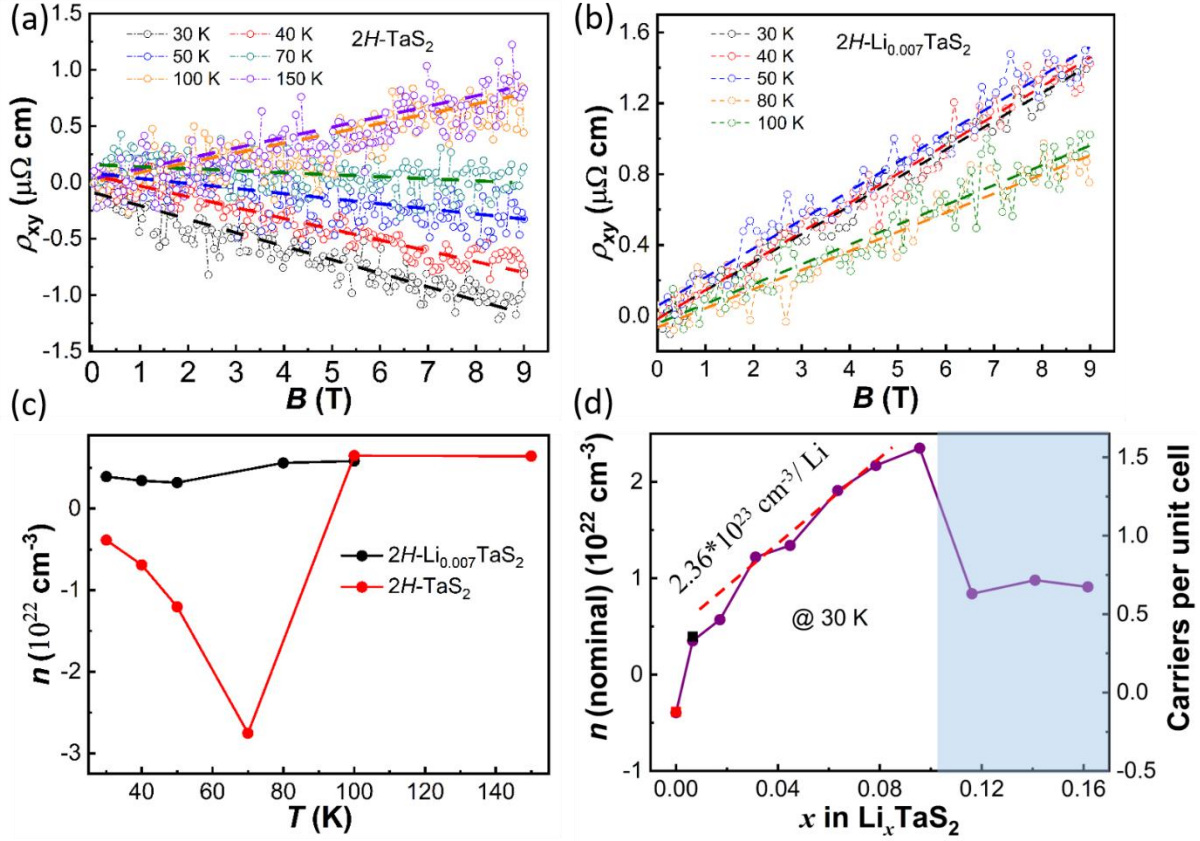


Fig. 3.4 (a) Magnetic-field dependent Hall resistance of 2H-TaS<sub>2</sub> and (b) 2H-Li<sub>0.007</sub>TaS<sub>2</sub> crystals. (c) The corresponding temperature dependent carrier densities of 2H-TaS<sub>2</sub> and 2H-Li<sub>0.007</sub>TaS<sub>2</sub> single crystals. (d) Nominal charge-carrier density and corresponding carriers per unit cell as obtained at  $T = 30$  K from 2H-Li<sub>*x*</sub>TaS<sub>2</sub> polycrystalline samples. The dashed line is linear fit to these data for  $0 < x < 0.1$ . The red and the green data point are from the data for single crystals shown in Fig. 3.4c.

Two types of charge carriers, electrons and holes, are dominating the transport behaviour below and above the CDW phase transition, respectively. For the 2H-Li<sub>0.007</sub>TaS<sub>2</sub> crystals, however, the positive Hall resistivity indicates that the dominant carriers are holes in this system[112]. An associated comparably small change in carrier density between 60 and 80 K also confirms the CDW transition, in a similar way as it has been observed in 2H-Cu<sub>0.03</sub>TaS<sub>2</sub>[100] and 2H-In<sub>0.5</sub>TaS<sub>2</sub>[113]. The carrier density measured on single-crystalline 2H-Li<sub>0.007</sub>TaS<sub>2</sub> is somewhat larger ( $\approx 3.95 \times 10^{21}$  holes cm<sup>-3</sup> at  $T = 30$  K) as compared to undoped 2H-TaS<sub>2</sub> ( $\approx 3.86 \times 10^{21}$  electrons cm<sup>-3</sup> at  $T = 30$  K), which would correspond to  $\approx 0.23$  and  $0.22$  charge carriers per unit cell, respectively. In the CDW state above  $T_{CDW}$ ,  $n$  is of the order of  $\approx 5 \times 10^{21}$  cm<sup>-3</sup> for both compositions, which corresponds to  $\approx 0.3$  hole-like carriers per unit cell.

To obtain a systematic trend as a function of lithium content  $x$ , Hall effect measurements were also performed on polycrystalline samples at  $T = 30$  K. The absolute values of the corresponding numbers must be taken with the reservation that Hall measurements on polycrystals can be affected by anisotropy and grain-boundary effects[114, 115]. Nevertheless, as all the samples were prepared in a similar manner, a clear trend still can be identified. The data shown in Fig. 3.4d indicate that there is an almost linear increase in  $n$  as a function of lithium content up to  $x = 0.096$ , and a sudden drop for larger values of  $x$ , which is not unexpected due to the changes in the crystal structure as discussed above. Using these estimates based on the linear fitting in Fig. 3.4d, the hypothetical intercalation of one lithium atom would correspond to a change in  $n$  by  $\approx 14$  carriers per formula unit. Therefore, the lithium intercalation does not primarily act as a mechanism for carrier doping, but most probably leads to a weakening of the CDW state, which indirectly results in an increase of the density of mobile charge carriers with a resulting boost of superconductivity.

### 3.3.4 Superconducting characteristic parameters

To study the physical properties of lithium-intercalated 2H-TaS<sub>2</sub> superconductors in more detail, the intrinsic 2H-TaS<sub>2</sub> ( $T_c \approx 1.2$  K) was chosen for comparison with 2H-Li<sub>0.096</sub>TaS<sub>2</sub> (with a maximum  $T_c \approx 3.5$  K). Detailed measurements of the field dependence of the resistive transition to superconductivity and the magnetization are presented in Fig. 3.4. The effect of applying a magnetic field on  $T_c$  for the  $x = 0$  and  $x = 0.096$  samples is shown in Figs. 3.4a and 3.4b, respectively. As expected,  $T_c$  is gradually suppressed and the width of the superconducting transition increases as the magnetic field is increased. The resulting temperature dependence of the upper-critical fields  $B_{c2}(T)$  are shown in Fig. 3.4c. The extrapolated slopes are  $dB_{c2}/dT = -1.41$  T/K and  $dB_{c2}/dT = -1.78$  T/K for  $x = 0$  and  $x = 0.096$ , respectively. The upper-critical fields at zero temperature  $B_{c2}(0)$  can be estimated using the Werthamer-Helfand-Hohenberg (WHH) approximation in the dirty limit[96, 116],

$$B_{c2}^{WHH}(0) = -0.69T_c \left( \frac{dB_{c2}}{dT} \right)_{T=T_c} \quad (3-1)$$

to  $B_{c2}^{WHH}(0) \approx 1.17$  T for  $x = 0$ , and  $B_{c2}^{WHH}(0) \approx 4.24$  T for  $x = 0.096$ . From  $B_{c2} = \Phi_0/2\pi\xi(0)^2$ , the corresponding superconducting coherence lengths can be estimated,  $\xi(0) = 16.8$  nm, and 8.8 nm, respectively.

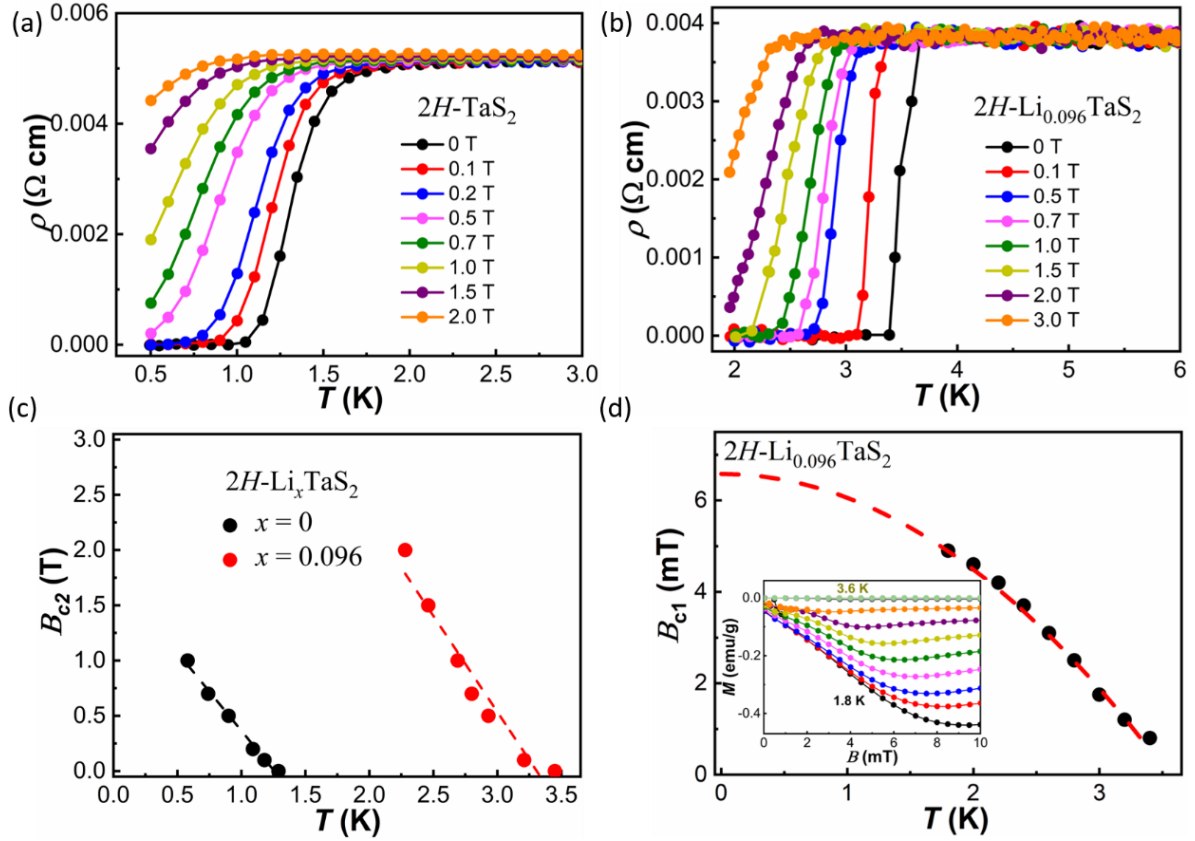


Fig. 3.4 (a) and (b) field-dependent resistivity measurements for the samples  $x = 0$  and  $x = 0.096$ . (c) The dashed lines indicate the extrapolated slopes  $dB_{c2}/dT$  used for the WHH approximation. (d) The temperature dependence of the lower critical field  $B_{c1}$  for  $x = 0.096$ . Lower inset: the ZFC field dependence of the magnetization  $M(B)$  for temperatures between 1.8 and 3.6 K (in 0.2 K steps) in magnetic fields  $B$  between 0 and 10 mT.

The ZFC field dependence of the magnetization  $M(B)$  for temperatures between 1.8 and 3.6 K is shown in Fig. 3.4d for the  $2H\text{-Li}_{0.096}\text{TaS}_2$  sample, exhibiting typical type-II superconducting behaviour. The ZFC and FC magnetic susceptibilities measured at 2 mT are shown in the lower inset of Fig. 3.4d. By estimating the lower-critical field  $B_{c1}$  as the minimum on the  $M(B)$  curves, its temperature dependence can be well fitted using an empirical formula[117],

$$B_{c1}(T) = B_{c1}(0) \left[ 1 - \left( \frac{T}{T_c} \right)^2 \right]. \quad (3-2)$$

A resulting estimate of the corresponding lower-critical field is  $B_{c1}(0) \approx 6$  mT. Together with  $B_{c1}(T) = \frac{\Phi_0}{4\pi\lambda^2} \ln \frac{\lambda}{\xi}$ , an estimate of the London penetration depth is  $\lambda(0) \approx 310$  nm, yielding  $\kappa = \frac{\lambda(0)}{\xi(0)} \approx 35.2$ , confirming that the material is a strongly type-II superconductor.

### 3.3.5 Heat capacity

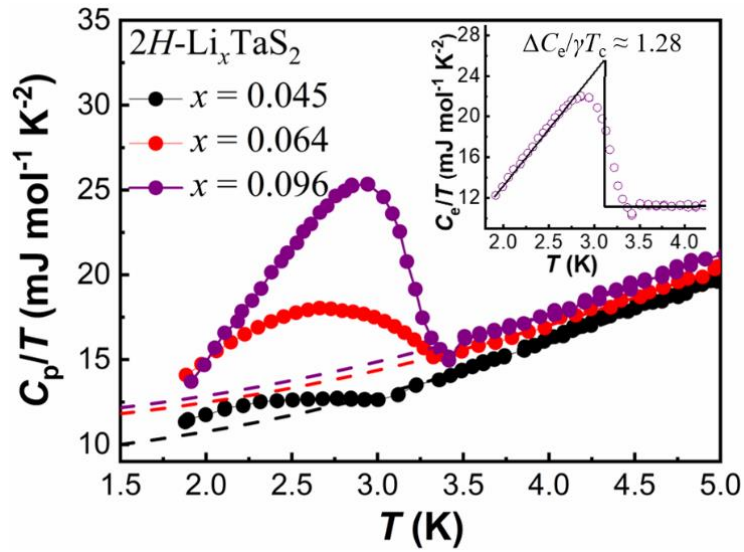


Fig. 3.5 Specific-heat  $C/T$  for  $2H\text{-Li}_x\text{TaS}_2$  with different lithium content  $x$ . Right inset: The solid line shows an entropy-conserving construction to obtain  $C_e/\gamma T_c$  for an optimally intercalated  $2H\text{-Li}_{0.096}\text{TaS}_2$  sample.

Table 3.1. Electronic ( $\gamma$ ) and lattice ( $\beta$ ) contributions according to a fit to Eq. (3-3). We obtained the calculated values  $\gamma_c$  from the free-electron model using the measured carrier densities  $n$ .

$x$	$\beta$ (mJ/mol K <sup>4</sup> )	Carrier density $n$ (cm <sup>-3</sup> )	Calculated $\gamma_c$ (mJ/mol K <sup>2</sup> )	Experimental $\gamma_c$ (mJ/mol K <sup>2</sup> )	Effective mass
0	0.35	$3.5 \times 10^{21}$	0.88	8.5	9.66
0.045	0.41(3)	$7.6 \times 10^{21}$	1.14	9.0	7.90
0.064	0.39(1)	$1.05 \times 10^{22}$	1.27	10.9	8.59
0.096	0.40(2)	$2.2 \times 10^{22}$	1.6	11.2	7

The low-temperature specific heats of the  $2H\text{-Li}_x\text{TaS}_2$  samples ( $x = 0.045, 0.064, 0.096$ ) are shown in Fig. 5. As expected, the specific-heat data show a peak at  $T_c \approx 2.9$  K, 3.3 K and 3.5 K, respectively. These results are consistent with the data from the transport measurements. The normal-state specific heat can be fitted by a standard expression at low temperatures,

$$\frac{c}{T} = \gamma + \beta T^2, \quad (3-3)$$

where  $\gamma$  is the Sommerfeld constant, which is proportional to the electron density of states  $\text{DOS}(E_F)$  at the Fermi level. The fitted values of  $\beta$  for all selected samples are close to 0.4 mJ/mol K<sup>4</sup> (see Table 3.1), as reported for  $\text{Cu}_x\text{TaS}_2$  and  $\text{Cu}_x\text{TiSe}_2$ [67, 87], corresponding to a

Debye temperature  $\Theta_D$  of  $\sim 244$  K from the corresponding three-dimensional Debye model via  $\beta = 12\pi^4 nR/5\Theta_D^3$ , where  $n$  is the number of atoms per formula unit and  $R$  is the gas constant. The resulting electronic contributions to the specific heat for these lithium-intercalated samples increase with lithium content and are slightly larger than that of the parent compound 2H-TaS<sub>2</sub> ( $\gamma = 8.5$  mJ/mol K<sup>2</sup>)[73, 118]. These results demonstrate that the lithium intercalation increases, along with the charge-carrier density  $n$ , also the  $DOS(E_F)$ . We state here that the measured values for  $\gamma$  of the order of 10 mJ/mol K<sup>2</sup> are far larger than one can expect from a simple free-electron model. Assuming one charge carrier per unit cell, we obtain with  $\gamma_c = \pi^2 k_B^2 DOS(E_F)/3$  and  $DOS(E_F) = (3n/\pi)^{1/3} m_e / (\pi \hbar^2)$  a calculated value  $\gamma_c$  of the order of 1.5 mJ/mol K<sup>2</sup> only, which may hint at an enhanced effective mass in superconducting 2H-Li<sub>*x*</sub>TaS<sub>2</sub> (see Table I). Here,  $k_B$  is the Boltzmann constant,  $m_e$  the electron mass, and  $\hbar$  the reduced Planck constant. The corresponding effective mass enhancements estimated from the measured carrier densities and the specific heat data are all of the order of  $\approx 7$ -9 (see Table I). The right inset of Fig. 5 shows the discontinuity in the electronic specific heat ( $C_e/T_c$ ) at the superconducting transition with the phonon contribution subtracted and with a BCS entropy-conserving construction. The obtained ratio  $\Delta C_e/\gamma T_c = 1.28$  is very close to the standard BCS value of 1.43, thereby qualifying 2H-Li<sub>*x*</sub>TaS<sub>2</sub> as a weakly-coupled superconductor[9].

### 3.4 Summary

All the electrical transport results are summarized in the electronic phase diagram of 2H-Li<sub>*x*</sub>TaS<sub>2</sub> (Fig. 3.3), which shows the evolution of the superconducting, CDW and metallic phases with varying lithium content  $x$ . The superconducting and CDW states are interrelated and coexist with each other. The lithium intercalation gradually enhances the superconducting transition temperature and weakens the CDW state. At  $x \approx 0.096$ , the CDW phase is fully suppressed, and superconductivity reaches its maximum critical temperature  $T_c = 3.5$  K, with a completely developed discontinuity in the specific heat which is compatible with a weak-coupling scenario. The changes upon lithium intercalation are accompanied by an increase of the hole-type carrier density. However, the measured changes in the charge carrier densities are too large to be explained by doping alone. Therefore, lithium intercalation leads primarily to a weakening of the CDW state, which then indirectly causes an increase of the density of mobile hole-type charge carriers.



### **3.5 Related Publication**

*Superconductivity and charge density wave formation in lithium-intercalated 2H-TaS<sub>2</sub>*

Huanlong Liu, Shangxiong Huangfu, Xiaofu Zhang, Hai Lin, and Andreas Schilling

Physical Review B 104, 064511 (2021)

DOI: 10.1103/PhysRevB.104.064511

## Chapter 4

### Superconductivity in hydrated $\text{Li}_x(\text{H}_2\text{O})_y\text{TaS}_2$

In a few cases, interlayer water has been shown to be crucial for the formation of superconductivity, such as in  $\text{Na}_x\text{CoO}_2 \cdot 1.3\text{H}_2\text{O}$  [119, 120], by enhancing the two-dimensionality and possibly inducing antiferromagnetic spin correlations[121]. To investigate the synergistic effects of interlayered water and intercalated lithium, the structural and physical properties of the hydrated  $\text{Li}_x(\text{H}_2\text{O})_y\text{TaS}_2$  ( $0.22 \leq x \leq 0.58$ ,  $y \approx 0.86$ ) have been systematically studied. Comprehensive transport measurements reveal that the transition temperature to superconductivity shows a dome-shaped dependence on the lithium content  $x$  with a maximum  $T_c$  of 4.6 K. From the corresponding Sommerfeld constants  $\gamma$  and Debye temperatures  $\Theta_D$  estimated by heat capacity data, the electron-phonon coupling parameters  $\lambda_{ep}$  and the  $\text{DOS}(E_F)$  can be derived as functions of  $x$ . While the variation of the  $\text{DOS}(E_F)$  is consistent with that of  $T_c$ , indicating that the lithium-intercalation is tuning  $T_c$  by changing the  $\text{DOS}(E_F)$  in  $2H\text{-Li}_x(\text{H}_2\text{O})_y\text{TaS}_2$ , the simultaneous changes of  $\lambda_{ep}$  and  $\Theta_D$  may also play a certain role.

#### 4.1 Introduction

As mentioned in chapter 3.1, in the alkali-metal or transition-metal atom-intercalated TMDs, the enhancement of superconductivity is fairly well-understood[68, 122]. The evolution of superconductivity can be explained by the suppression of the CDW state[62], or in the rigid-band model of the band structure[70]. For simple inorganic metal-intercalated  $2H\text{-TaS}_2$ , the  $T_c$  of the optimally intercalated samples can generally reach the maximum as the CDW is sufficiently suppressed, and then decreases with further increasing the intercalation level, thereby forming a dome-shaped  $T_c$  dependence on the intercalation level[42], which is similar to the pressure dependence of  $T_c$  seen in high-pressure experiments on  $2H\text{-TaS}_2$ [68, 72, 107]. On the contrary, when an extended organic- or inorganic-chemical group intercalant enters the interlayer of  $2H\text{-TaS}_2$ , the enhanced superconductivity is always accompanied by the complete disappearance of the CDW state[123, 124].

It is very likely that the charge transfers from such intercalants to the Ta-S layer increases the  $\text{DOS}(E_F)$ . The superconducting transition temperatures of the hydrated phases  $\text{A}_x(\text{H}_2\text{O})_y\text{TaS}_2$  can be much higher than those with the same doping level in  $\text{A}_x\text{TaS}_2$  ( $\text{A} = \text{Li}, \text{Na}, \text{K}, \text{Rb}$ ;  $x \geq$

0.33)[96, 125]. Taking lithium-intercalation as an example, the rigid-band model indicates that the intercalant does not significantly change the band structure of  $2H\text{-TaS}_2$ [70]. The DOS has a peak at the Fermi level, and the Fermi energy is located nearly in the center of the conduction band, which is dominated by the half-filled Ta  $5d_{z^2}$  band[102, 126, 127]. This band structure is hardly changed at the CDW transition, or even in a thinned monolayer. The Fermi level of the hydrated  $\text{A}_x(\text{H}_2\text{O})_y\text{TaS}_2$  moves from the center to the near the top of the  $d_{z^2}$  band upon charge transfer from the intercalant to the conduction band, leading to a decrease of  $\text{DOS}(E_F)$ , which should be detrimental to superconductivity[128, 129]. The above scenario based on the rigid-band theory apparently fails to account for the experimentally observed distinctly enhanced superconducting transition temperatures of the hydrates which are higher than those of the anhydrates[130]. Undoubtedly, interlayer water molecules are favourable for superconductivity in  $2H\text{-TaS}_2$ . However, whether the enhancement of  $T_c$  is due to the possible enlargement of the interlayer spacing[131], which in turn weakens the interlayer coupling of the Ta-S layers[103], or due to the shielding of the random Coulomb potential[102], is still a matter of debate.

## 4.2 Experiments

The  $\text{Li}_x\text{TaS}_2$  powders were obtained by solid-state reaction as described in chapter 3.2. The resulting  $2H\text{-Li}_x\text{TaS}_2$  samples were exposed to air (relative humidity  $\sim 31\%$ ) to form  $\text{Li}_x(\text{H}_2\text{O})_y\text{TaS}_2$ , and then stored in a glove box filled with argon.

The water content  $y$  was determined by thermogravimetric analysis in an argon atmosphere with details given in chapter 2.2.1. The other experimental characterization techniques in this chapter are the same as in chapter 3.2.

## 4.3 Results and discussion

### 4.3.1 Crystal structure

As shown in Fig. 4.1a, the PXRD patterns are characterized at room temperature for all  $\text{Li}_x(\text{H}_2\text{O})_y\text{TaS}_2$  samples and show a similar crystal structure with the space group of  $P6_3/mmc$ [59]. To more clearly reveal the structural differences between the  $\text{Li}_x(\text{H}_2\text{O})_y\text{TaS}_2$  compounds, a detailed refinement has been performed on all PXRD patterns using Fullprof[105] and *autoFP* packages. The Rietveld refinement of the PXRD pattern of hexagonal  $\text{Li}_{0.31}(\text{H}_2\text{O})_y\text{TaS}_2$  is shown in Fig. 4.1(b). The relative coordinates in the Ta-S layer of the  $\text{Li}_{0.31}(\text{H}_2\text{O})_y\text{TaS}_2$  compound are the same as those of  $2H\text{-TaS}_2$ . The corresponding data are presented in Table 4.1[59]. The Ta atoms bond with six surrounding S atoms to form a  $[\text{TaS}_6]$

triangular prism, and a co-edged connection to construct the  $\text{TaS}_2$  layer. The interlayer spacing of about  $5.8 \text{ \AA}$  for the  $\text{Li}_x(\text{H}_2\text{O})_y\text{TaS}_2$  compounds is much larger than that of  $2\text{H-Li}_x\text{TaS}_2$  ( $\sim 3.4 \text{ \AA}$ )[122], which indicates the presence of interlayer water. The crystal structure with the possible position of the water molecule is qualitatively shown in the inset of Fig. 4.1b, although the exact positions of the hydrogen and oxygen atoms are unknown[132]. The lithium contents of these polycrystalline hydrated  $\text{Li}_x(\text{H}_2\text{O})_y\text{TaS}_2$  samples have been measured by ICP-MS measurements. The refinement results of the lattice parameters are displayed in Fig. 4.1c. The lattice parameter  $c$  gradually decreases with increasing lithium content when compared with  $2\text{H-TaS}_2$ , and shows a significant change for  $x > 0.42$ . A linear trend of a slight expansion is observed for the Ta-S layer, showing a simultaneous contraction of interlayer spacing with increasing the lithium content, which is similar to  $2\text{H-Li}_x\text{TaS}_2$ [122], and is another manifestation of the evolution of the lithium content in  $\text{Li}_x(\text{H}_2\text{O})_y\text{TaS}_2$  samples.

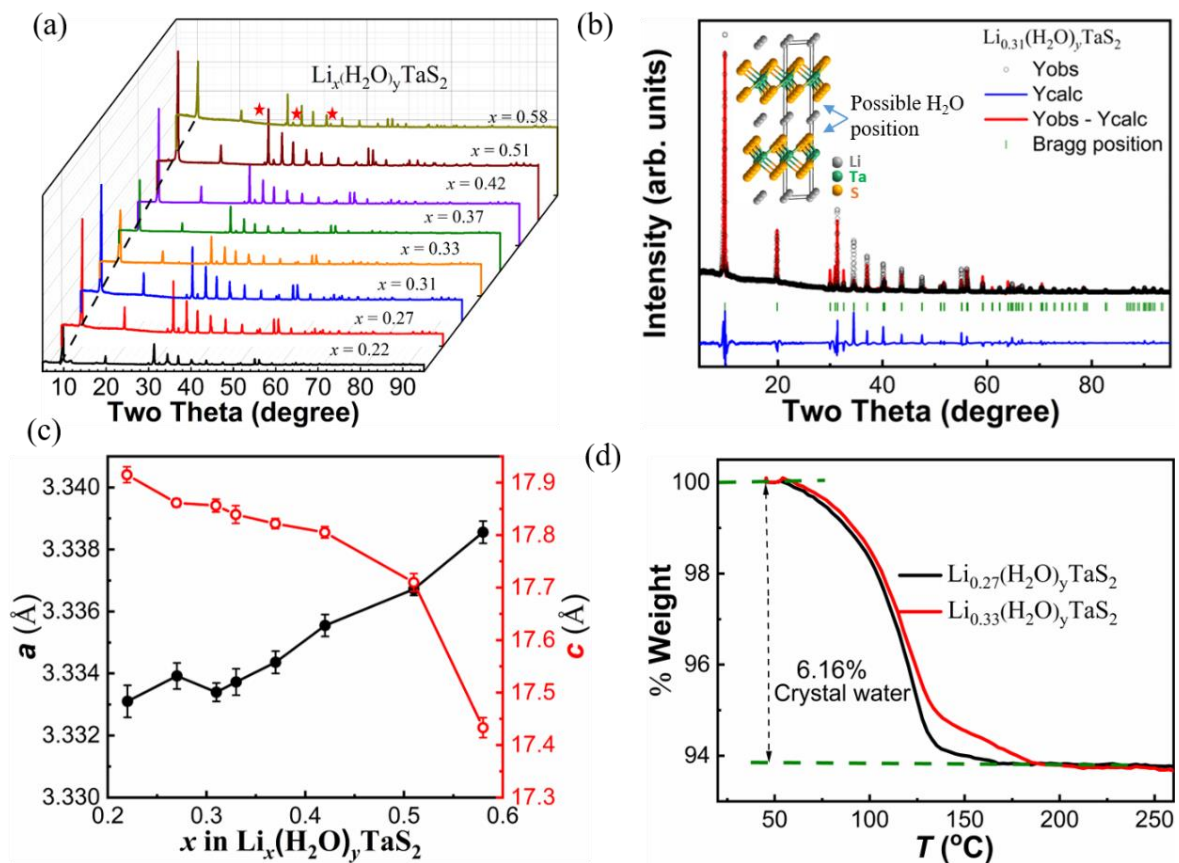


Fig. 4.1 (a) The PXRD pattern at room temperature for all samples of  $\text{Li}_x(\text{H}_2\text{O})_y\text{TaS}_2$  ( $0.22 \leq x \leq 0.58$ ). (b) The PXRD pattern of  $\text{Li}_{0.31}(\text{H}_2\text{O})_y\text{TaS}_2$ . The black dots are the observed data, while the red solid line represents the calculated intensities. The bottom blue solid line is the difference between the observed and calculated intensities. Inset: Crystal structure of  $\text{Li}_{0.31}(\text{H}_2\text{O})_y\text{TaS}_2$  along the  $ab$ -plane. (c) The variation of lattice parameters for  $\text{Li}_x(\text{H}_2\text{O})_y\text{TaS}_2$  samples. (d) The weight loss of  $\text{Li}_x(\text{H}_2\text{O})_y\text{TaS}_2$  ( $x = 0.27$  and  $0.33$ ) samples versus temperature in an argon environment.

The thermogravimetric analysis of the selected  $\text{Li}_x(\text{H}_2\text{O})_y\text{TaS}_2$  ( $x = 0.27, 0.33$ ) samples in an argon atmosphere (Fig. 4.1d) shows that the weight of the samples decreases, and then stabilizes with increasing temperature. The interlayered crystal water content is essentially constant, namely  $\approx 0.86$  per formula unit, despite the differences in lithium content in the  $\text{Li}_x(\text{H}_2\text{O})_y\text{TaS}_2$  samples, and is also close to the reported results for  $\beta\text{-Na}_{1/3}(\text{H}_2\text{O})_{0.77-0.87}\text{TaS}_2$ [96, 98, 129, 133]. In principle, the intercalated water content can be related not only to the lithium content but also to the air humidity[98, 128]. However, for the present conditions and when the lithium content is below  $x \approx 0.08$ , any absorbed water must enter the Ta-S layers on interstitial sites, as it does not qualitatively affect the crystal structure. Preliminary data indicate the presence of one  $\text{H}_2\text{O}$  interlayer for  $0.08 < x < 0.22$ , and of possibly two  $\text{H}_2\text{O}$  interlayers for higher lithium contents.

Table 4.1 Fractional atomic and occupancy factors for  $\text{Li}_{0.31}(\text{H}_2\text{O})_y\text{TaS}_2$  ( $R_{\text{wp}} = 8.047\%$ ,  $\chi^2 = 2.30$ ). For this fit, the positions and occupancies of the light H and O atoms were omitted.

Atom	Wyckoff position	x	y	z	Occ.
Ta	2b	0	0	0.2500	1
S	4f	0.3333	0.1667	0.6180(4)	1
Li	2a	0	0	0	0.31

### 4.3.2 Electrical transports and magnetism

To investigate the effect of lithium-intercalation into the hydrated phase  $\text{Li}_x(\text{H}_2\text{O})_y\text{TaS}_2$  on superconductivity, the resistivities  $\rho(T)$  at temperatures ranging from 1.8 to 300 K are shown in Fig. 4.2a for all  $\text{Li}_x(\text{H}_2\text{O})_y\text{TaS}_2$  samples. All samples show a weakly metallic behaviour, which is similar to that of the parent  $2H\text{-TaS}_2$  discussed in the above chapter 3.3.2. The typical CDW-like kink in the  $\rho(T)$  dependence completely disappears in the normal state for all samples when compared with the CDW transition temperature of  $\sim 75$  K for  $2H\text{-TaS}_2$ [134]. The disappearance of the CDW transition may be due to the large amounts of intercalated lithium[87]. However, the interlayer spacing is also largely expanded by the water intercalation, which reduces the dimensionality and tends to suppress the CDW as well[131, 135, 136]. The detailed normal-to-superconducting transitions are shown in Fig. 4.2b. The transition temperatures were determined by a 50% criterion and, alternatively, by the onset of the drop from the normal-state trend lines ( $T_c^{\text{on}}$ ). They first increase from  $T_c \approx 2.8$  K to  $\approx 4.5$  K ( $T_c^{\text{on}} \approx$

5.0 K), and then fall to  $\approx 2.1$  K ( $T_c^{on} \approx 2.9$  K), forming a dome-like behaviour with increasing intercalated lithium content in hydrated  $\text{Li}_x(\text{H}_2\text{O})_y\text{TaS}_2$ , which is similar to the case of several families of high- and low-temperature superconductors[83, 137, 138].

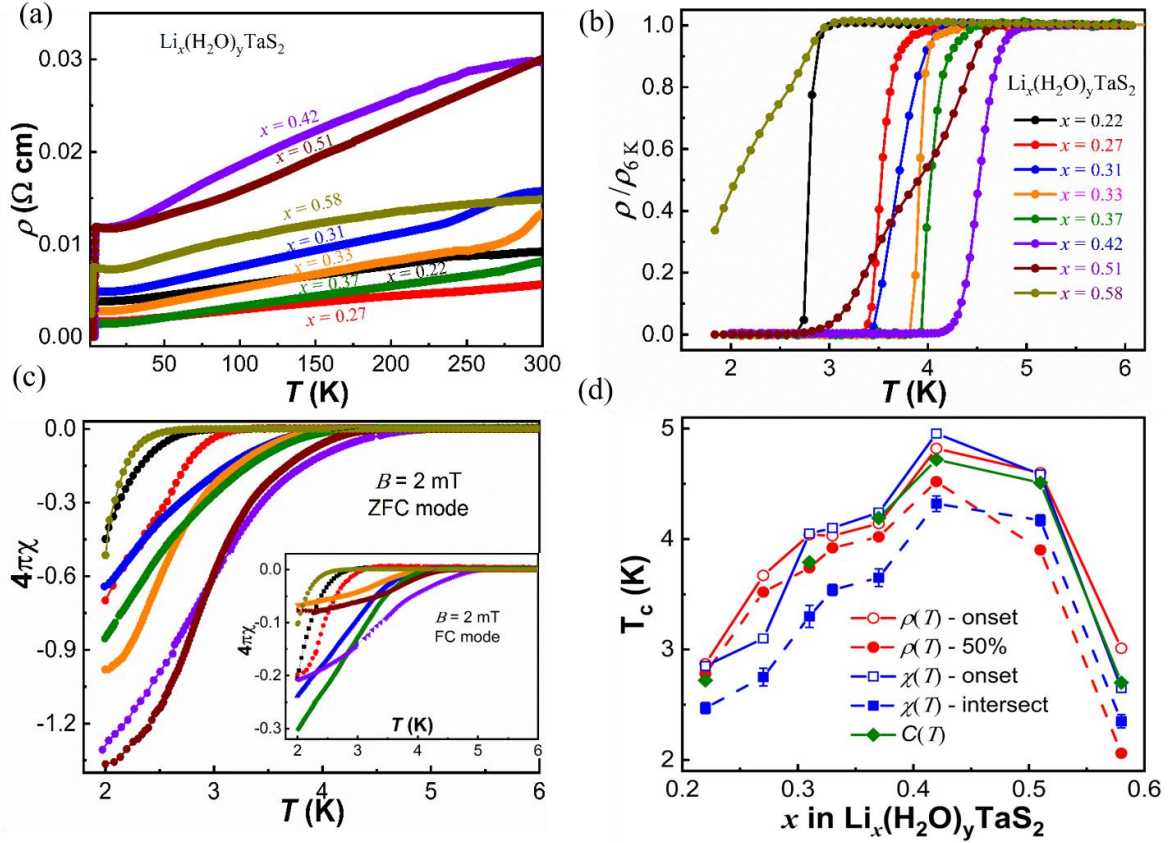


Fig. 4.2 The physical properties of  $\text{Li}_x(\text{H}_2\text{O})_y\text{TaS}_2$  samples. (a) Resistivity data in a temperature range between 1.8 and 300 K. (b) The resistivities  $\rho/\rho_{6\text{K}}$  between 1.8 and 6 K, showing the transitions to superconductivity. The dashed line denotes the 50% criterion used to determine  $T_c$ , while the arrows indicate the onset temperatures  $T_c^{onset}$  here the  $\rho(T)$  curves start to drop from the normal-state trendlines. (c) The temperature-dependent magnetic susceptibilities for ZFC and FC procedures (inset), respectively. (d) The  $T_c$  as determined by 50% of the normal resistivity (“ $\rho(T)$ -50%”), by the onset temperature of the resistivity drops (“ $\rho(T)$ -onset”), by corresponding data from FC susceptibility (steepest-slope method and onset temperature of diamagnetism, “ $\chi(T)$ -intersect” and “ $\chi(T)$ -onset”, respectively), and from the heat-capacity data (“ $C(T)$ ”).

The temperature-dependent DC magnetic susceptibilities of hydrated  $\text{Li}_x(\text{H}_2\text{O})_y\text{TaS}_2$  are shown in Fig. 4.2c, measured in an external magnetic field of 2.0 mT and using the ZFC and FC procedures. The  $T_c$  is determined from the FC magnetization either by defining the intersection of the extrapolated normal-state magnetic susceptibility with the steepest slope line of the superconductivity signal, or alternatively by the onset temperature of diamagnetism. The results from all magnetic susceptibility and resistivity data are shown in Fig. 4.2d, all in good agreement with the corresponding  $T_c$  data from the heat-capacity measurements to be discussed

further below. Lithium-intercalation is therefore an effective way to tune superconductivity in hydrated  $\text{Li}_x(\text{H}_2\text{O})_y\text{TaS}_2$  in a controllably manner.

### 4.3.3 Superconducting characteristic parameters

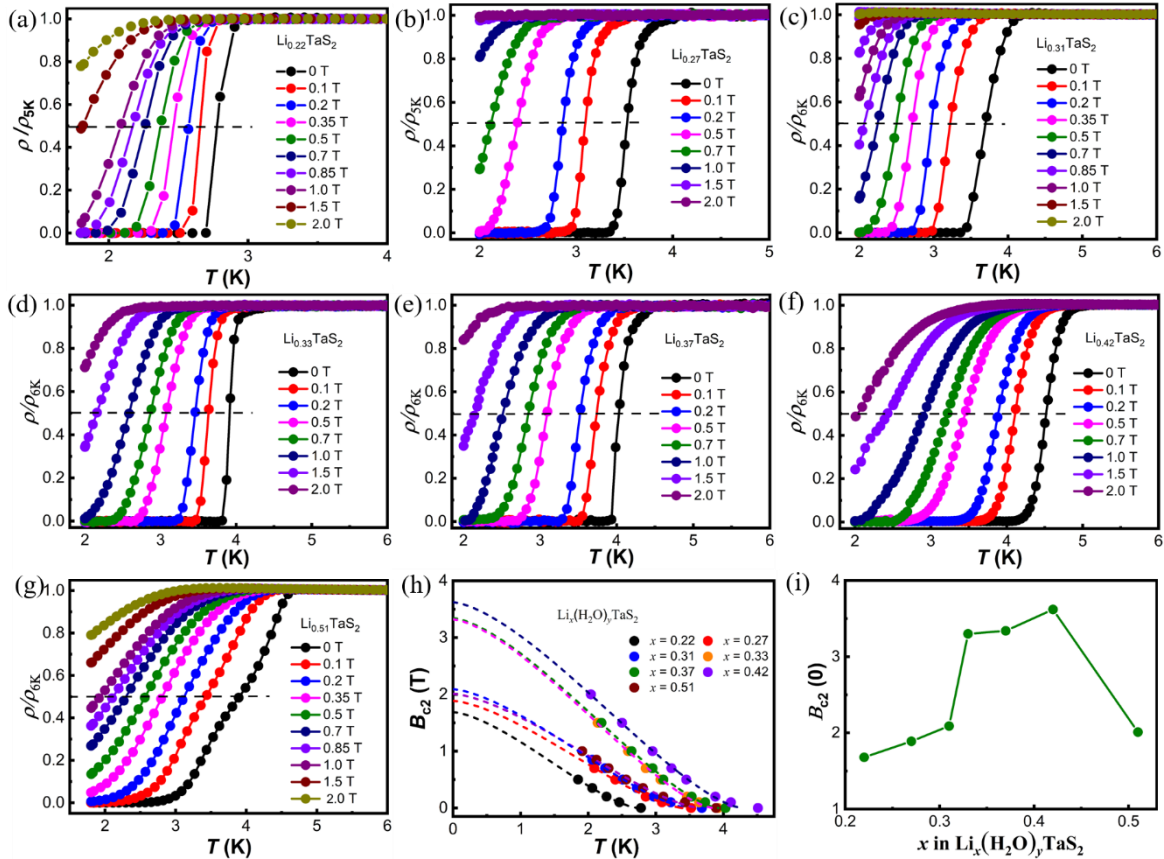


Fig. 4.3 (a-g) Temperature dependence of the resistivity of  $\text{Li}_x(\text{H}_2\text{O})_y\text{TaS}_2$  ( $0.22 \leq x \leq 0.51$ ) for various magnetic fields. The dashed line corresponds to the 50% criterion used to evaluate  $B_{c2}$ . (h) The estimation of the upper-critical field for  $\text{Li}_x(\text{H}_2\text{O})_y\text{TaS}_2$  ( $0.22 \leq x \leq 0.51$ ). (i) The respective extrapolated values of the upper-critical fields at  $T = 0$ .

In Figs. 4.3a-4.3g, we show the magnetic field dependence of the resistivity is characterized for all intercalated  $\text{Li}_x(\text{H}_2\text{O})_y\text{TaS}_2$  ( $0.22 \leq x \leq 0.51$ ) samples. As the magnetic field is gradually increased to  $B \leq 2.0$  T, the  $\rho(T)$  curves show a systematic shift to low temperatures along with a certain field-induced broadening, which is not uncommon in layered superconductors. For simplicity, the corresponding upper-critical fields  $B_{c2}(T)$  are evaluated using the 50% criterion. A corresponding determination of  $B_{c2}$  from the magnetization  $M(B)$  data as shown later in Fig. 4.4b is less definite because the transition is very broad in high magnetic fields, but it yields consistent  $B_{c2}$  values (see below). The respective temperature dependent critical fields for all investigated samples are summarized in Fig. 4.3h. The critical field  $B_{c2}(T)$  has a positive curvature as a function of temperature, which has also been found in other superconductors,

such as organic-intercalated  $\text{TaS}_2$ [43], and  $\text{MgB}_2$ [139, 140]. The polycrystalline average of the  $B_{c2}(0)$  at zero temperature can be estimated with a fit according to[141]

$$B_{c2}(T) = B_{c2}(0) \left[ 1 - \left( \frac{T}{T_c} \right)^{3/2} \right]^{3/2}. \quad (4-1)$$

The resulting  $B_{c2}(0)$  values are higher than the reported upper-critical field of 1.17 T for the pristine  $2H\text{-TaS}_2$ , but are still smaller than the corresponding BCS weak-coupling Pauli limits ( $1.86T_c$  in Tesla) (Fig. 4.3i).

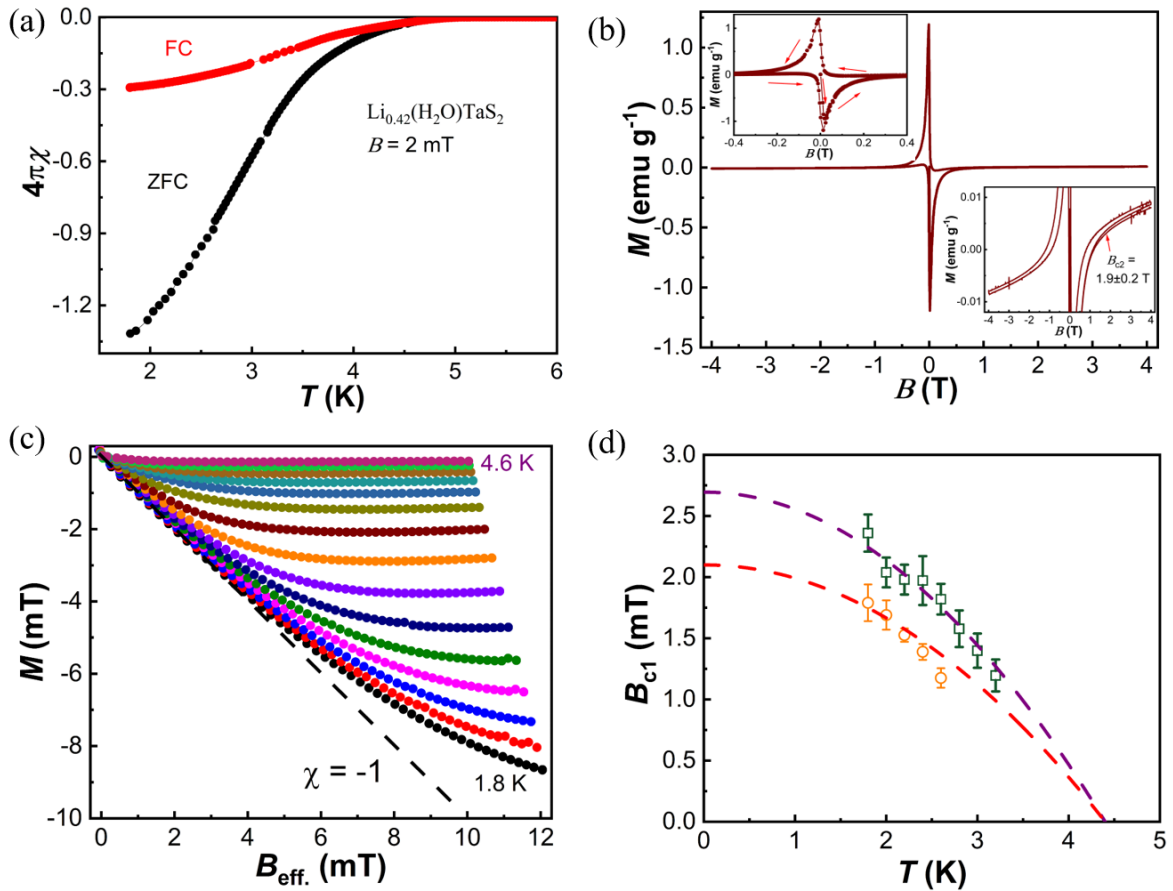


Fig. 4.4 (a) The ZFC and FC magnetic susceptibilities, and (b) measured  $M(B)$  loop at 1.8 K for optimally intercalated  $\text{Li}_{0.42}(\text{H}_2\text{O})_y\text{TaS}_2$ . Insets: Magnified views to show details. (c) The ZFC field dependence of the magnetization between temperatures 1.8 and 4.6 K (in 0.2 K steps) for  $\text{Li}_{0.42}(\text{H}_2\text{O})_y\text{TaS}_2$ . The gray dashed line shows the ideal diamagnetic shielding. (d) The evaluated  $B_{c1}$  values from Fig. 4(c) at different temperatures by methods 1 (squares) and 2 (circles) with the uncertainties from the extraction procedure drawn as error bars. The dashed lines are the fitting results using equation (4-2).

Figure 4.4a shows the Meissner (FC) and the shielding (ZFC) signals of the optimally intercalated sample with  $x = 0.42$ , measured at 2.0 mT. From the shielding fraction of 131.7% at 1.8 K obtained in the ZFC magnetic susceptibility, a demagnetization factor  $N = 0.240(8)$



can be estimated for this sample assuming an effective 100% shielding to correct all the magnetic low-field data, and all the parameters derived from it, according to  $B_{\text{eff.}} = B - N \times \mu_0 M$ . While the critical temperature as determined from the DC magnetization,  $T_c \approx 4.3\text{-}5\text{ K}$ , is consistent with  $T_c$  from resistivity data ( $\approx 4.5 - 4.8\text{ K}$ ) (see Fig. 4.2b), the calculated large effective Meissner volume of  $\sim 26\%$  even in the FC magnetic susceptibility indicates significant magnetic-flux expulsion and the good quality of the sample. The magnetization loop of  $\text{Li}_{0.42}(\text{H}_2\text{O})_y\text{TaS}_2$  at 1.8 K shows typical type-II behaviour (Fig. 4.4b and upper inset therein). The lower inset of Fig. 4.4b shows a further estimate of  $B_{c2}$  based on the first deviation of the magnetization from linearity, yielding  $B_{c2} = 1.9 \pm 0.2\text{ T}$  at 1.8 K, which is similar to the result from the magneto-transport data. In Fig. 4.4c, the field dependence of the ZFC susceptibility for  $\text{Li}_{0.42}(\text{H}_2\text{O})_y\text{TaS}_2$  is plotted in the temperature range between 1.8 and 4.6 K (in 0.2 K steps). The dashed line shows the ideal linear behavior of the Meissner state ( $\chi = -1$ ).

To obtain an estimate for the polycrystalline average of the lower critical fields  $B_{c1}$ , one can determine the  $B_{c1}$  from the magnetic fields where the  $M(B_{\text{eff.}})$  curves in Fig. 4.4c first deviate from linearity at different temperatures (here referred to as “method 1”). An improved approach, incorporating concepts of the Bean critical-state model for the mixed state and making corresponding assumptions on the mechanism of magnetic-flux penetration allows one to quantitatively fit the deviation  $\delta M(B_{\text{eff.}})$  from a linear  $M(B_{\text{eff.}})$  to extract  $B_{c1}$  (Ref. [142], here referred to as “method 2”). A work including in addition the effect of Bean-Livingston barriers (Ref. [143], “method 3”) suggests an improved fitting procedure of  $\delta M(B_{\text{eff.}})$  to eliminate this effect, at least at low temperatures. The resulting  $B_{c1}$  values obtained by methods 1 and 2 are shown in Fig. 4.4d, while the attempts to fit the  $\delta M(B_{\text{eff.}})$  data according to method 3 (which aimed to include edge-barrier effects) did not result in physically reasonable quantities. In this way the corresponding upper limits of  $B_{c1}(0)$  can still be derived from the empirical formula Eq. (3-2) in above chapter 3.3.4 with  $B_{c1}(0) \approx 2.7\text{ mT}$  (method 1, purple dashed line) and  $2.1\text{ mT}$  (method 2, red dashed line) using for the further analysis. To be on the safe side, however, these  $B_{c1}(\text{T})$  values should be interpreted as fields for the first magnetic-flux entry, which could indeed be larger than the true  $B_{c1}$ . Together with  $B_{c1} = (\Phi_0/4\pi\lambda^2) \ln \frac{\lambda(0)}{\xi(0)}$  and  $B_{c2} = \Phi_0/4\pi\xi(0)^2$ , both the superconducting coherence length  $\xi(0)$  and the London penetration depth  $\lambda(0)$  can be estimated to  $\approx 9.6\text{ nm}$  and  $\geq 69\text{ nm}$  at zero temperature, respectively. The resulting Ginzburg-Landau parameter  $\kappa = \lambda(0)/\xi(0) \geq 7$ , indicates type-II superconductors behaviour of  $\text{Li}_{0.42}(\text{H}_2\text{O})_y\text{TaS}_2$ . As the given  $B_{c1}(0)$  and  $B_{c2}(0)$  stem from extrapolations over an

extended temperature region, the corresponding errors in these values and the quantities derived from them may be considerable, but they should reflect the correct orders of magnitude.

#### 4.3.4 Heat capacity

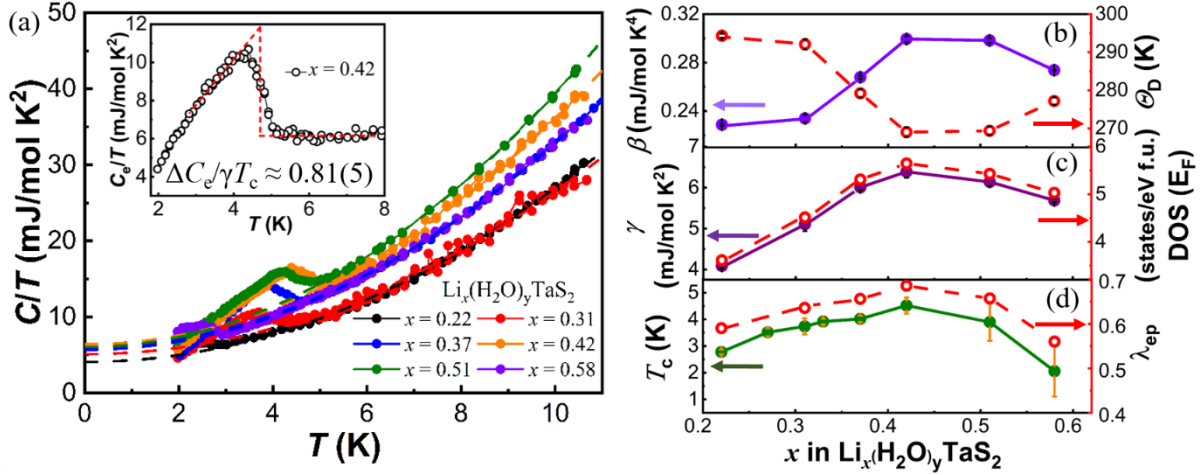


Fig. 4.5 (a) Reduced specific heat  $C/T$  vs.  $T$  curves of polycrystalline  $\text{Li}_x(\text{H}_2\text{O})_y\text{TaS}_2$  ( $x = 0.22, 0.31, 0.37, 0.42, 0.51, \text{ and } 0.58$ ) samples. The dashed lines represent fits to the data between the superconducting transition temperature and 10 K. The inset shows the electronic specific heat  $\Delta C_e/T$  at optimal intercalation with  $x = 0.42$ , together with an entropy-conserving construction to evaluate the discontinuity in  $C_e/T$ . The red dashed line is a fit to the superconducting part with a single gap BCS model. (b) Variation of  $\beta$  and corresponding  $\Theta_D$ , (c) normal state  $\gamma$  and corresponding DOS( $E_F$ ), and (d) the  $T_c$  determined from the discontinuity in the specific heat, together with the estimated  $\lambda_{ep}$ , all as functions of lithium content  $x$ .

The temperature dependence of the reduced specific heat  $C/T$  in zero magnetic field was measured in Fig. 4.5a from 1.9 to 10 K to further investigate the superconductivity in the hydrated  $\text{Li}_x(\text{H}_2\text{O})_y\text{TaS}_2$ . The  $T_c$  from an entropy-conserving construction with an idealized specific heat discontinuity is  $T_c \approx 4.6 - 4.7$  K as illustrated in the inset of Fig. 4.5a, which is consistent with the magnetic susceptibility and resistivity data for  $x = 0.42$  shown in Fig. 4.2d. The normal-state contribution can be fitted using the data between  $T_c$  and 10 K according to Eq. (3-3) in chapter 3.3.5. We obtained the parameters and summarized in Fig. 4.5b. The fitted  $\beta$  values at first increase and then decrease with increasing lithium content, resulting in a minimum of  $\Theta_D$  of  $\sim 269$  K, which is somewhat larger than in metal-intercalated  $2H\text{-TaS}_2$  and the parent  $2H\text{-TaS}_2$  ( $\Theta_D \approx 250$  K)[42, 122]. It has been reported that in the organic-matter intercalated  $2H\text{-TaS}_2$ , the  $\Theta_D$  values are also larger than in the parent  $2H\text{-TaS}_2$ . However, the reduction of  $\Theta_D$  by  $\sim 8.6\%$  upon lithium intercalation in hydrated  $\text{Li}_x(\text{H}_2\text{O})_y\text{TaS}_2$  samples may indicate a certain successive phonon softening associated with lithium doping (Fig. 4.5c). This is completely different from metal-intercalated  $2H\text{-TaS}_2$ , where the corresponding quantities

values hardly change with the intercalation[144]. By subtracting the phonon contribution from the total specific heats, the electronic parts of specific heat that characterize the superconducting state can be obtained, as it is shown for optimally hydrated  $\text{Li}_{0.42}(\text{H}_2\text{O})_y\text{TaS}_2$  with a maximum of  $\Delta C_e/\gamma T_c \approx 0.81(5)$  in the inset of Fig. 4.5a. This value is significantly lower than the expected standard BCS weak-coupling value of 1.43 and is similar to those reported for the parent  $2H\text{-TaS}_2$  and organic-matter intercalated  $2H\text{-TaS}_2$ . Therefore, superconductivity in the  $2H\text{-TaS}_2$  related compounds cannot be described by the BCS theory in its simplest form. The reduced discontinuity of the specific heat as compared to that of a single-band s-wave superconductor might indicate unconventional superconductivity with gap nodes [145], multiband features[146], or possible anisotropic single-gap superconductivity[147]. With the measured parameters  $\Theta_D$  and  $T_c$ , the parameter describing the electron-phonon coupling,  $\lambda_{\text{ep}} = \text{DOS}(E_F)V_{\text{e-ph}}$  (where  $V_{\text{e-ph}}$  denotes the electron-phonon-induced interaction), can be estimated from the inverted McMillan equation, assuming a repulsive screened-Coulomb parameter  $\mu^* \approx 0.13$ , which is a typical value for a metallic system[148],

$$\lambda_{\text{ep}} = \frac{1.04 + \mu^* \ln(\Theta_D/1.45T_c)}{(1 - 0.62\mu^*) \ln(\Theta_D/1.45T_c) - 1.04}. \quad (4-2)$$

As shown in Fig. 4.5d, the estimated  $\lambda_{\text{ep}} \approx 0.6\text{-}0.69$  are larger than those of parent  $2H\text{-TaS}_2$  ( $\sim 0.49$ ) but similar to those of the metal-intercalated  $2H\text{-TaS}_2$ , such as  $2H\text{-Li}_x\text{TaS}_2$  ( $\lambda_{\text{ep}} = 0.61$ )[122],  $2H\text{-Ni}_x\text{TaS}_2$  ( $\lambda_{\text{ep}} = 0.68$ )[42],  $2H\text{-Cu}_x\text{TaS}_2$  ( $\lambda_{\text{ep}} = 0.65$ )[67], and  $2H\text{-TaS}_{2-x}\text{Se}_x$  ( $\lambda_{\text{ep}} = 0.73$ )[66]. The enhancement of  $T_c$  is reminiscent to the effect of the oxygenation of ultrathin  $2H\text{-TaS}_2$ , which has been attributed to an increase in the  $\text{DOS}(E_F)$  by incorporation of oxygen into the  $\text{TaS}_2$  crystal lattice, resulting in a strongly increased electron-phonon coupling. It is worth noting that the  $T_c$  of  $\approx 4.6$  K (with an onset of diamagnetism up to  $\approx 5.0$  K) for hydrated  $\text{Li}_{0.42}(\text{H}_2\text{O})_y\text{TaS}_2$  is somewhat larger than the value reported for optimally metal-intercalated  $2H\text{-TaS}_2$  superconductors ( $T_c \sim 4.2$  K), indicating that the presence of interlayer water is favourable for superconductivity, which is similar to the role of other intercalated organic matter in  $2H\text{-TaS}_2$ [149]. Using the values of  $\lambda_{\text{ep}}$  and  $\gamma$  values in appropriate units, the  $\text{DOS}(E_F)$  can be estimated from the equation[150],

$$\text{DOS}(E_F) = \frac{3\gamma}{\pi^2 k_B^2 (1 + \lambda_{\text{ep}})}, \quad (4-3)$$

with the Boltzmann constant  $k_B$ . As shown in Fig. 4.5c, the calculated  $\text{DOS}(E_F)$  values initially exhibit an increasing trend and then slightly decrease with increasing  $x$ . The maximum of the  $\text{DOS}(E_F)$  value is  $5.6(5)$  states  $\text{eV}^{-1} \text{f.u.}^{-1}$  as the lithium content reaches  $x = 0.42$ , which is very

similar to the associated variation of  $T_c$  with  $x$ . It has been reported that the intercalation of organic matter has no obvious effects on the  $\text{DOS}(E_F)$  of the  $2H\text{-TaS}_2$  host, but mainly affect the interlayer spacing in the  $2H\text{-TaS}_2$  system[151]. As  $y \approx 0.86$  is constant for  $x \leq 0.42$  samples, the observed increase in the  $\text{DOS}(E_F)$  must therefore be due to the intercalation of lithium only. The reason for the subsequent slight decrease of the  $\text{DOS}(E_F)$  beyond  $x \approx 0.42$  is unclear, but it is conceivable that water intercalation and/or electron doping may further change the size or shape of the Fermi surface, as it has been found for the related  $2H\text{-Cu}_x\text{TaS}_2$ [67].

#### 4.3.5 Discussion

To gain some more insight into the enhanced superconductivity in  $\text{Li}_x(\text{H}_2\text{O})_y\text{TaS}_2$  based on the experimental results, I now focus on the  $T_c$  given by the BCS theory [9] in terms of the  $\text{DOS}(E_F)$ , the total electron-electron interaction  $V$ , and  $\Theta_D$ ,

$$T_c = 1.14\Theta_D \exp[-1/\text{DOS}(E_F)V]. \quad (4-4)$$

The  $T_c$  is proportional to  $\Theta_D$  and is a strongly varying function of the density of mobile charge carriers as the  $\text{DOS}(E_F)$  enters exponentially. Since the calculated  $\text{DOS}(E_F)$  values and  $T_c$  follow a similar trendline upon lithium intercalation  $x$ , it is tempting to make the variation of the  $\text{DOS}(E_F)$  solely responsible for the dome-like  $T_c$  dependence. However, the presence of the interlayered lithium atoms, together with the interlayer water, is also related to the variation of  $\Theta_D$  (Fig. 4.5b) and  $\lambda_{ep}$  (Fig. 4.5d), and hence, to the critical temperature  $T_c$  via the effect on the phonon spectrum and the electron-phonon coupling. It is very interesting to note that a strengthening of the electron-phonon coupling and a certain simultaneous phonon softening have been observed in other systems in the context of a dome-shaped  $T_c$  dependence[148, 152, 153].

Finally, the role of the interlayered water seems to be mainly to expand the interlayer spacing to  $\sim 0.58$  nm for hydrated  $\text{Li}_{0.42}(\text{H}_2\text{O})_y\text{TaS}_2$ , which is larger than that of parent  $2H\text{-TaS}_2$  ( $\sim 0.34$  nm). Although this enlarged interlayer spacing does not seem to strongly correlate with superconductivity in the hydrated  $\text{Li}_x(\text{H}_2\text{O})_y\text{TaS}_2$  system, the situation of interlayered species in  $2H\text{-TaS}_2$  can be complicated, and it is possible in principle that a weakened interlayer coupling and enhanced two-dimensionality can boost superconductivity as well.

## 4.4 Summary

Hydrated  $\text{Li}_x(\text{H}_2\text{O})_y\text{TaS}_2$  ( $0.22 \leq x \leq 0.58$ ;  $y \approx 0.86$ ) shows a dome-shape dependence of the critical temperature  $T_c$  on the lithium content  $x$  with a maximum  $T_c$  of at least 4.6 K for  $x \approx 0.42$ . This value is larger than in corresponding optimally intercalated  $2H\text{-TaS}_2$  without water or organic intercalants, supporting the scenario that a weakened interlayer coupling - as a result of a large interlayer spacing - may suppress the tendency of CDW formation and enhance superconductivity. The electron density of states at the Fermi level  $\text{DOS}(E_F)$  strongly varies with lithium content  $x$  and closely follows the corresponding variation of the critical temperature. While this may be the main factor influencing  $T_c$ , a simultaneous strengthening of the electron-phonon coupling and a phonon softening are observed upon approaching the maximum critical temperature, which has also been reported to occur in other systems in the context of a dome-shaped  $T_c$  dependence.

## 4.5 Related Publication

### *Superconductivity in hydrated $\text{Li}_x(\text{H}_2\text{O})_y\text{TaS}_2$*

Huanlong Liu, Shangxiong Huangfu, Hai Lin, Xiaofu Zhang and Andreas Schilling

J. Mater. Chem. C, 2023, 11, 3553-3561

<https://doi.org/10.1039/D2TC04353J>

## Chapter 5

# Signatures of a charge-density wave quantum-critical point in superconducting 2H-TaS<sub>2-x</sub> induced by disorder

As outlined in the previous chapters, 2H-TaS<sub>2</sub>, is an ideal correlated system for studying the interplay between superconductivity and the CDW state. In this chapter, I report on the tuning of the long-range CDW order and superconductivity in bulk 2H-TaS<sub>2-x</sub> by disorder, the level of which can be well controlled by the number of structural defects induced by sulfur (S) vacancies. Measurements of Raman, magnetization, electronic and thermal transport properties show that the long-range CDW is continuously suppressed, coexists with and is taken over by the emerging short-range CDW phase, eventually leading to strange-metal behaviour with linear resistivity at the endpoint of the long-range CDW. The superconductivity shows at first a two-step-like behaviour but reaches a maximum at the endpoint of long-range CDW with a single homogeneous phase, suggesting an interplay between superconductivity and CDW order. Moreover, our results suggest that the strange-metal behaviour, which is closely related to the short-range CDW, is a signature of quantum criticality with Planckian dissipation.

### 5.1 Introduction

The cuprate superconductors, for example hole-doped La<sub>2-x</sub>Sr<sub>x</sub>CuO<sub>4</sub>, La<sub>2-x</sub>Ba<sub>x</sub>CuO<sub>4</sub>, HgBa<sub>2</sub>CuO<sub>4+δ</sub> and YBa<sub>2</sub>Cu<sub>3</sub>O<sub>6+δ</sub>, exhibit a competition with the CDW order in the underdoped region[90, 154-157]. A fan-shaped region of strange-metal behaviour forms around the maximum of  $T_c$ , where the resistivity  $\rho$  shows a linear temperature dependence[158, 159]. A similar phenomenon has also been observed in iron-based[159, 160], nickelate[161, 162] superconductors, which could reflect a common mechanism of strange-metal behaviour in unconventional superconductors. Moreover, a positive relationship between the  $T_c$  and the coefficient of temperature-dependent linear resistivity  $A$ ,  $T_c \sim A^{0.5}$ , has been found recently, further suggesting that superconductivity could be closely linked to strange-metal behaviour[163-166].

In YBa<sub>2</sub>Cu<sub>3</sub>O<sub>6+δ</sub>, for example, the long-range CDW order disappears when  $T_c$  reaches a maximum value at the optimal doping level (Fig. 5.1b)[167]. The existence of short-range CDW order in the pseudogap state up to the optimal doping has recently been demonstrated experimentally and theoretically[168, 169]. In addition, short-range charge-density fluctuations

(CDFs) have been observed in the cuprates not only at low doping levels[157], but also in the strange-metal regime (reddish zone in Fig. 5.1b)[155, 170]. Because such short-range CDW correlations are accompanied by the occurrence of strange-metal behaviour, there may exist an intimate link between them[89, 171]. The CDW correlation length decreases to values close to those of the CDFs as the temperature is increased towards the CDW transition temperature ( $T_{CDW}$ ), suggesting that the CDFs have a common origin with the long-range CDW order and could represent a short-range CDW order. They may produce a strong isotropic scattering channel for the carriers at the Fermi level, leading to the strange-metal behaviour in the normal state[155].

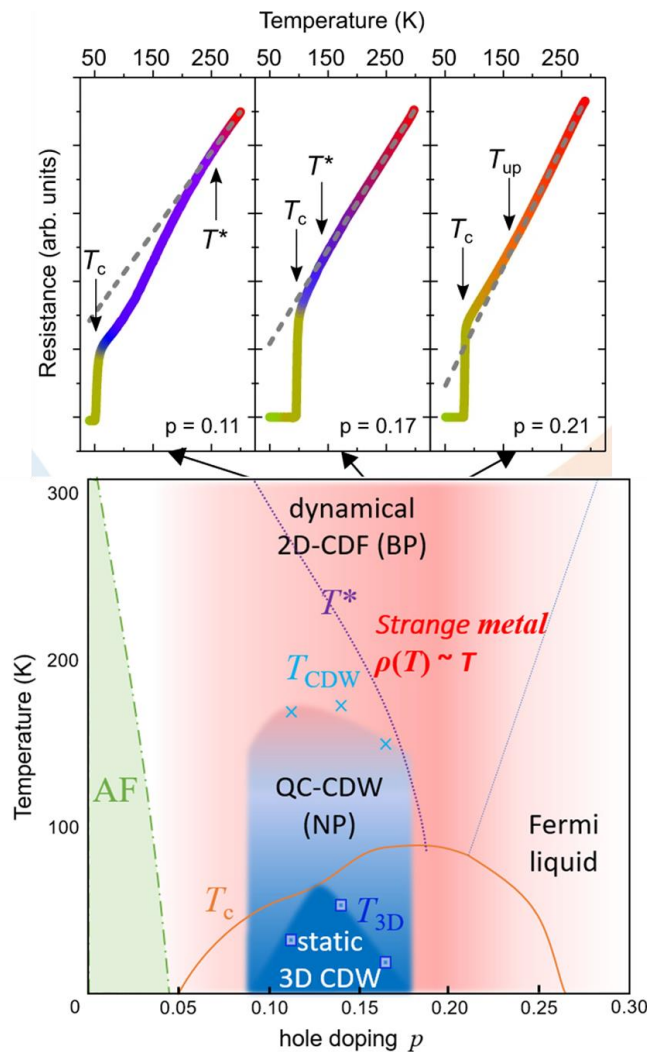


Fig. 5.1 (a) The temperature dependence of the resistance of YBa<sub>2</sub>Cu<sub>3</sub>O<sub>6+δ</sub>[155, 172]. The region of a linear temperature dependence is displayed as a red thick solid (b) the phase diagram ( $T$  vs. doping level  $p$ ) of YBa<sub>2</sub>Cu<sub>3</sub>O<sub>6+δ</sub>. The green zone is the antiferromagnetic phase. The reddish zone represents the 2D CDFs. In the cone above optimal doping (between  $T^*$  and the Fermi liquid), CDFs are responsible for the strange metal behavior and the linear in  $T$  resistivity. Light blue zone: "quasi-critical CDWs". These figures are taken from Refs.[89, 167].

As discussed earlier, the  $T_{\text{CDW}}$  in pristine  $2H\text{-TaS}_2$  is susceptible to the tuning of external parameters, in particular to the intercalation of foreign atoms but also to disorder and pressure[92, 122, 173, 174, 175, 176]. In pressurized  $2H\text{-TaS}_2$  the complete suppression of CDW at a critical pressure[68, 72] is accompanied by a non-Fermi-liquid behaviour in the low-temperature range due to the possible collapse of the long-range CDW along with enhanced critical CDFs. There, a minimum of the resistivity thermal exponent  $n$ , derived from the standard low-temperature resistivity relation  $\rho \propto T^n$ , has been observed as and in other CDW systems[108]. In this chapter, we are investigating a possible strange-metal behaviour in defect-controlled  $2H\text{-TaS}_{2-x}$ , and its relationship to CDFs and short-range CDW order.

## 5.2 Experiments

The  $\text{Li}_y\text{TaS}_2$  samples were synthesized by high temperature solid-state reaction, the details of which are described in chapter 3.2. Stoichiometric amounts of  $\text{Li}_2\text{S}$ , Ta and S powders were mixed, ground and pressed into a pellet. The pellets were sealed in evacuated quartz tubes and transferred into a muffle furnace. The tubes were annealed at 1073 K for 12 hours and then transferred into a glove box filled with argon. The samples were resealed into other quartz tubes, which were annealed again at 1073 K for one week. The prepared  $\text{Li}_y\text{TaS}_2$  samples were immersed in deionized water, then ultrasonicated and filtered several times with deionized water to remove the interlayer lithium atoms. The resulting lithium-free  $2H\text{-TaS}_{2-x}$  samples were dried in a vacuum drying oven at 30 °C and stored in the argon filled glove box.

Raman analyses were performed using a Horiba Labram HR Evolution spectrometer equipped with an Olympus microscope and an ultra-narrow notch filter with laser excitation at 532 nm. The samples were mounted in a He flow cryoVac micro Konti cryostat. The chemical compositions of  $2H\text{-TaS}_{2-x}$  were estimated by EDS measurements. The microstructure of the material was characterized by high resolution STEM images obtained on a Thermo Fisher Scientific Talos F200X TEM operated at 200 kV with EDS. High-resolution SRPES was performed to determine the chemical compositions and valence states at the synchrotron light facilities of the Swiss Light Source, Switzerland. The other experimental characterization steps were the same as those in chapter 3.2.

## 5.3 Characterization of the structure

The schematic synthesis process of  $2H\text{-TaS}_{2-x}$  from the intercalated  $\text{Li}_y\text{TaS}_2$  crystals is shown in Fig. 5.2a, which visualizes the formation of S vacancies induced by the removal of the



interlayered lithium. As an example sample, the structures of Li<sub>y</sub>TaS<sub>2</sub> ( $y = 0.51$ ) and the corresponding 2H-TaS<sub>2-x</sub> ( $x_c = 0.214$ ) have been characterized using the Raman spectra between 125 - 450 cm<sup>-1</sup> (Fig. 5.2b). The Raman peaks at ~400 cm<sup>-1</sup>, ~300 cm<sup>-1</sup> and ~203 cm<sup>-1</sup> correspond to the  $A_{1g}^1$ ,  $E_{2g}^1$ , and two-phonon modes, respectively[177], without any additional peaks, suggesting that both have a similar dynamics of the crystal lattice. The blue shift of the  $E_{2g}^1$  mode at  $x_c$  of 2H-TaS<sub>2-x</sub> is related to the weakened interlayer coupling induced by the removal of interlayer lithium[178].

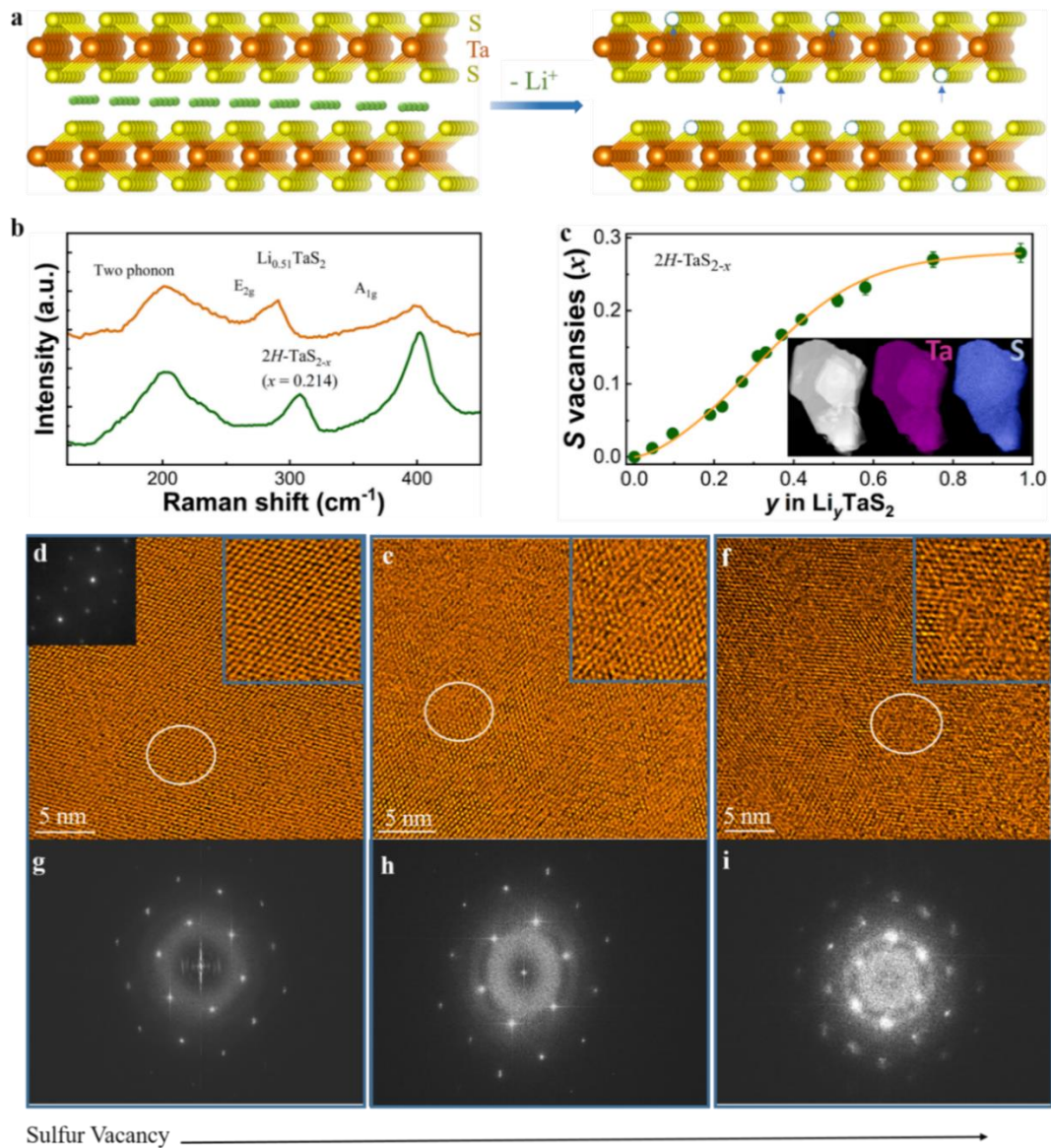


Fig. 5.2 (a) Schematic diagram of the 2H-TaS<sub>2-x</sub> samples synthesized by interlayer lithium extraction and S-vacancies generation (blue arrows). (b) Raman spectrum of intercalated Li<sub>0.52</sub>TaS<sub>2</sub> and a corresponding sample by removal of the interlayer lithium with  $x_c = 0.214$ . (c) The S-vacancy level as a function of the original interlayer lithium content in Li<sub>y</sub>TaS<sub>2</sub>. The inset shows the STEM images of  $x_c = 0.214$  with the corresponding Ta and S elemental maps. The HR-STEM images and corresponding FFT diffraction patterns of 2H-TaS<sub>2-x</sub> with (d, g)  $x = 0.032$ , (e, h)  $x = 0.143$ , and (f, i)  $x_c = 0.214$ .

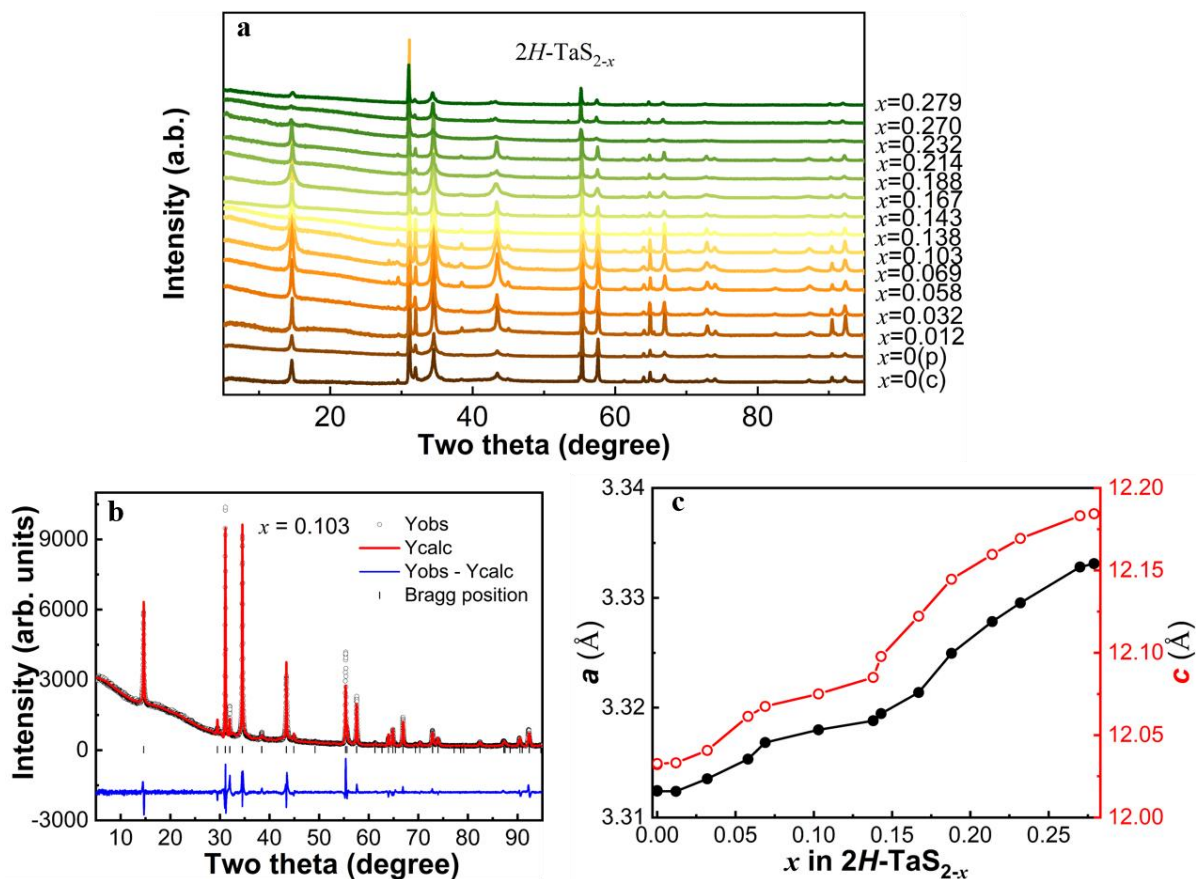


Fig. 5.3 (a) The PXR pattern at room temperature for all samples of  $2H\text{-TaS}_{2-x}$ . (b) The refined X-ray diffraction pattern of  $x = 0.103$ . The red dots are the observed data, while the black solid line represents the calculated intensities. The bottom blue solid line is the difference between the observed and calculated intensities. (c) The variation of the cell parameters  $a$  and  $c$  with  $x$  for  $2H\text{-TaS}_{2-x}$ .

The amount of S-vacancies in the  $2H\text{-TaS}_{2-x}$ , as a measure of structural disorder, has been identified by EDS, yielding the Ta/S ratio (Fig. 5.2c), whereas the lithium contents  $y$  of these  $\text{Li}_y\text{TaS}_2$  samples have been obtained by ICP-MS measurements[179]. The presence and uniform distribution of Ta and S elements were confirmed by STEM-EDS element mapping for  $x_c$  (inset of Fig. 5.2c). In Figs. 5.2d-f, the lattice structures of  $2H\text{-TaS}_{2-x}$  ( $x = 0.032, 0.143, 0.214$ ) are shown as obtained by high resolution STEM images. The corresponding selected-area electron diffraction (SAED) patterns with a series of bright spots reveal a hexagonal single crystal for  $x = 0.032$  in the left inset of Fig. 2d. One can see that the structure becomes increasingly disordered from  $x = 0.032$  to  $x_c$ . The corresponding magnified STEM images (circled areas in the insets of Figs. 5.2c-e) illustrate the crossover from point-like defects to disordered regions with increasing number of S - vacancies. The coexistence of ordered and disordered lattices were observed in Ta-S layers of a bulk single crystal with  $x = 0.143$ , indicating the coexistence of two types of regions with low and high S-vacancy contents. As

shown in Figs. 5.2g-i, the corresponding Fast-Fourier Transform (FFT) diffraction patterns ( $x = 0.032, 0.143, 0.214$ ) consist of hexagonal spots, which become blurrier, together with the appearance of diffuse rings induced by disordered regions, indicating an increase of the disorder level from S-vacancies in bulk 2H-TaS<sub>2-x</sub>.

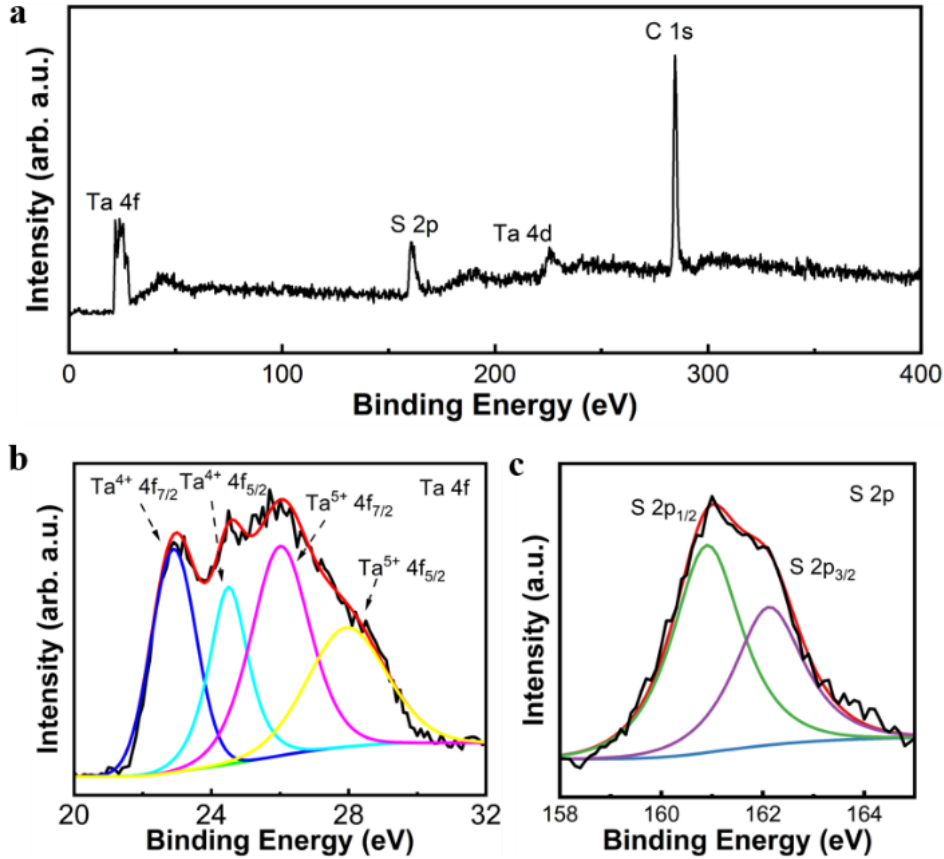


Fig. 5.4 (a) SRPES survey spectra. High-resolution SRPES spectra of the Ta 4f (b) and S 2p (c) peaks for  $x = 0.103$ .

To further confirm the crystal structure, all 2H-TaS<sub>2-x</sub> samples were characterized by PXRD at room temperature (Fig. 5.3a), confirming the similar crystal structure with a space group of  $P6_3/mmc$ . Due to the presence of disorder induced by the removed interlayer lithium, the diffraction peaks of the 2H-TaS<sub>2-x</sub> samples are weakened, especially at high levels of disorder. To more clearly reveal the structural differences of the 2H-TaS<sub>2-x</sub> samples, a detailed refinement was performed on all the PXRD patterns. As an example, the Rietveld refinement of the PXRD pattern of the hexagonal structure with  $x = 0.103$  is shown in Fig. 5.3b. The summarized structural parameters  $a$  and  $c$  are shown in Fig. 5.3c. A linear trend is observed, with a slight expansion of the Ta-S layer as the S-vacancy level increases, along with an increase of the interlayer spacing.

To confirm the chemical composition and valence states, a selected sample of  $x = 0.103$  was measured with SRPES. As shown in Fig. 5.4a, the SRPES survey spectrum indicates the presence of Ta and S elements, but no Li element. The high-resolution SRPES spectra of Ta 4f can be resolved into four peaks at  $\sim 22.9$  eV,  $\sim 24.5$  eV,  $\sim 26$  eV, and  $\sim 27.9$  eV (Fig. 5.4b). The two peaks at 22.9 eV and 24.5 eV can be assigned to Ta<sup>4+</sup> 4f<sub>7/2</sub> and Ta<sup>4+</sup> 4f<sub>5/2</sub>, respectively [180, 181]. The peaks at  $\sim 26$  eV and  $\sim 27.9$  eV agree well with the binding energy of Ta<sup>5+</sup> 4f, which could be attributed to the presence of Ta<sub>2</sub>O<sub>5</sub> species [182], which are common in bulk 2H-TaS<sub>2</sub> and other TMDs samples. The presence of metallic Ta in the 2H-TaS<sub>2-x</sub> samples has been excluded. In addition, there are no impurities in the XRD data and elemental mapping from the TEM measurements, further suggesting that the Ta<sub>2</sub>O<sub>5</sub> only originates from the surface of the bulk 2H-TaS<sub>2-x</sub>. This could be due to the sample being exposed to air for an extended time for the measurements, resulting in oxidation of the surface. The S 2p peak shows typical S<sup>2-</sup> species without other discernible species (Fig. 5.4c), suggesting the formation of the 2H phase TaS<sub>2</sub> [183].

## 5.4 Transport measurements

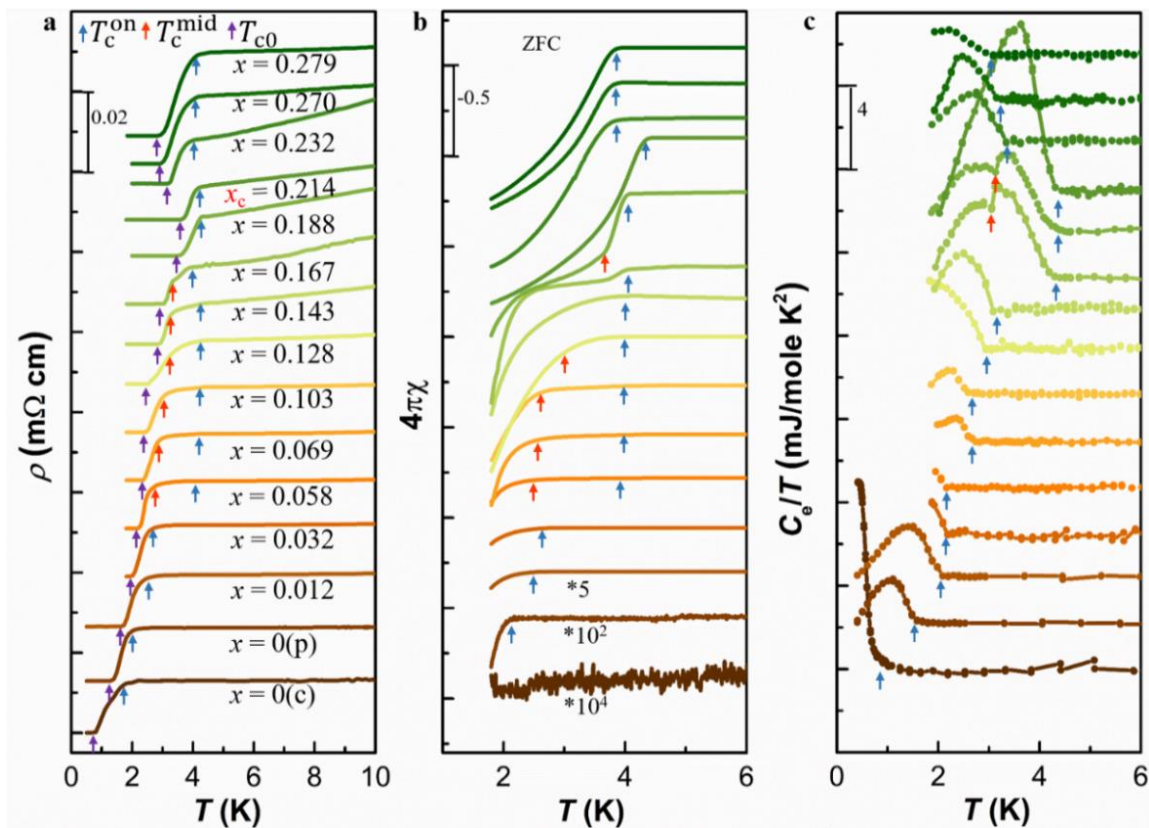


Fig. 5.5 (a) The temperature dependence of the resistivity, (b) the magnetization for both ZFC and FC in  $B = 2$  mT, and (c) the electronic specific-heat data for all 2H-TaS<sub>2-x</sub> samples.

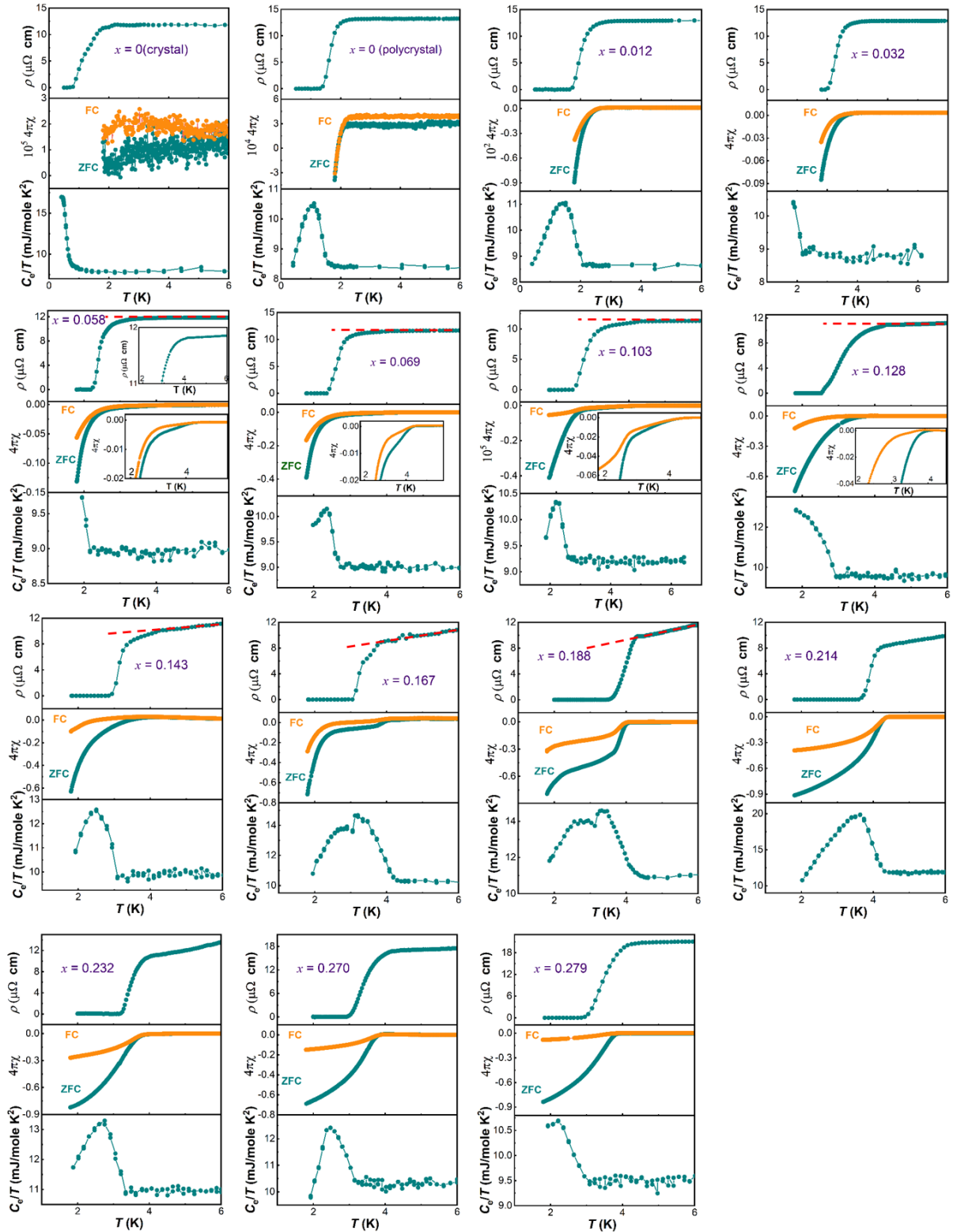


Fig. 5.6 The temperature dependence of the resistivity, the magnetization for both ZFC and FC in  $B = 2$  mT and the specific-heat curves in zero magnetic field to characterize the normal to superconducting phase transitions of all  $2H\text{-TaS}_{2-x}$  samples.

The normal-to-superconducting transition was characterized for all samples to investigate the effect of disorder on superconductivity in  $2H\text{-TaS}_{2-x}$  (Figs. 5.5 and 5.6). As shown in Fig. 5.5a, the temperature dependence of the resistivities  $\rho(T)$  show a sharp transition from normal to

superconducting states for less-disordered samples ( $0 \leq x \leq 0.032$ ). The onset of superconductivity ( $T_c^{on}$ ) of these samples is also evident in the magnetization data and has been confirmed by the discontinuity in the electronic specific heat ( $C_e/T$ ) at the transition to superconductivity. In contrast, as the disorder level increases above  $x = 0.058$ , the normal-to-superconducting transitions for the 2H-TaS<sub>2-x</sub> set in at  $T_c^{on} \sim 4.2$  K, and then show a kink instead of a sharp superconducting transition, forming a broad transition region to superconductivity with a two-step-like transition. Consistent with the  $\rho(T)$  dependence, a two-step transition of diamagnetism has also been observed as revealed by the ZFC data shown in Fig. 5.5b, indicating inhomogeneous superconductivity in with two superconducting coexisting phases[184, 185]. Furthermore, the evaluation of the magnetic susceptibility results reveal an increase in the fraction of the superconducting phase with the high  $T_c$  up to  $x = 0.188$ , and the  $\rho(T)$  shows a single sharp transition to zero-resistivity at  $T_{c0}$ . The presence of inhomogeneous superconductivity with coexisting phases for  $x \leq 0.188$  is further confirmed by the presence of two discontinuities in  $C_e/T$  (Fig. 5.5c)[186]. As the disorder level is further increased to a critical value with  $x_c$ , a single homogeneous superconducting phase forms again, and the critical temperature reaches a maximum of  $T_{c0} = 3.6$  K. Upon increasing the disorder level even further, superconductivity is continuously suppressed down to  $T_{c0} = 2.8$  K, resulting in a dome-like superconducting behaviour.

In Fig. 5.7, the systematically measured  $\rho(T)$  and  $\chi(T)$  show the evolution of the long-range CDW with disorder. This evolution can be accurately followed by determining the onset of  $T_{CDW}$  and evaluating a measure of the intensity of the CDW peak ( $A_{CDW}$ ) as illustrated for  $\rho(T)$  in Fig. 5.7a and the corresponding  $d\rho(T)/dT$  curves in Fig. 5.7c. The  $T_{CDW}$  are defined by the abrupt upturns of  $\rho(T)$  and the minima in the temperature derivative  $d\rho(T)/dT$  with decreasing temperature. As the disorder level increases,  $T_{CDW}$  turns out to be unchanged for  $x \leq 0.214$  and is close to its pristine value  $T_{CDW} \sim 75$  K (Fig. 5.6c). As an alternative to  $\rho(T)$ , the CDW phase transitions for 2H-TaS<sub>2-x</sub> can be determined from  $\chi(T)$  as shown in Fig. 5.7b and from the onset of the susceptibility drops  $\Delta\chi$ . Again, they remain almost unchanged at  $\sim 78$  K with increasing disorder level, which is consistent with the values obtained from  $d\rho(T)/dT$ . The intensity of the long-range CDW, however, is suppressed with increasing disorder level. This intensity can be defined as  $I_{CDW} = A_{CDW}(x)/A_{CDW}(0)$ , where  $A_{CDW}(x)$  is the area between each normalized  $d\rho(T)/dT$  curve and a baseline from 25 to  $\sim 75$  K, as shown in Fig. 5.7c[175, 187]. The  $I_{CDW}$  is gradually suppressed and eventually disappears at  $x_c = 0.214$ . As expected,

the  $\Delta\chi(x)/\Delta\chi(0)$  also displays a similar tendency for  $I_{\text{CDW}}(x)$  with varying disorder level as shown in the phase diagram in Fig. 5.11b.

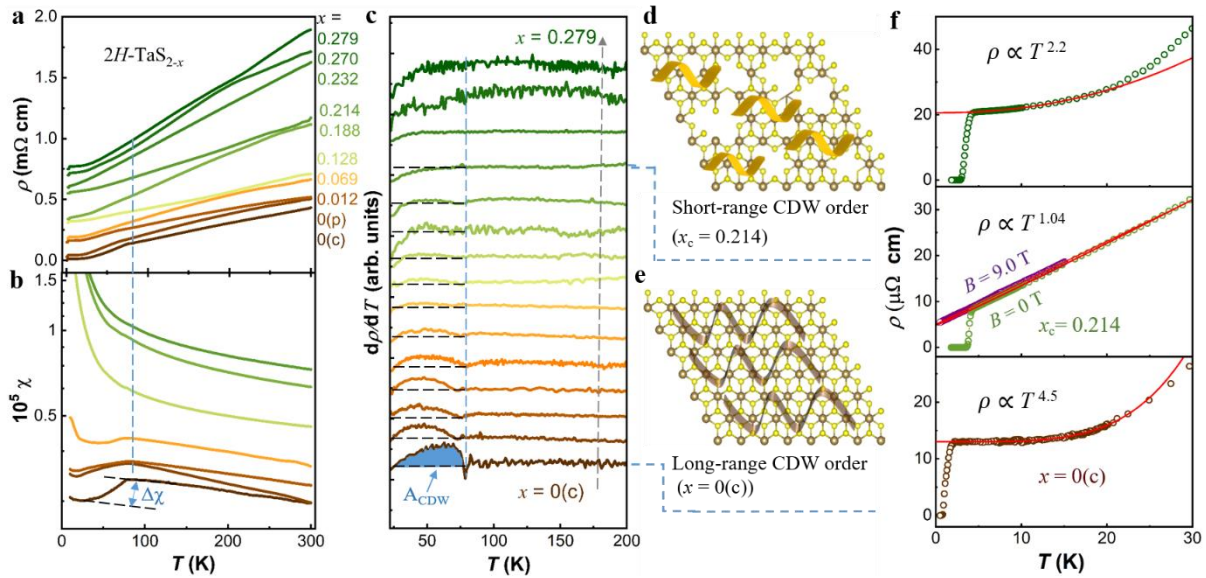


Fig. 5.7 (a) The temperature dependence of the resistivity  $\rho(T)$  and (b) the temperature dependence of the magnetic susceptibilities  $\chi(T)$  with an external magnetic field  $B = 0.5$  T. (c) The first derivative of the resistivity as a function of temperature,  $d\rho(T)/dT$ . Some curves have been offset for clarity. The dashed line around  $T = 78$  K indicates the  $T_{\text{CDW}}$  and illustrates the evaluation of the CDW intensity,  $A_{\text{CDW}}$ , with disorder ( $x$ ), where  $A_{\text{CDW}}(x)$  is the absolute peak area between 25 and 75K. (d) and (e) Illustrations of the dynamic evolution of the CDW state with  $x$ , in which the coloured waves represent the long-range CDW order (brown) for  $x = 0$  in (e) and the short-range CDW order (orange-brown) for  $x_c$  in (d) respectively. (f) Power law fits to  $\rho(T) = \rho_0 + AT^n$  in the range  $T_c^{\text{on}} \leq T \leq 20$  K to evaluate the exponents  $n$  for  $x = 0$ ,  $x_c = 0.214$ , and  $x = 0.279$ .

## 5.5 Raman measurements

The CDW signatures of selected samples ( $x = 0, 0.214, 0.270$ ) were also characterized using Raman spectroscopy with a cross-polarization configuration. As shown in the lower panel of Fig. 5.8a, the respective Raman spectra of  $x = 0$  at 5 K and 280 K show the common phonon modes at  $\sim 26$   $\text{cm}^{-1}$  ( $E_{2g}^2$ ),  $\sim 245$   $\text{cm}^{-1}$  ( $E_{2g}^1$ ), and  $\sim 404$   $\text{cm}^{-1}$  ( $A_{1g}^1$ ), defined in the point group  $D_{6h}$ . Two well-defined CDW amplitude modes are observed at  $\sim 48$   $\text{cm}^{-1}$  ( $E_{2g}$ -CDW) and  $\sim 78$   $\text{cm}^{-1}$  ( $A_{1g}$ -CDW). A two-phonon mode is located at  $\sim 190$   $\text{cm}^{-1}$ , resulting from phonon anomalies[72]. The corresponding temperature-dependent Raman scattering intensity maps for different disorder levels are shown in Figs. 5.8d-f. The Raman scattering spectra show CDW modes which become weaker and disappear with increasing temperature towards  $\sim 80$  K for  $x = 0$  (Fig. 5.8d). This indicates that the transition temperature of the long-range CDW is  $\sim 80$  K, similar to

the previous results. For  $x = 0$ , the CDW state is long-range order as sketched in the schematic Fig. 5.7e.

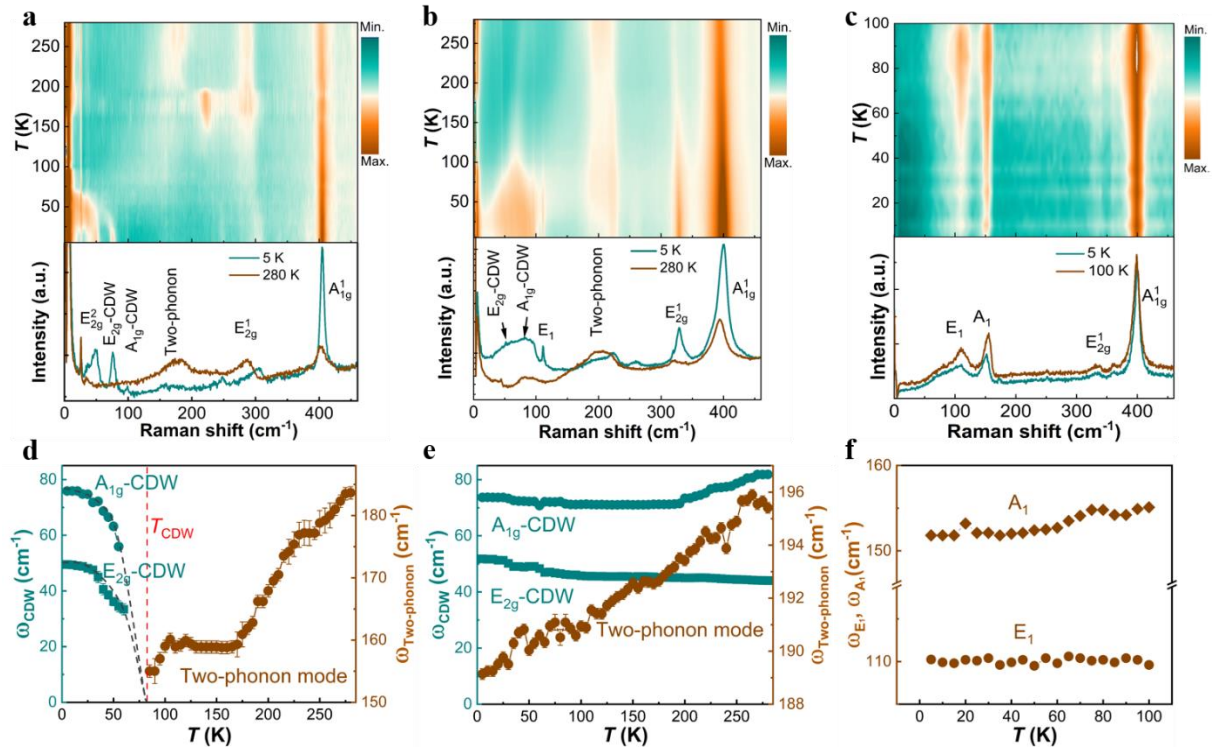


Fig. 5.8 Temperature maps of Raman scattering intensities and frequencies of CDW modes ( $A_{1g}$  and  $E_{2g}$ ), and two-phonon modes of  $x = 0$  (a and d),  $x_c = 0.214$  (b and e),  $x = 0.27$  (c and f) for  $2H\text{-TaS}_{2-x}$ . Spectra at 5 K and 280 K (100 K) of each sample are displayed for clarity.

Figure 5.8b shows the Raman spectra for  $x_c$  in the temperature range from 5 to 280 K. Surprisingly, the CDW amplitude modes exist in the entire temperature range, although their intensity changes with increasing temperature in Fig. 5.8e[85, 188-190]. The energies of these features are temperature dependent, suggesting that structural instabilities on short-length scales could exist at  $\sim 280$  K, which might be related to the CDW gap-closing temperature of  $\sim 240$  K as estimated from the angle-resolved photoemission spectroscopy data on  $2H\text{-TaS}_2$ [189]. These results demonstrate that short-range charge correlations persist above  $T_{\text{CDW}}$ , with the formation of short-range CDW order at  $x_c$ [191], as illustrated by the schematic Fig. 5.7d. As the disorder level is further increased to  $x = 0.27$ , the CDW mode becomes barely visible, while the two new Raman modes at  $\sim 110$   $\text{cm}^{-1}$  ( $E_1$ ) and  $\sim 152$   $\text{cm}^{-1}$  ( $A_1$ ) are observed (Figs. 5.8b and 5.8c) as compared to  $x = 0$ . This indicates that both  $E_1$  and  $A_1$  modes are characteristic for disordered samples and could be related to the S-vacancy induced disorder, symmetry breaking, and structural instabilities[192]. The  $E_1$  and  $A_1$  modes possess clear symmetry differences, yet emerge concomitantly with increasing disorder level, implying the existence of structural



instability even after the suppression of short-range CDW state in Fig. 5.8f[85, 189]. A possible CDW phase transition is not observed in the low-temperature  $\rho(T)$ ,  $\chi(T)$  and  $C_e/T$  data with temperatures, suggesting the complete disappearance of the CDW state below 5 K. To further confirm the variation of the CDW state, the Raman scattering spectra of the sample  $x = 0.167$  is shown in Fig. 5.9. The temperature dependence of the Raman spectra shows that the CDW amplitude modes still exist in the temperature range of 5- 300 K (Fig. 5.9a), indicating the formation of short-range CDW formation and similar to that of  $x_c$ . In Fig. 5.9b, the intensity of the quasi-elastic scattering starts to increase between 60-80 K, which could be due to the closing of the long-range CDW gap, indicating the coexistence of two types of CDW orders. All these results are consistent with the data shown in Fig. 5.10b. The decreasing intensity of the long-range CDW can be interpreted as a trend of the development of the short-range CDW with disorder. As mentioned above, the disorder-dependent evolution from long-range CDW to short-range CDW shows the coexistence of characteristic structures of these two different CDW phases below  $x_c$  ( $0 \leq x \leq 0.188$ ) for 2H-TaS<sub>2-x</sub>. Therefore, disorder can effectively tune the CDW state from long-range to short-range orders by perturbing the crystal structure.

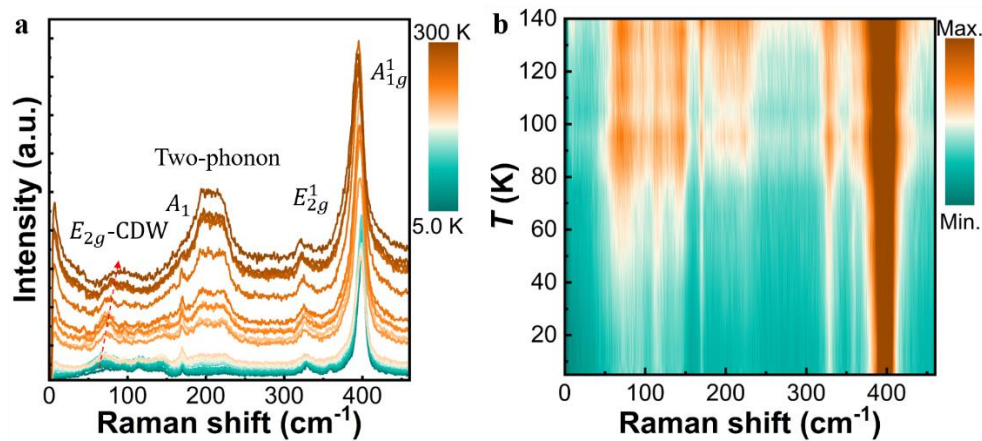


Fig. 5.9 (a) Temperature dependence of Raman scattering intensities and frequencies of CDW modes ( $E_{2g}$ , dashed red arrow) from 5 K to 300 K. (b) Temperature map of Raman scattering intensities and frequencies is shown in a temperature range of 5-140 K of  $x = 0.167$  for clarity.

## 5.6 Heat capacity

The CDW order competes with superconductivity at states near the Fermi surface[108]. The weakening of the long-range CDW is accompanied by a change of the contribution of the free electrons to physical properties that can be probed, for example, with specific heat  $C(T)$  and  $\chi(T)$  measurements. The low-temperature  $C(T)$  data for 2H-TaS<sub>2-x</sub> above the respective  $T_c$  were fitted according to Eq. (3-3) in chapter 3.3.5 (Figs. 5.10a and 5.10b). The extracted  $\beta$  shows no

significant change for 2H-TaS<sub>2-x</sub> (Fig. 5.10c), while  $\gamma$  first increases with increasing disorder to a maximum of  $12.1 \pm 0.2 \text{ mJ mol}^{-1} \text{ K}^{-2}$  at  $x_c$  and then decreases to  $9.5 \pm 0.2 \text{ mJ mol}^{-1} \text{ K}^{-2}$  at  $x = 0.279$  (Fig. 5.13b and Fig. 5.10d). In addition, the decrease in  $\chi(T)$  near  $T_{\text{CDW}}$  indicates a decrease in the Pauli spin susceptibility[193-195]. The susceptibility drops  $\Delta\chi \propto \Delta\text{DOS}(E_F)$  decrease with increasing disorder towards  $x_c$  (Figs. 5.7b and 5.13b), implying that fewer long-range CDW states are gapped below  $T_{\text{CDW}}$ . The normalized  $\Delta\chi$  and  $\gamma$  data show a complementary trend for  $x \leq x_c$ , both of which can be used for an experimental determination of the change in the density of the states  $\text{DOS}(E_F)$  (Fig. 5.10d)[108], indicating that a corresponding increase in the  $\text{DOS}(E_F)$  is mainly caused by the complete suppression of the long-range CDW. The  $\text{DOS}(E_F)$  values and  $T_c$ , therefore, follow a similar trendline upon the increase of disorder, demonstrating the significance of the variation in  $\text{DOS}(E_F)$  for the dome-like  $T_c$  dependence.

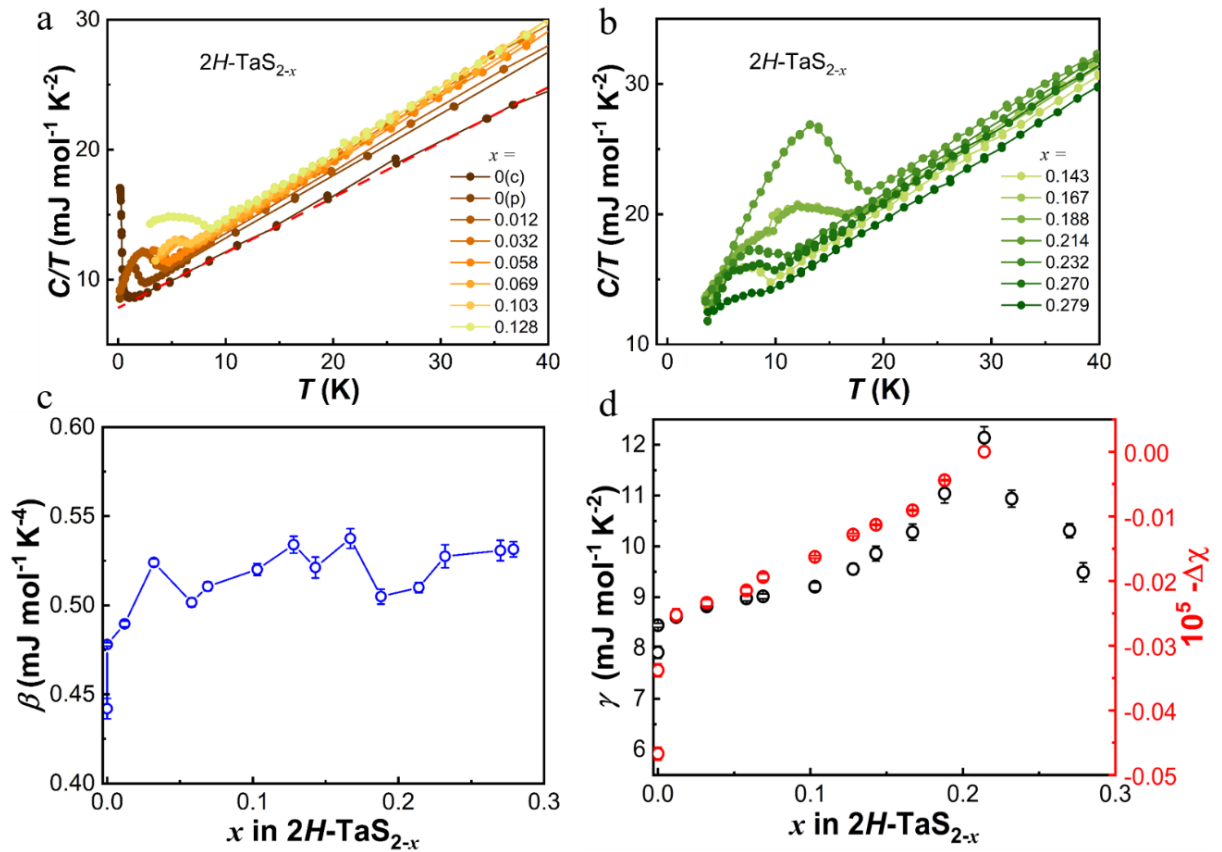


Figure 5.10 (a) and (b), The slope of the  $C/T$  versus  $T^2$ . Linear fits were used to obtain the coefficients  $\beta$  and plotted in (c) and the Sommerfeld constants  $\gamma$  displayed in (d). A dashed red line is shown as an example for  $x = 0$ . (d) The drops in susceptibility  $\Delta\chi$  at  $T_{\text{CDW}}$  as evaluated from the susceptibility data above and below  $T_{\text{CDW}}$ .

## 5.7 Electronic phase diagram

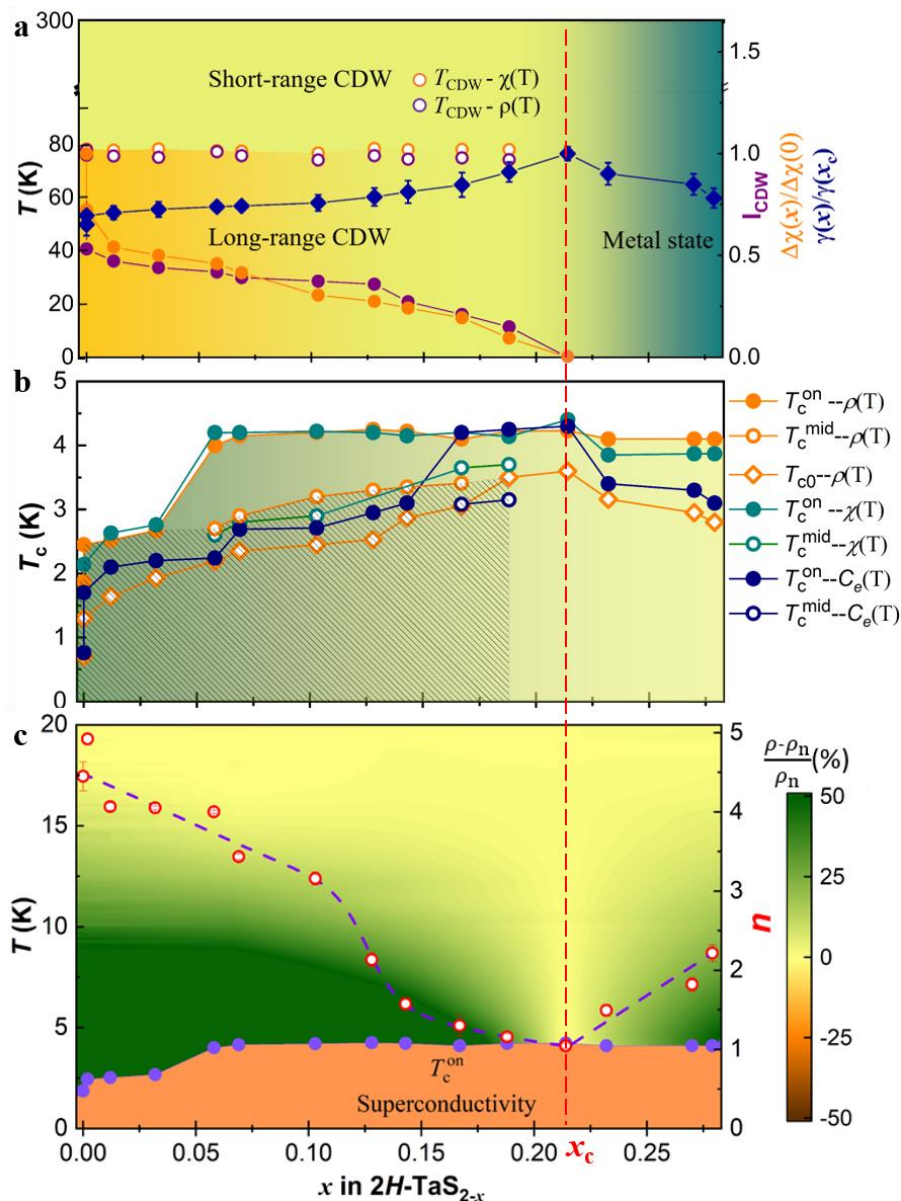


Fig. 5.11 (a) The variation of CDW state with disorder in 2H-TaS<sub>2-x</sub>. The  $T_{CDW}$  determined by  $\rho(T)$  and  $\chi(T)$  are plotted as functions of the disorder level. Both the  $I_{CDW}$  and  $\Delta\chi(x)/\Delta\chi(0)$  (right scale) show a similar trend with disorder. The dome-shaped variation of the normalized Sommerfeld coefficient  $\gamma(x)/\gamma(x_c)$  with increasing disorder shows a pronounced peak at  $x_c = 0.214$ . (b)  $T_c$ - $x$  phase diagram of 2H-TaS<sub>2-x</sub>. The shadowed region shows the disorder-dependent  $T_c^{mid}$ , while  $T_{c0}$  exhibits a dome-like variation with a sharp peak at  $x_c$ . (c) Temperature-disorder phase diagram based on the resistivity measurements for 2H-TaS<sub>2-x</sub>. The colours represent the fractional deviations  $(\rho - \rho_n)/\rho_n$  (%) from fits to a linear temperature dependence  $\rho_n = \rho'_0 + A'T$  below 20 K, while the red circles are the exponents from corresponding fits to  $\rho(T) = \rho_0 + AT^n$ .

To establish the relationship between disorder, CDW order, and superconductivity, all results are summarized in the electronic phase diagrams present in Figs. 5.11a-b. The disorder

dependence of  $T_c$  in the range between  $0.058 \leq x \leq 0.214$  shows that the onset of the normal-to-superconducting transitions takes place already at  $T_c^{on}$  with the same value of about 4.2 K, independent of  $x$ , whereas the long-range CDW order is gradually weakened, and as a result, the short-range CDW order probably takes over. Meanwhile, along with this trend, the superconducting magnetic shielding of the component with the higher  $T_c$  increases continuously, and the system finally reaches a state with homogeneous superconductivity at  $x \geq 0.214$  (Figs. 5.5b and 5.6). This may imply that the superconductivity at  $T_c \approx 4.2$  K originates from the short-range CDW regions induced by structural disorder, and the closing of the long-range CDW gap leads to an increase of  $\text{DOS}(E_F)$ , giving rise to the higher  $T_c$ . It is comparable to the optimum value of  $T_c$  in other 2H-TaS<sub>2</sub> systems when the long-range CDW is completely suppressed[62]. Above  $x_c$ , the superconducting pairing strength must be weakened with increasing disorder scattering, resulting in a slight decrease in  $T_c$ . In the range of the two-step-like superconducting transition, the  $T_c^{\text{mid}}$  increases monotonically and reaches a maximum of  $\sim 3.4$  K at  $x = 0.167$  with increasing disorder level, which is almost identical to the  $T_c \approx 3.6$  K observed in disorder-induced charge-doped Ta<sub>1-x</sub>S<sub>2</sub> monolayers[104]. Furthermore, a systematic suppression of  $T_{\text{CDW}}$  was not observed with increasing disorder level, suggesting that the enhancement of  $T_c^{\text{mid}}$  could be attributed to the increase in carrier density induced by S-vacancies and point-like defects for disordered 2H-TaS<sub>2-x</sub> ( $0 \leq x \leq 0.188$ ), as marked by the shadowed region in Fig. 5.10a. The unusual two-step superconducting transition is observed in the intermediate disorder range with the coexistence of the long-range and short-range CDWs in Fig. 5.11c, suggesting a unique interplay between superconductivity and the CDW state. This is also similar to the pressure effect on CsV<sub>3</sub>Sb<sub>5</sub>, in which a two-step-like superconductivity transition has been observed in the regions with coexistence of two types of CDW[61, 109, 196].

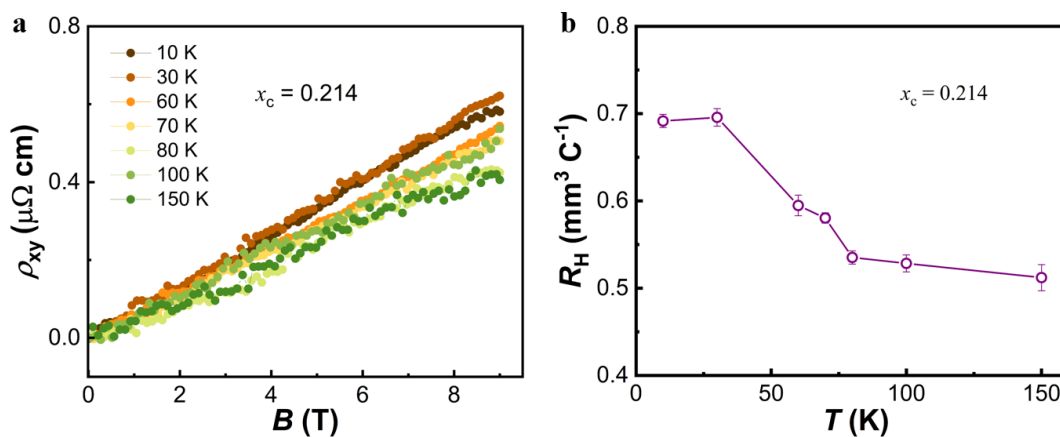


Fig. 5.12 (a) The magnetic field dependence of the Hall resistivity at different temperatures. (b) The estimated temperature dependence of the Hall coefficients for  $x_c=0.214$ .

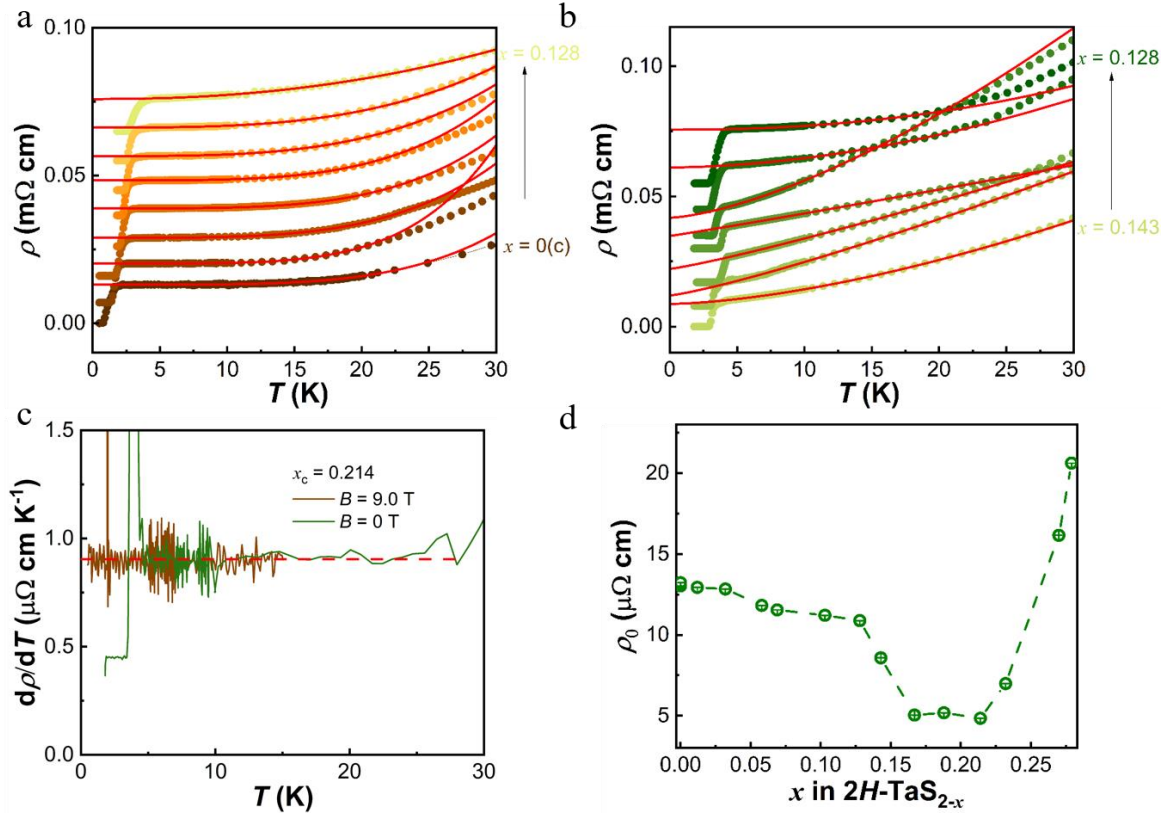


Figure 5.13 (a) and (b) The plots show the resistivity  $\rho(T)$  in zero magnetic field. Some curves have been offset for clarity. The red lines represent fits to the power law  $\rho(T) = \rho_0 + AT^n$  between  $T_c^{on}$  and 20 K. The fitting procedures have been considered acceptable only when the  $R$ -Square value was larger than 0.99. (c) The temperature derivative of the resistivity for  $x_c = 0.214$  measured in magnetic fields of 0 T (green) and 9.0 T (wine), showing the expected linear behaviour. (d) Resulting residual resistivity  $\rho_0$ .

Quantum-critical behaviour can emerge when the CDW order is completely suppressed[197]. Considering the continuous weakening of the long-range CDW in 2H-TaS<sub>2-x</sub>, the results of an analysis of all the low-temperature  $\rho(T)$  data between  $T_c^{on}$  and 20 K to search for indications for quantum criticality are shown in Fig. 5.11c. The colour scheme represents the fractional deviation  $\frac{\rho - \rho_n}{\rho_n}$  (%) of  $\rho(T)$  from fits to a linear temperature dependence  $\rho_n = \rho'_0 + A'T$ . The yellow region, indicating a linear  $\rho(T)$ , extends down to the top of the  $T_c(x)$  dome at  $x_c$ , which is also supported by an alternative analysis based on the temperature derivative  $d\rho/dT$  shown in Fig. 5.13c. At this disorder level, the significant enhancement of  $T_c = 4.2$  K coincides with pronounced strange-metal behaviour, which is accompanied by a complete suppression of the long-range CDW. Here, the temperature range for linear behaviour is widest with only  $\sim 4\%$  deviation from strict linearity. For a further analysis, the low-temperature  $\rho(T)$  can be approximated by a power law  $\rho(T) = \rho_0 + AT^n$  between  $T_c^{on}$  and 20 K (Figs. 5.13a and 5.13b), where  $\rho_0$  represents the residual resistivity at  $T=0$ . The systematic evolution of the

low-temperature  $\rho(T)$  data ranges from normal electron-phonon scattering behaviour ( $n = 4.5$ ) to non-Fermi liquid-like at  $x_c$  ( $n = 1.04$ ) and finally to Fermi liquid-like ( $n = 2.2$ ), which is a typical signature of quantum criticality at  $x_c$  (Fig. 5.11c). Upon application of a magnetic field of  $B = 9.0$  T to the sample with  $x_c$ , the linear range of  $\rho(T)$  even further extends down to 500 mK (Figs 5.13c and 5.7f).

Most interestingly, the disorder dependence of  $\rho_0$  shows, contrary to intuition, a decreasing trend with increasing disorder, reaching a minimum around  $x_c$ , before increasing again with additional disorder (Fig. 5.13d). This is similar to the results reported for pressurized 2H-TaS<sub>2</sub> and CsV<sub>3</sub>Sb<sub>5</sub>[61, 68], and may be related to the enhancement of  $\text{DOS}(E_F)$  upon approaching  $x_c$ . A universal linear temperature dependence close to a quantum-critical point has recently been attributed to charge-carrier scattering at a rate given by  $\hbar/\tau = \alpha k_B T$ , where  $\hbar$  is the reduced Planck constant and  $k_B$  is the Boltzmann constant, and  $\alpha \approx 1$  regardless of the nature of the scattering process. To examine this hypothesis, we combine the estimated effective mass  $m^* \approx 18 m_e$  from the heat-capacity measurements  $\gamma = (2N_A k_B^2 / \pi \hbar^2) a^2 m^*$ , charge carrier density  $n$  from  $R_H$  in Fig. 5.12 with the linear coefficient  $A \approx 8.8 \times 10^{-9}$  ( $\Omega \text{ m K}^{-1}$ ), and can estimate  $\alpha$  from the below equation[158, 160],

$$\alpha = A \frac{\hbar e^2 n}{k_B m^*}. \quad (5-1)$$

The value  $\alpha = 0.92 \pm 0.1$  at  $x_c$ , indicates that the linear resistivity indeed agrees with Planckian dissipation. This finding strongly supports the hypothesis that the charge-carrier scattering rate close to a quantum-critical point is universal, which has been verified for many other systems such as the cuprate, heavy-Fermion, organic, and iron-based superconductors that are all seemingly unrelated to TMDs[198].

The order parameter in play, in the absence of any magnetic ordering and thereby excluding spin fluctuations[199], is most likely the charge order, the critical fluctuations of which at its vanishing lead to the appearance to a quantum critical point (QCP) at  $x_c$ . We note here that for the single crystalline 2H-TaS<sub>2</sub> in the dirty limit[68], there is no clear CDW phase transition in  $\rho(T)$ . There, the low-temperature  $\rho(T)$  shows a Fermi-liquid behaviour under pressure with an enhancement of superconductivity, which is also observed in the isoelectronic substitution in disordered 2H-TaSe<sub>2-x</sub>S<sub>x</sub>[144]. In the clean limit of 2H-TaS<sub>2</sub>, however, it is a non-Fermi liquid behaviour that appears concomitantly with the pressure-induced collapse of CDW at a possibly pressure-induced QCP. The Fermi-liquid behaviour recovers upon further increasing

the external pressure[68], in a similar way to this experiments, where disorder serves as an external control parameter.

## 5.8 Summary

In summary, all results of the disorder-induced variation of the CDW order in  $2H-TaS_{2-x}$  show that the long-range CDW is continuously weakened but is independent of the transition temperature. This is at first accompanied by a two-step-like superconducting transition, which could be ascribed to the formation of a short-range CDW when disorder determines the long-range CDW order in  $2H-TaS_{2-x}$ . At the endpoint of the long-range CDW for  $x_c = 0.214$ , the superconductivity reaches a maximum of  $T_{c0} = 3.6$  K, accompanied by the development of a strange-metal behaviour at a QCP which is most likely a result of critical charge-density fluctuations. At  $x_c$ , the resistivity becomes linear in temperature and follows quantitatively the scenario of Planckian dissipation. All these results on disordered  $2H-TaS_{2-x}$  significantly contribute to the understanding of quantum critical behaviour in superconductors.

## 5.9 Related Publication

*Signatures of a charge-density wave quantum-critical point in superconducting  $2H-TaS_{2-x}$  induced by disorder*

Huanlong Liu, Shangxiong Huangfu, Xiaofu Zhang, Qisi Wang, Dirk Wulferding, Fabian O. von Rohr, Andreas Schilling

*Submitted*

## Chapter 6

### Conclusion

In the present thesis, the interplay between the CDW state and superconductivity in the  $2H$ - $\text{TaS}_2$  system has been systematically investigated by introducing external atoms and disorder.

We have presented how superconductivity and the CDW state evolve in the  $2H$ - $\text{Li}_x\text{TaS}_2$  as a function of lithium-intercalation. The CDW transition temperature is effectively suppressed by lithium intercalation, while the  $T_c$  is concurrently increased, reaching a maximum of  $T_c = 3.5$  K at  $x = 0.096$ , which supports a competitive relationship between the long-range CDW state and superconductivity. A difference in Hall resistivity was observed between pristine  $2H$ - $\text{TaS}_2$  and  $2H$ - $\text{Li}_x\text{TaS}_2$ , which may originate from the reconstruction of the Fermi surface by lithium-intercalation induced suppression of the long-range CDW order, indicating that the prominently improved  $T_c$  in  $2H$ - $\text{Li}_x\text{TaS}_2$  results from the increase of the electron density of states at the Fermi level ( $\text{DOS}(E_F)$ ) induced by suppression of the long-range CDW state rather than charges injection by lithium intercalation. The investigation of superconductivity was extended to  $\text{Li}_x(\text{H}_2\text{O})_y\text{TaS}_2$  with a constant interlayer water content estimated within the range of the lithium content, where the CDW order is absent. The superconductivity, dependent on lithium content  $x$ , displayed a dome-like shape with a maximum  $T_c$  of 4.6 K at  $x = 0.42$ , which is along with the variation of the  $\text{DOS}(E_F)$ . Moreover, this optimal  $T_c$  value surpassed that of the corresponding optimally intercalated  $2H$ - $\text{TaS}_2$  without water or organic intercalants, further emphasizing the role of the electron-phonon coupling enhancement and phonon softening in boosting superconductivity. All results indicate that intercalation is an excellent strategy for the investigation of the competition and coexistence of superconductivity and the long-range CDW order, and for understanding superconductivity within the BCS theoretical framework.

Based on the as-prepared lithium-intercalated  $2H$ - $\text{TaS}_2$  samples, we successfully synthesized the S vacancies-induced disordered bulk  $2H$ - $\text{TaS}_{2-x}$  by removing the interlayer lithium atoms and investigated their physical properties in detail. The disorder-induced variations of the CDW order revealed a continuous weakening of the long-range CDW, independent of the transition temperature, and the emergence of the short-range CDW. The two coexisting CDW orders with different disorder levels lead to a two-step-like superconducting transition and homogeneous superconductivity at the endpoint of the long-range CDW accompanied by the formation of the short-range CDW. We have investigated the role of the short-range CDW by analyzing the



normal resistivity. The evolution of the low-temperature form of the resistivity with the disorder level is from electron-phonon scattering behaviour to non-Fermi liquid at  $x_c$  and back to Fermi-liquid-like, which are classic signatures of quantum criticality and consistent with the Planckian dissipation scenario in disordered  $2H\text{-TaS}_{2-x}$ . The complete suppression of the long-range CDW, together with the minimum of the thermal exponent  $\alpha \approx 1$  and the enhancement of the DOS( $E_F$ ), is accompanied by the formation of the short-range CDW, suggesting that the critical charge-density fluctuations play an important role in the enhancement of  $T_c$  at the CDW quantum critical point and revealing potential physics between the CDW state, strange-metal behaviour, and superconductivity.

In the studies illustrated in this thesis, we have systematically investigated the interplay between superconductivity and the CDW state using different strategies, of which show intriguing and unexpected physical properties and may be extended to other TMDs system. Our work represents a major step forward in the interpretation of the interplay between the CDW and superconductivity, and may even have some relevance to the understanding of high-temperature superconductivity. This contributes to the understanding of high-temperature superconductivity and even further to the discovery of superconductors with higher  $T_c$  and improved physical properties for applications.

## Bibliography

- [1] P.W. Anderson, More Is Different, *Science*, 177 (1972) 393-396.
- [2] G. Baym, C. Pethick, *Landau Fermi-liquid theory: concepts and applications*, (2008).
- [3] G. Grüner, The dynamics of charge-density waves, *Reviews of modern physics*, 60 (1988) 1129.
- [4] Z. Xu, H. Yang, X. Song, Y. Chen, H. Yang, M. Liu, Z. Huang, Q. Zhang, J. Sun, L. Liu, Topical review: recent progress of charge density waves in 2D transition metal dichalcogenide-based heterojunctions and their applications, *Nanotechnology*, 32 (2021) 492001.
- [5] J.R. Schrieffer, *Theory of superconductivity*, CRC press, 2018.
- [6] J. Bardeen, L.N. Cooper, J.R. Schrieffer, *Microscopic Theory of Superconductivity*, *Physical Review*, 106 (1957) 162-164.
- [7] H.K. Onnes, Further experiments with liquid helium. C. On the change of electric resistance of pure metals at very low temperatures etc. IV. The resistance of pure mercury at helium temperatures, in: *Through Measurement to Knowledge: The Selected Papers of Heike Kamerlingh Onnes 1853–1926*, Springer, 1991, pp. 261-263.
- [8] D. van Delft, P. Kes, The discovery of superconductivity, *Physics Today*, 63 (2010) 38-43.
- [9] J. Bardeen, L.N. Cooper, J.R. Schrieffer, *Theory of Superconductivity*, *Physical Review*, 108 (1957) 1175-1204.
- [10] W. McMillan, Transition temperature of strong-coupled superconductors, *Physical Review*, 167 (1968) 331.
- [11] J.G. Bednorz, K.A. Müller, Possible high  $T_c$  superconductivity in the Ba–La–Cu–O system, *Zeitschrift für Physik B Condensed Matter*, 64 (1986) 189-193.
- [12] W.E. Pickett, Electronic structure of the high-temperature oxide superconductors, *Reviews of Modern Physics*, 61 (1989) 433-512.
- [13] M.K. Wu, J.R. Ashburn, C.J. Torng, P.H. Hor, R.L. Meng, L. Gao, Z.J. Huang, Y.Q. Wang, C.W. Chu, Superconductivity at 93 K in a new mixed-phase Yb-Ba-Cu-O compound system at ambient pressure, *Phys Rev Lett*, 58 (1987) 908-910.
- [14] A. Schilling, M. Cantoni, J.D. Guo, H.R. Ott, Superconductivity above 130 K in the Hg–Ba–Ca–Cu–O system, *Nature*, 363 (1993) 56-58.
- [15] Y. Kamihara, T. Watanabe, M. Hirano, H. Hosono, Iron-Based Layered Superconductor  $\text{La}[\text{O}_{1-x}\text{F}_x]\text{FeAs}$  ( $x = 0.05\text{--}0.12$ ) with  $T_c = 26$  K, *Journal of the American Chemical Society*, 130 (2008) 3296-3297.

- [16] T.Y. Chen, Z. Tesanovic, R.H. Liu, X.H. Chen, C.L. Chien, A BCS-like gap in the superconductor  $\text{SmFeAsO}_{0.85}\text{F}_{0.15}$ , *Nature*, 453 (2008) 1224-1227.
- [17] X.H. Chen, T. Wu, G. Wu, R.H. Liu, H. Chen, D.F. Fang, Superconductivity at 43 K in  $\text{SmFeAsO}_{1-x}\text{F}_x$ , *Nature*, 453 (2008) 761-762.
- [18] D. Li, K. Lee, B.Y. Wang, M. Osada, S. Crossley, H.R. Lee, Y. Cui, Y. Hikita, H.Y. Hwang, Superconductivity in an infinite-layer nickelate, *Nature*, 572 (2019) 624-627.
- [19] H. Sun, M. Huo, X. Hu, J. Li, Z. Liu, Y. Han, L. Tang, Z. Mao, P. Yang, B. Wang, J. Cheng, D.X. Yao, G.M. Zhang, M. Wang, Signatures of superconductivity near 80 K in a nickelate under high pressure, *Nature*, (2023).
- [20] W. Meissner, R. Ochsenfeld, Ein neuer effekt bei eintritt der supraleitfähigkeit, *Naturwissenschaften*, 21 (1933) 787-788.
- [21] F. London, H. London, The Electromagnetic Equations of the Supraconductor, *Proc. R. Soc. Lond. A*, 149 (1935) 71-88.
- [22] V.L. Ginzburg, L.D. Landau, On the Theory of superconductivity, *Zh.Eksp.Teor.Fiz.*, 20 (1950) 1064-1082.
- [23] M. Schluter, M. Lannoo, M. Needels, G.A. Baraff, D. Tománek, Electron-phonon coupling and superconductivity in alkali-intercalated  $\text{C}_{60}$  solid, *Physical Review Letters*, 68 (1992) 526-529.
- [24] D.-V. Anghel, G.A. Nemnes, The role of the chemical potential in the BCS theory, *Physica A: Statistical Mechanics and its Applications*, 464 (2016) 74-82.
- [25] M. Keller, W. Metzner, U. Schollwöck, Dynamical Mean-Field Theory for Pairing and Spin Gap in the Attractive Hubbard Model, *Physical Review Letters*, 86 (2001) 4612-4615.
- [26] G. Gruner, *Density Waves In Solids*, CRC Press, 2018.
- [27] T.M. Rice, G.K. Scott, New mechanism for a charge-density-wave instability, *Physical Review Letters*, 35 (1975) 120.
- [28] R. Peierls, *More surprises in theoretical physics*, Princeton University Press, 1991.
- [29] E. Slot, M.A. Holst, H.S.J. van der Zant, S.V. Zaitsev-Zotov, One-Dimensional Conduction in Charge-Density-Wave Nanowires, *Physical Review Letters*, 93 (2004) 176602.
- [30] P.A. Lee, T.M. Rice, P.W. Anderson, Fluctuation Effects at a Peierls Transition, *Physical Review Letters*, 31 (1973) 462-465.
- [31] L.N. Bulaevskiĭ, Peierls structure transition in quasi-one-dimensional crystals, *Soviet Physics Uspekhi*, 18 (1975) 131.

- [32] M. Hoesch, A. Bosak, D. Chernyshov, H. Berger, M. Krisch, Giant Kohn Anomaly and the Phase Transition in Charge Density Wave  $\text{ZrTe}_3$ , *Physical Review Letters*, 102 (2009) 086402.
- [33] X. Zhu, J. Guo, J. Zhang, E.W. Plummer, Misconceptions associated with the origin of charge density waves, *Advances in Physics: X*, 2 (2017) 622-640.
- [34] J. van Wezel, P. Nahai-Williamson, S.S. Saxena, Exciton-phonon-driven charge density wave in  $\text{TiSe}_2$ , *Physical Review B*, 81 (2010) 165109.
- [35] A. Wegner, J. Zhao, J. Li, J. Yang, A.A. Anikin, G. Karapetrov, K. Esfarjani, D. Louca, U. Chatterjee, Evidence for pseudo--Jahn-Teller distortions in the charge density wave phase of 1T- $\text{TiSe}_2$ , *Physical Review B*, 101 (2020) 195145.
- [36] G. Li, W.Z. Hu, D. Qian, D. Hsieh, M.Z. Hasan, E. Morosan, R.J. Cava, N.L. Wang, Semimetal-to-Semimetal Charge Density Wave Transition in 1T- $\text{TiSe}_2$ , *Physical Review Letters*, 99 (2007) 027404.
- [37] G. Duvjir, B.K. Choi, I. Jang, S. Ulstrup, S. Kang, T. Thi Ly, S. Kim, Y.H. Choi, C. Jozwiak, A. Bostwick, E. Rotenberg, J.-G. Park, R. Sankar, K.-S. Kim, J. Kim, Y.J. Chang, Emergence of a Metal–Insulator Transition and High-Temperature Charge-Density Waves in  $\text{VSe}_2$  at the Monolayer Limit, *Nano Letters*, 18 (2018) 5432-5438.
- [38] X.-L. Feng, K. Jiang, J.-P. Hu, Kagome superconductors, *Acta Physica Sinica*, 71 (2022) 118103-118101-118103-118106.
- [39] H.N.S. Lee, H. McKinzie, D.S. Tannhauser, A. Wold, The Low-Temperature Transport Properties of  $\text{NbSe}_2$ , *Journal of Applied Physics*, 40 (1969) 602-604.
- [40] R. Delaplace, P. Molinie, D. Jerome, On the pressure dependence of a charge density wave state in 2H- $\text{TaS}_2$ , *Journal de Physique Lettres*, 37 (1976) 13-15.
- [41] L.-j. Li, Z.-a. Xu, J.-q. Shen, L.-m. Qiu, Z.-h. Gan, The effect of a charge-density wave transition on the transport properties of 2H- $\text{NbSe}_2$ , *Journal of Physics: Condensed Matter*, 17 (2005) 493-498.
- [42] L.J. Li, X.D. Zhu, Y.P. Sun, H.C. Lei, B.S. Wang, S.B. Zhang, X.B. Zhu, Z.R. Yang, W.H. Song, Superconductivity of Ni-doping 2H- $\text{TaS}_2$ , *Physica C: Superconductivity*, 470 (2010) 313-317.
- [43] N.Z. Wang, M.Z. Shi, C. Shang, F.B. Meng, L.K. Ma, X.G. Luo, X.H. Chen, Tunable superconductivity by electrochemical intercalation in  $\text{TaS}_2$ , *New Journal of Physics*, 20 (2018) 023014.

- [44] K. Wijayarathne, J. Zhao, C. Malliakas, D. Young Chung, M.G. Kanatzidis, U. Chatterjee, Spectroscopic signature of moment-dependent electron–phonon coupling in 2H-TaS<sub>2</sub>, *Journal of Materials Chemistry C*, 5 (2017) 11310-11316.
- [45] M.D. Johannes, I.I. Mazin, C.A. Howells, Fermi-surface nesting and the origin of the charge-density wave in NbSe<sub>2</sub>, *Physical Review B*, 73 (2006) 205102.
- [46] K. Wijayarathne, J. Zhao, C.D. Malliakas, D.Y. Chung, M.G. Kanatzidis, U. Chatterjee, Spectroscopic signature of the k-dependent electron-phonon coupling in 2H-TaS<sub>2</sub>, *Free radical biology & medicine*. 0891-5849, (2018).
- [47] F. Weber, S. Rosenkranz, J.P. Castellan, R. Osborn, R. Hott, R. Heid, K.P. Bohnen, T. Egami, A.H. Said, D. Reznik, Extended Phonon Collapse and the Origin of the Charge-Density Wave in 2H-NbSe<sub>2</sub>, *Physical Review Letters*, 107 (2011) 107403.
- [48] F. Weber, S. Rosenkranz, J.P. Castellan, R. Osborn, G. Karapetrov, R. Hott, R. Heid, K.P. Bohnen, A. Alatas, Electron-Phonon Coupling and the Soft Phonon Mode in TiSe<sub>2</sub>, *Physical Review Letters*, 107 (2011) 266401.
- [49] J. Zhou, J. Lin, X. Huang, Y. Zhou, Y. Chen, J. Xia, H. Wang, Y. Xie, H. Yu, J. Lei, D. Wu, F. Liu, Q. Fu, Q. Zeng, C.-H. Hsu, C. Yang, L. Lu, T. Yu, Z. Shen, H. Lin, B.I. Yakobson, Q. Liu, K. Suenaga, G. Liu, Z. Liu, A library of atomically thin metal chalcogenides, *Nature*, 556 (2018) 355-359.
- [50] X. Zhao, P. Song, C. Wang, A.C. Riis-Jensen, W. Fu, Y. Deng, D. Wan, L. Kang, S. Ning, J. Dan, T. Venkatesan, Z. Liu, W. Zhou, K.S. Thygesen, X. Luo, S.J. Pennycook, K.P. Loh, Engineering covalently bonded 2D layered materials by self-intercalation, *Nature*, 581 (2020) 171-177.
- [51] S.Z. Butler, S.M. Hollen, L. Cao, Y. Cui, J.A. Gupta, H.R. Gutiérrez, T.F. Heinz, S.S. Hong, J. Huang, A.F. Ismach, E. Johnston-Halperin, M. Kuno, V.V. Plashnitsa, R.D. Robinson, R.S. Ruoff, S. Salahuddin, J. Shan, L. Shi, M.G. Spencer, M. Terrones, W. Windl, J.E. Goldberger, Progress, Challenges, and Opportunities in Two-Dimensional Materials Beyond Graphene, *ACS Nano*, 7 (2013) 2898-2926.
- [52] S. Manzeli, D. Ovchinnikov, D. Pasquier, O.V. Yazyev, A. Kis, 2D transition metal dichalcogenides, *Nature Reviews Materials*, 2 (2017) 17033.
- [53] M. Hossain, Z. Zhao, W. Wen, X. Wang, J. Wu, L. Xie, Recent Advances in Two-Dimensional Materials with Charge Density Waves: Synthesis, Characterization and Applications, in: *Crystals*, 2017.
- [54] J. Wang, Y. Wei, H. Li, X. Huang, H. Zhang, Crystal phase control in two-dimensional materials, *Science China Chemistry*, 61 (2018) 1227-1242.

- [55] A. Ribak, R.M. Skiff, M. Mograbi, P.K. Rout, M.H. Fischer, J. Ruhman, K. Chashka, Y. Dagan, A. Kanigel, Chiral superconductivity in the alternate stacking compound 4Hb-TaS<sub>2</sub>, *Science Advances*, 6 eaax9480.
- [56] A. Achari, J. Bekaert, V. Sreepal, A. Orekhov, P. Kumaravadivel, M. Kim, N. Gauquelin, P. Balakrishna Pillai, J. Verbeeck, F.M. Peeters, A.K. Geim, M.V. Milošević, R.R. Nair, Alternating Superconducting and Charge Density Wave Monolayers within Bulk 6R-TaS<sub>2</sub>, *Nano Letters*, 22 (2022) 6268-6275.
- [57] Y. Yu, G.-H. Nam, Q. He, X.-J. Wu, K. Zhang, Z. Yang, J. Chen, Q. Ma, M. Zhao, Z. Liu, F.-R. Ran, X. Wang, H. Li, X. Huang, B. Li, Q. Xiong, Q. Zhang, Z. Liu, L. Gu, Y. Du, W. Huang, H. Zhang, High phase-purity 1T'-MoS<sub>2</sub> and 1T'-MoSe<sub>2</sub> layered crystals, *Nature Chemistry*, 10 (2018) 638-643.
- [58] C. Shang, Y.Q. Fang, Q. Zhang, N.Z. Wang, Y.F. Wang, Z. Liu, B. Lei, F.B. Meng, L.K. Ma, T. Wu, Z.F. Wang, C.G. Zeng, F.Q. Huang, Z. Sun, X.H. Chen, Superconductivity in the metastable 1T' and 1T'' phases of MoS<sub>2</sub> crystals, *Physical Review B*, 98 (2018) 184513.
- [59] A. Meetsma, G. Wiegers, R. Haange, J. De Boer, Structure of 2H-TaS<sub>2</sub>, *Acta Crystallographica Section C: Crystal Structure Communications*, 46 (1990) 1598-1599.
- [60] I. Guillamón, H. Suderow, J.G. Rodrigo, S. Vieira, P. Rodière, L. Cario, E. Navarro-Moratalla, C. Martí-Gastaldo, E. Coronado, Chiral charge order in the superconductor 2H-TaS<sub>2</sub>, *New Journal of Physics*, 13 (2011) 103020.
- [61] F.H. Yu, D.H. Ma, W.Z. Zhuo, S.Q. Liu, X.K. Wen, B. Lei, J.J. Ying, X.H. Chen, Unusual competition of superconductivity and charge-density-wave state in a compressed topological kagome metal, *Nat Commun*, 12 (2021) 3645.
- [62] Y. Yang, S. Fang, V. Fatemi, J. Ruhman, E. Navarro-Moratalla, K. Watanabe, T. Taniguchi, E. Kaxiras, P. Jarillo-Herrero, Enhanced superconductivity upon weakening of charge density wave transport in 2H-TaS<sub>2</sub> in the two-dimensional limit, *Physical Review B*, 98 (2018).
- [63] P.M.C. Rourke, A.F. Bangura, C. Proust, J. Levallois, N. Doiron-Leyraud, D. LeBoeuf, L. Taillefer, S. Adachi, M.L. Sutherland, N.E. Hussey, Fermi-surface reconstruction and two-carrier model for the Hall effect in YBa<sub>2</sub>Cu<sub>4</sub>O<sub>8</sub>, *Physical Review B*, 82 (2010) 020514.
- [64] Y. Muto, Y. Okada, N. Kobayashi, N. Toyota, M. Ikebe, INTERLAYER COUPLING STRENGTH IN SUPERCONDUCTORS 2H-TaS<sub>2</sub> AND 2H-TaS<sub>2</sub>(py)<sub>1/2</sub>, *Le Journal de Physique Colloques*, 39 (1978), 0449-1947.
- [65] L. Fang, P.Y. Zou, Y. Wang, L. Tang, Z. Xu, H. Chen, C. Dong, L. Shan, H.H. Wen, Competition of superconductivity and charge density wave order in Na<sub>x</sub>TaS<sub>2</sub> single crystals, *Science and Technology of Advanced Materials*, 6 (2005) 736-739.

- [66] L. Li, X. Deng, Z. Wang, Y. Liu, M. Abeykoon, E. Dooryhee, A. Tomic, Y. Huang, J.B. Warren, E.S. Bozin, S.J.L. Billinge, Y. Sun, Y. Zhu, G. Kotliar, C. Petrovic, Superconducting order from disorder in 2H-TaSe<sub>2-x</sub>S<sub>x</sub>, *npj Quantum Materials*, 2 (2017) 11.
- [67] K.E. Wagner, E. Morosan, Y.S. Hor, J. Tao, Y. Zhu, T. Sanders, T.M. McQueen, H.W. Zandbergen, A.J. Williams, D.V. West, R.J. Cava, Tuning the charge density wave and superconductivity in Cu<sub>x</sub>TaS<sub>2</sub>, *Physical Review B*, 78 (2008) 104520.
- [68] S. Xu, J. Gao, Z. Liu, K. Chen, P. Yang, S. Tian, C. Gong, J. Sun, M. Xue, J. Gouchi, X. Luo, Y. Sun, Y. Uwatoko, H. Lei, B. Wang, J. Cheng, Effects of disorder and hydrostatic pressure on charge density wave and superconductivity in 2H-TaS<sub>2</sub>, *Physical Review B*, 103 (2021).
- [69] P.W. Anderson, Theory of dirty superconductors, *Journal of Physics and Chemistry of Solids*, 11 (1959) 26-30.
- [70] L. Fang, Y. Wang, P.Y. Zou, L. Tang, Z. Xu, H. Chen, C. Dong, L. Shan, H.H. Wen, Fabrication and superconductivity of Na<sub>x</sub>TaS<sub>2</sub> crystals, *Physical Review B*, 72 (2005) 014534.
- [71] D.C. Freitas, P. Rodière, M.R. Osorio, E. Navarro-Moratalla, N.M. Nemes, V.G. Tissen, L. Cario, E. Coronado, M. García-Hernández, S. Vieira, M. Núñez-Regueiro, H. Suderow, Strong enhancement of superconductivity at high pressures within the charge-density-wave states of 2H-TaS<sub>2</sub> and 2H-TaSe<sub>2</sub>, *Physical Review B*, 93 (2016).
- [72] X.-M. Zhao, K. Zhang, Z.-Y. Cao, Z.-W. Zhao, V.V. Struzhkin, A.F. Goncharov, H.-K. Wang, A.G. Gavriliuk, H.-K. Mao, X.-J. Chen, Pressure tuning of the charge density wave and superconductivity in 2H-TaS<sub>2</sub>, *Physical Review B*, 101 (2020).
- [73] M. Abdel-Hafiez, X.M. Zhao, A.A. Kordyuk, Y.W. Fang, B. Pan, Z. He, C.G. Duan, J. Zhao, X.J. Chen, Enhancement of superconductivity under pressure and the magnetic phase diagram of tantalum disulfide single crystals, *Sci Rep*, 6 (2016) 31824.
- [74] J.B. Wiley, R.B. Kaner, Rapid Solid-State Precursor Synthesis of Materials, *Science*, 255 (1992) 1093-1097.
- [75] H. Schmalzried, *Solid state reactions*, (1981).
- [76] A.-M. Sapse, P.v.R. Schleyer, *Lithium chemistry: a theoretical and experimental overview*, (1995).
- [77] C.M. Julien, *Lithium intercalated compounds: Charge transfer and related properties*, *Materials Science and Engineering: R: Reports*, 40 (2003) 47-102.
- [78] J. Rodríguez-Carvajal, Recent advances in magnetic structure determination by neutron powder diffraction, *Physica B: Condensed Matter*, 192 (1993) 55-69.

- [79] X. Cui, Z. Feng, Y. Jin, Y. Cao, D. Deng, H. Chu, S. Cao, C. Dong, J. Zhang, AutoFP: a GUI for highly automated Rietveld refinement using an expert system algorithm based on FullProf, *Journal of Applied Crystallography*, 48 (2015) 1581-1586.
- [80] S.H. Lee, S.-m. Park, L.P. Lee, *Optical Methods in Studies of Olfactory System*, in: T.H. Park (Ed.) *Bioelectronic Nose: Integration of Biotechnology and Nanotechnology*, Springer Netherlands, Dordrecht, 2014, pp. 191-220.
- [81] S.C. Wilschefski, M.R. Baxter, *Inductively Coupled Plasma Mass Spectrometry: Introduction to Analytical Aspects*, *Clin Biochem Rev*, 40 (2019) 115-133.
- [82] S. Jian, K. Jürgen, *Finite-Element Modelling and Analysis of Hall Effect and Extraordinary Magnetoresistance Effect*, in: E. Farzad (Ed.) *Finite Element Analysis*, IntechOpen, Rijeka, 2012, pp. Ch. 10.
- [83] J. Chang, E. Blackburn, A.T. Holmes, N.B. Christensen, J. Larsen, J. Mesot, R. Liang, D.A. Bonn, W.N. Hardy, A. Watenphul, M.v. Zimmermann, E.M. Forgan, S.M. Hayden, Direct observation of competition between superconductivity and charge density wave order in  $\text{YBa}_2\text{Cu}_3\text{O}_{6.67}$ , *Nature Physics*, 8 (2012) 871-876.
- [84] J. Chang, E. Blackburn, O. Ivashko, A.T. Holmes, N.B. Christensen, M. Hucker, R. Liang, D.A. Bonn, W.N. Hardy, U. Rutt, M.V. Zimmermann, E.M. Forgan, S.M. Hayden, Magnetic field controlled charge density wave coupling in underdoped  $\text{YBa}_2\text{Cu}_3\text{O}_{6+x}$ , *Nat Commun*, 7 (2016) 11494.
- [85] U. Chatterjee, J. Zhao, M. Iavarone, R. Di Capua, J.P. Castellán, G. Karapetrov, C.D. Malliakas, M.G. Kanatzidis, H. Claus, J.P. Ruff, F. Weber, J. van Wezel, J.C. Campuzano, R. Osborn, M. Randeria, N. Trivedi, M.R. Norman, S. Rosenkranz, Emergence of coherence in the charge-density wave state of  $2\text{H-NbSe}_2$ , *Nat Commun*, 6 (2015) 6313.
- [86] B. Keimer, S.A. Kivelson, M.R. Norman, S. Uchida, J. Zaanen, From quantum matter to high-temperature superconductivity in copper oxides, *Nature*, 518 (2015) 179-186.
- [87] E. Morosan, H.W. Zandbergen, B.S. Dennis, J.W.G. Bos, Y. Onose, T. Klimczuk, A.P. Ramirez, N.P. Ong, R.J. Cava, Superconductivity in  $\text{Cu}_x\text{TiSe}_2$ , *Nature Physics*, 2 (2006) 544-550.
- [88] H.H. Kim, E. Lefrançois, K. Kummer, R. Fumagalli, N.B. Brookes, D. Betto, S. Nakata, M. Tortora, J. Porras, T. Loew, M.E. Barber, L. Braicovich, A.P. Mackenzie, C.W. Hicks, B. Keimer, M. Minola, M. Le Tacon, Charge Density Waves in  $\text{YBa}_2\text{Cu}_3\text{O}_{6.67}$  Probed by Resonant X-Ray Scattering under Uniaxial Compression, *Phys Rev Lett*, 126 (2021) 037002.
- [89] R. Arpaia, S. Caprara, R. Fumagalli, G. De Vecchi, Y.Y. Peng, E. Andersson, D. Betto, G.M. De Luca, N.B. Brookes, F. Lombardi, M. Salluzzo, L. Braicovich, C. Di Castro, M. Grilli,



G. Ghiringhelli, Dynamical charge density fluctuations pervading the phase diagram of a Cu-based high- $T_c$  superconductor, *Science*, 365 (2019) 906-910.

[90] H. Miao, R. Fumagalli, M. Rossi, J. Lorenzana, G. Seibold, F. Yakhou-Harris, K. Kummer, N.B. Brookes, G.D. Gu, L. Braicovich, G. Ghiringhelli, M.P.M. Dean, Formation of Incommensurate Charge Density Waves in Cuprates, *Physical Review X*, 9 (2019).

[91] S. Sachdev, B. Keimer, Quantum criticality, *Physics Today*, 64 (2011) 29-35.

[92] M. Leroux, V. Mishra, J.P.C. Ruff, H. Claus, M.P. Smylie, C. Opagiste, P. Rodiere, A. Kayani, G.D. Gu, J.M. Tranquada, W.K. Kwok, Z. Islam, U. Welp, Disorder raises the critical temperature of a cuprate superconductor, *Proc Natl Acad Sci U S A*, 116 (2019) 10691-10697.

[93] Y. Feng, J. Wang, R. Jaramillo, J. van Wezel, S. Haravifard, G. Srajer, Y. Liu, Z.A. Xu, P.B. Littlewood, T.F. Rosenbaum, Order parameter fluctuations at a buried quantum critical point, *Proceedings of the National Academy of Sciences*, 109 (2012) 7224-7229.

[94] S. Nagata, T. Aochi, T. Abe, S. Ebisu, T. Hagino, Y. Seki, K. Tsutsumi, Superconductivity in the layered compound 2H-TaS<sub>2</sub>, *Journal of Physics and Chemistry of Solids*, 53 (1992) 1259-1263.

[95] F.R. Gamble, F.J. DiSalvo, R.A. Klemm, T.H. Geballe, Superconductivity in Layered Structure Organometallic Crystals, *Science*, 168 (1970) 568.

[96] A. Lerf, F. Sernetz, W. Biberacher, R. Schöllhorn, Superconductivity in layered ternary chalcogenides A<sub>x</sub>TaS<sub>2</sub> and A<sub>x</sub>NbS<sub>2</sub> and influence of topotactic solvation, *Materials Research Bulletin*, 14 (1979) 797-805.

[97] D.C. Johnston, Ambient temperature phase relations in the system of Na<sub>1/3</sub>(H<sub>2</sub>O)<sub>y</sub>TaS<sub>2</sub> (0 < y < 2), *Materials Research Bulletin*, 17 (1982) 13-23.

[98] D.C. Johnston, S.P. Frysinger, X-ray diffraction study of Na<sub>1/3</sub>(H<sub>2</sub>O)<sub>1.5</sub>TaS<sub>2</sub>: Observation of a Hendricks-Teller disordered layer lattice, *Physical Review B*, 30 (1984) 980-984.

[99] T. Valla, A.V. Fedorov, P.D. Johnson, P.A. Glans, C. McGuinness, K.E. Smith, E.Y. Andrei, H. Berger, Quasiparticle Spectra, Charge-Density Waves, Superconductivity, and Electron-Phonon Coupling in 2H-NbSe<sub>2</sub>, *Physical Review Letters*, 92 (2004) 086401.

[100] X.D. Zhu, Y.P. Sun, X.B. Zhu, X. Luo, B.S. Wang, G. Li, Z.R. Yang, W.H. Song, J.M. Dai, Single crystal growth and characterizations of Cu<sub>0.03</sub>TaS<sub>2</sub> superconductors, *Journal of Crystal Growth*, 311 (2008) 218-221.

[101] J. Pan, C. Guo, C. Song, X. Lai, H. Li, W. Zhao, H. Zhang, G. Mu, K. Bu, T. Lin, X. Xie, M. Chen, F. Huang, Enhanced Superconductivity in Restacked TaS<sub>2</sub> Nanosheets, *J Am Chem Soc*, 139 (2017) 4623-4626.

- [102] E. Navarro-Moratalla, J.O. Island, S. Manas-Valero, E. Pinilla-Cienfuegos, A. Castellanos-Gomez, J. Querada, G. Rubio-Bollinger, L. Chirolli, J.A. Silva-Guillen, N. Agrait, G.A. Steele, F. Guinea, H.S. van der Zant, E. Coronado, Enhanced superconductivity in atomically thin TaS<sub>2</sub>, *Nat Commun*, 7 (2016) 11043.
- [103] A.H. Thompson, F.R. Gamble, R.F. Koehler, Effects of Intercalation on Electron Transport in Tantalum Disulfide, *Physical Review B*, 5 (1972) 2811-2816.
- [104] J. Peng, Z. Yu, J. Wu, Y. Zhou, Y. Guo, Z. Li, J. Zhao, C. Wu, Y. Xie, Disorder Enhanced Superconductivity toward TaS<sub>2</sub> Monolayer, *ACS Nano*, 12 (2018) 9461-9466.
- [105] J. Rodriguez-Carvajal, Collected abstract of powder diffraction meeting, Toulouse, France, 127 (1990).
- [106] W.P.F.A.M. Omloo, F. Jellinek, Intercalation compounds of alkali metals with niobium and tantalum dichalcogenides, *Journal of the Less Common Metals*, 20 (1970) 121-129.
- [107] R. Grasset, Y. Gallais, A. Sacuto, M. Cazayous, S. Manas-Valero, E. Coronado, M.A. Measson, Pressure-Induced Collapse of the Charge Density Wave and Higgs Mode Visibility in 2H-TaS<sub>2</sub>, *Phys Rev Lett*, 122 (2019) 127001.
- [108] T. Gruner, D. Jang, Z. Huesges, R. Cardoso-Gil, G.H. Fecher, M.M. Koza, O. Stockert, A.P. Mackenzie, M. Brando, C. Geibel, Charge density wave quantum critical point with strong enhancement of superconductivity, *Nature Physics*, 13 (2017) 967-972.
- [109] L. Zheng, Z. Wu, Y. Yang, L. Nie, M. Shan, K. Sun, D. Song, F. Yu, J. Li, D. Zhao, S. Li, B. Kang, Y. Zhou, K. Liu, Z. Xiang, J. Ying, Z. Wang, T. Wu, X. Chen, Emergent charge order in pressurized kagome superconductor CsV<sub>3</sub>Sb<sub>5</sub>, *Nature*, 611 (2022) 682-687.
- [110] C. Kendziora, D. Mandrus, L. Mihaly, L. Forro, Single-band model for the temperature-dependent Hall coefficient of high-T<sub>c</sub> superconductors, *Physical Review B*, 46 (1992) 14297-14300.
- [111] P.M.C. Rourke, A.F. Bangura, C. Proust, J. Levallois, N. Doiron-Leyraud, D. LeBoeuf, L. Taillefer, S. Adachi, M.L. Sutherland, N.E. Hussey, Fermi-surface reconstruction and two-carrier model for the Hall effect in YBa<sub>2</sub>Cu<sub>4</sub>O<sub>8</sub>, *Physical Review B*, 82 (2010).
- [112] N. Wang, M. Shi, C. Shang, F. Meng, L. Ma, X. Luo, X. Chen, Tunable superconductivity by electrochemical intercalation in TaS<sub>2</sub>, *New Journal of Physics*, 20 (2018).
- [113] Y. Li, Z. Wu, J. Zhou, K. Bu, C. Xu, L. Qiao, M. Li, H. Bai, J. Ma, Q. Tao, C. Cao, Y. Yin, Z.-A. Xu, Enhanced anisotropic superconductivity in the topological nodal-line semimetal In<sub>x</sub>TaS<sub>2</sub>, *Physical Review B*, 102 (2020).
- [114] A.K. Ghosh, A. Rose, H.P. Maruska, D.J. Eustace, T. Feng, Hall measurements and grain-size effects in polycrystalline silicon, *Applied Physics Letters*, 37 (1980) 544-546.

- [115] T.K. Xia, D. Stroud, Theory of the Hall coefficient of polycrystals: Application to a simple model for  $\text{La}_{2-x}\text{M}_x\text{CuO}_4$  ( $\text{M}=\text{Sr}, \text{Ba}$ ), *Phys Rev B Condens Matter*, 37 (1988) 118-122.
- [116] F. von Rohr, R. Nesper, A. Schilling, Superconductivity in rubidium-substituted  $\text{Ba}_{1-x}\text{Rb}_x\text{Ti}_2\text{Sb}_2\text{O}$ , *Physical Review B*, 89 (2014) 094505.
- [117] E.H. Brandt, Properties of the ideal Ginzburg-Landau vortex lattice, *Physical Review B*, 68 (2003).
- [118] M.H. Van Maaren, Superconductivity in tin-group Va trichalcogenides, *Physics Letters A*, 40 (1972), 0375-9601.
- [119] R.E. Schaak, T. Klimczuk, M.L. Foo, R.J. Cava, Superconductivity phase diagram of  $\text{Na}_x\text{CoO}_2 \cdot 1.3\text{H}_2\text{O}$ , *Nature*, 424 (2003) 527-529.
- [120] H. Sakurai, K. Takada, F. Izumi, R.A. Dilanian, T. Sasaki, E. Takayama-Muromachi, The role of the water molecules in novel superconductor,  $\text{Na}_{0.35}\text{CoO}_2 \cdot 1.3\text{H}_2\text{O}$ , *Physica C: Superconductivity*, 412-414 (2004) 182-186.
- [121] K. Matano, G.q. Zheng, D.P. Chen, C.T. Lin, J. Cmaidalka, R.L. Meng, C.W. Chu, NMR and NQR studies of the pairing symmetry in the superconducting state of  $\text{Na}_x\text{CoO}_2 \cdot 1.3\text{H}_2\text{O}$ , *Journal of Magnetism and Magnetic Materials*, 310 (2007) 687-689.
- [122] H. Liu, S. Huangfu, X. Zhang, H. Lin, A. Schilling, Superconductivity and charge density wave formation in lithium-intercalated  $2\text{H-TaS}_2$ , *Physical Review B*, 104 (2021).
- [123] F.R. Gamble, F.J. DiSalvo, R.A. Klemm, T.H. Geballe, Superconductivity in Layered Structure Organometallic Crystals, *Science*, 168 (1970) 568-570.
- [124] F.R. Gamble, J.H. Osiecki, M. Cais, R. Pisharody, F.J. DiSalvo, T.H. Geballe, Intercalation Complexes of Lewis Bases and Layered Sulfides: A Large Class of New Superconductors, *Science*, 174 (1971) 493-497.
- [125] N. Katayama, M. Nohara, F. Sakai, H. Takagi, Enhanced Superconducting Transition Temperature in the Water-intercalated Sulfides, *Journal of the Physical Society of Japan*, 74 (2005) 851-854.
- [126] N.F. Hinsche, K.S. Thygesen, Electron-phonon interaction and transport properties of metallic bulk and monolayer transition metal dichalcogenide  $\text{TaS}_2$ , *2D Materials*, 5 (2017) 015009.
- [127] G. Guo, W. Liang, Electronic structures of intercalation complexes of the layered compound  $2\text{H-TaS}_2$ , *Journal of Physics C: Solid State Physics*, 20 (1987) 4315.
- [128] W. Biberacher, A. Lurf, J. Besenhard, H. Möhwald, T. Butz, S. Saibene, Electrointercalation into  $2\text{H-TaS}_2$  single crystals: in situ dilatometry and superconducting properties, *Il Nuovo Cimento D*, 2 (1983) 1706-1711.

- [129] S. Gygax, W. Biberacher, A. Lerf, M. Denhoff, Superconducting parameters of a strongly anisotropic intercalated TaS<sub>2</sub> compound: K<sub>0.33</sub>(H<sub>2</sub>O)<sub>0.66</sub>TaS<sub>2</sub>, *Helvetica Physica Acta*, 55 (1983) 755-763.
- [130] P.B. Allen, W.E. Pickett, H. Krakauer, Band-theory analysis of anisotropic transport in La<sub>2</sub>CuO<sub>4</sub>-based superconductors, *Physical Review B*, 36 (1987) 3926-3929.
- [131] F.J.D. Salvo, R. Schwall, T.H. Geballe, F.R. Gamble, J.H. Osiecki, Superconductivity in Layered Compounds with Variable Interlayer Spacings, *Physical Review Letters*, 27 (1971) 310-313.
- [132] Y. Mao, Y. Fang, J. Pan, D. Wang, K. Bu, X. Che, W. Zhao, F. Huang, Synthesis, crystal structures and physical properties of A(H<sub>2</sub>O)MoS<sub>2</sub> (A = K, Rb, Cs), *Journal of Solid State Chemistry*, 279 (2019) 120937.
- [133] H.A. Graf, A. Lerf, R. Schöllhorn, A crystal structure investigation of the hydrated layered chalcogenides K<sub>x</sub>(H<sub>2</sub>O)<sub>y</sub>NbS<sub>2</sub> and K<sub>x</sub>(H<sub>2</sub>O)<sub>y</sub>TaS<sub>2</sub>, *Journal of the Less Common Metals*, 55 (1977) 213-220.
- [134] W.Z. Hu, G. Li, J. Yan, H.H. Wen, G. Wu, X.H. Chen, N.L. Wang, Optical study of the charge-density-wave mechanism in 2H-TaS<sub>2</sub> and Na<sub>x</sub>TaS<sub>2</sub>, *Physical Review B*, 76 (2007) 045103.
- [135] B.G.M. Ekoya, J. Han, J. Zhu, Y. Shan, R. Liu, L. Hu, Z.-J. Qiu, C. Cong, Molecular interactions induced collapse of charge density wave quantum states in 2H tantalum disulfide nanosheets, *Nano Research*, 16 (2023) 6960-6966.
- [136] Q. Qian, H. Ren, J. Zhou, Z. Wan, J. Zhou, X. Yan, J. Cai, P. Wang, B. Li, Z. Sofer, B. Li, X. Duan, X. Pan, Y. Huang, X. Duan, Chiral molecular intercalation superlattices, *Nature*, 606 (2022) 902-908.
- [137] B.J. Ramshaw, S.E. Sebastian, R.D. McDonald, J. Day, B.S. Tan, Z. Zhu, J.B. Betts, R. Liang, D.A. Bonn, W.N. Hardy, N. Harrison, Quasiparticle mass enhancement approaching optimal doping in a high-temperature superconductor, *Science*, 348 (2015) 317.
- [138] P.C. Canfield, S.L. Bud'ko, FeAs-Based Superconductivity: A Case Study of the Effects of Transition Metal Doping on BaFe<sub>2</sub>As<sub>2</sub>, *Annual Review of Condensed Matter Physics*, 1 (2010) 27-50.
- [139] F. Bouquet, R.A. Fisher, N.E. Phillips, D.G. Hinks, J.D. Jorgensen, Specific Heat of MgB<sub>2</sub>: Evidence for a Second Energy Gap, *Physical Review Letters*, 87 (2001).
- [140] K.-H. Müller, G. Fuchs, A. Handstein, K. Nenkov, V. Narozhnyi, D. Eckert, The upper critical field in superconducting MgB<sub>2</sub>, *Journal of alloys and compounds*, 322 (2001) L10-L13.

- [141] R. Micnas, J. Ranninger, S. Robaszkiewicz, Superconductivity in narrow-band systems with local nonretarded attractive interactions, *Reviews of Modern Physics*, 62 (1990) 113-171.
- [142] V.V. Moshchalkov, J.Y. Henry, C. Marin, J. Rossat-Mignod, J.F. Jacquot, Anisotropy of the first critical field and critical current in  $\text{YBa}_2\text{Cu}_3\text{O}_{6.9}$  single crystals, *Physica C: Superconductivity*, 175 (1991) 407-418.
- [143] L. Burlachkov, Y. Yeshurun, M. Konczykowski, F. Holtzberg, Explanation for the low-temperature behavior of  $H_{c1}$  in  $\text{YBa}_2\text{Cu}_3\text{O}_7$ , *Phys Rev B Condens Matter*, 45 (1992) 8193-8196.
- [144] L. Li, X. Deng, Z. Wang, Y. Liu, M. Abeykoon, E. Dooryhee, A. Tomic, Y. Huang, J.B. Warren, E.S. Bozin, S.J.L. Billinge, Y. Sun, Y. Zhu, G. Kotliar, C. Petrovic, Superconducting order from disorder in  $2\text{H-TaSe}_{2-x}\text{S}_x$ , *npj Quantum Materials*, 2 (2017).
- [145] M.V. Milošević, A. Perali, Emergent phenomena in multicomponent superconductivity: an introduction to the focus issue, *Superconductor Science and Technology*, 28 (2015) 060201.
- [146] M. Abdel-Hafiez, S. Aswartham, S. Wurmehl, V. Grinenko, C. Hess, S.L. Drechsler, S. Johnston, A.U.B. Wolter, B. Büchner, H. Rosner, L. Boeri, Specific heat and upper critical fields in  $\text{KFe}_2\text{As}_2$  single crystals, *Physical Review B*, 85 (2012).
- [147] J. Bekaert, S. Vercauteren, A. Aperis, L. Komendová, R. Prozorov, B. Partoens, M.V. Milošević, Anisotropic type-I superconductivity and anomalous superfluid density in  $\text{OsB}_2$ , *Physical Review B*, 94 (2016).
- [148] K. Kudo, M. Takasuga, Y. Okamoto, Z. Hiroi, M. Nohara, Giant Phonon Softening and Enhancement of Superconductivity by Phosphorus Doping of  $\text{BaNi}_2\text{As}_2$ , *Physical Review Letters*, 109 (2012).
- [149] A. Schlicht, M. Schwenker, W. Biberacher, A. Lerf, Superconducting Transition Temperature of  $2\text{H-TaS}_2$  Intercalation Compounds Determined by the Phonon Spectrum, *The Journal of Physical Chemistry B*, 105 (2001) 4867-4871.
- [150] Arushi, D. Singh, P.K. Biswas, A.D. Hillier, R.P. Singh, Unconventional superconducting properties of noncentrosymmetric  $\text{Re}_{5.5}\text{Ta}$ , *Physical Review B*, 101 (2020) 144508.
- [151] A. Lerf, Different modes and consequences of electron transfer in intercalation compounds, *Journal of Physics and Chemistry of Solids*, 65 (2004) 553-563.
- [152] J.A. Flores-Livas, R. Debord, S. Botti, A. San Miguel, M.A. Marques, S. Pailhes, Enhancing the superconducting transition temperature of  $\text{BaSi}_2$  by structural tuning, *Phys Rev Lett*, 106 (2011) 087002.
- [153] J. Guo, Y. Qi, S. Matsuishi, H. Hosono,  $T_c$  Maximum in Solid Solution of Pyrite  $\text{IrSe}_2$ - $\text{RhSe}_2$  Induced by Destabilization of Anion Dimers, *Journal of the American Chemical Society*, 134 (2012) 20001-20004.

- [154] B.J. Ramshaw, S.E. Sebastian, R.D. McDonald, J. Day, B.S. Tan, Z. Zhu, J.B. Betts, R. Liang, D.A. Bonn, W.N. Hardy, N. Harrison, Quasiparticle mass enhancement approaching optimal doping in a high- $T_c$  superconductor, *Science*, 348 (2015) 317-320.
- [155] G. Seibold, R. Arpaia, Y.Y. Peng, R. Fumagalli, L. Braicovich, C. Di Castro, M. Grilli, G.C. Ghiringhelli, S. Caprara, Strange metal behaviour from charge density fluctuations in cuprates, *Communications Physics*, 4 (2021).
- [156] W. Tabis, Y. Li, M. Le Tacon, L. Braicovich, A. Kreyssig, M. Minola, G. Della, E. Weschke, M.J. Veit, M. Ramazanoglu, A.I. Goldman, T. Schmitt, G. Ghiringhelli, N. Barisic, M.K. Chan, C.J. Dorow, G. Yu, X. Zhao, B. Keimer, M. Greven, Charge order and its connection with Fermi-liquid charge transport in a pristine high- $T_c$  cuprate, *Nat Commun*, 5 (2014) 5875.
- [157] H. Miao, G. Fabbris, R.J. Koch, D.G. Mazzone, C.S. Nelson, R. Acevedo-Esteves, G.D. Gu, Y. Li, T. Yilmaz, K. Kaznatcheev, E. Vescovo, M. Oda, T. Kurosawa, N. Momono, T. Assefa, I.K. Robinson, E.S. Bozin, J.M. Tranquada, P.D. Johnson, M.P.M. Dean, Charge density waves in cuprate superconductors beyond the critical doping, *npj Quantum Materials*, 6 (2021).
- [158] H. Polshyn, M. Yankowitz, S. Chen, Y. Zhang, K. Watanabe, T. Taniguchi, C.R. Dean, A.F. Young, Large linear-in-temperature resistivity in twisted bilayer graphene, *Nature Physics*, 15 (2019) 1011-1016.
- [159] S. Licciardello, J. Buhot, J. Lu, J. Ayres, S. Kasahara, Y. Matsuda, T. Shibauchi, N.E. Hussey, Electrical resistivity across a nematic quantum critical point, *Nature*, 567 (2019) 213-217.
- [160] N. Doiron-Leyraud, P. Auban-Senzier, S. René de Cotret, C. Bourbonnais, D. Jérôme, K. Bechgaard, L. Taillefer, Correlation between linear resistivity and  $T_c$  in the Bechgaard salts and the pnictide superconductor  $Ba(Fe_{1-x}Co_x)_2As_2$ , *Physical Review B*, 80 (2009).
- [161] K. Lee, B.Y. Wang, M. Osada, B.H. Goodge, T.C. Wang, Y. Lee, S. Harvey, W.J. Kim, Y. Yu, C. Murthy, S. Raghu, L.F. Kourkoutis, H.Y. Hwang, Linear-in-temperature resistivity for optimally superconducting  $(Nd,Sr)NiO_2$ , *Nature*, 619 (2023) 288-292.
- [162] D.S. Yanan Zhang, Yanen Huang, Hualei Sun, Mengwu Huo, Zhaoyang Shan, Kaixin Ye, Zihan Yang, Rui Li, Michael Smidman, Meng Wang, Lin Jiao, Huiqiu Yuan, High-temperature superconductivity with zero-resistance and strange metal behaviour in  $La_3Ni_2O_7$ , (2023). ([doi.org/10.48550/arXiv.2307.14819](https://doi.org/10.48550/arXiv.2307.14819)).
- [163] M. Gurvitch, A.T. Fiory, Resistivity of  $La_{1.825}Sr_{0.175}CuO_4$  and  $YBa_2Cu_3O_7$  to 1100 K: Absence of saturation and its implications, *Phys Rev Lett*, 59 (1987) 1337-1340.

- [164] R. Cooper, Y. Wang, B. Vignolle, O. Lipscombe, S. Hayden, Y. Tanabe, T. Adachi, Y. Koike, M. Nohara, H. Takagi, Anomalous criticality in the electrical resistivity of  $\text{La}_{2-x}\text{Sr}_x\text{CuO}_4$ , *Science*, 323 (2009) 603-607.
- [165] K. Jin, N.P. Butch, K. Kirshenbaum, J. Paglione, R.L. Greene, Link between spin fluctuations and electron pairing in copper oxide superconductors, *Nature*, 476 (2011) 73-75.
- [166] J. Yuan, Q. Chen, K. Jiang, Z. Feng, Z. Lin, H. Yu, G. He, J. Zhang, X. Jiang, X. Zhang, Y. Shi, Y. Zhang, M. Qin, Z.G. Cheng, N. Tamura, Y.F. Yang, T. Xiang, J. Hu, I. Takeuchi, K. Jin, Z. Zhao, Scaling of the strange-metal scattering in unconventional superconductors, *Nature*, 602 (2022) 431-436.
- [167] C. Di Castro, Revival of Charge Density Waves and Charge Density Fluctuations in Cuprate High-Temperature Superconductors, in: *Condensed Matter*, 2020.
- [168] S.A. Kivelson, I.P. Bindloss, E. Fradkin, V. Oganesyan, J. Tranquada, A. Kapitulnik, C. Howald, How to detect fluctuating stripes in the high-temperature superconductors, *Reviews of Modern Physics*, 75 (2003) 1201.
- [169] R. Comin, A. Damascelli, Resonant X-Ray Scattering Studies of Charge Order in Cuprates, *Annual Review of Condensed Matter Physics*, 7 (2016) 369-405.
- [170] D.H. Torchinsky, F. Mahmood, A.T. Bollinger, I. Bozovic, N. Gedik, Fluctuating charge-density waves in a cuprate superconductor, *Nat Mater*, 12 (2013) 387-391.
- [171] J.L. Jaewon Choi, Abhishek Nag, Jonathan Pellicciari, Hannah Robarts, Charles C. Tam, Andrew Walters, Stefano Agrestini, Mirian García-Fernández, Dongjoon Song, Hiroshi Eisaki, Steven Johnston, Riccardo Comin, Hong Ding, Ke-Jin Zhou, Stripe Symmetry of Short-range Charge Density Waves in Cuprate Superconductors. (doi.org/10.48550/arXiv.2301.07637)
- [172] R. Arpaia, E. Andersson, E. Trabeldo, T. Bauch, F. Lombardi, Probing the phase diagram of cuprates with  $\text{YBa}_2\text{Cu}_4\text{O}_7$  thin films and nanowires, *Physical Review Materials*, 2 (2018) 024804.
- [173] D. Lin, S. Li, J. Wen, H. Berger, L. Forro, H. Zhou, S. Jia, T. Taniguchi, K. Watanabe, X. Xi, M.S. Bahrmy, Patterns and driving forces of dimensionality-dependent charge density waves in 2H-type transition metal dichalcogenides, *Nat Commun*, 11 (2020) 2406.
- [174] R.V. Coleman, B. Giambattista, P.K. Hansma, A. Johnson, W.W. McNairy, C.G. Slough, Scanning tunnelling microscopy of charge-density waves in transition metal chalcogenides, *Advances in Physics*, 37 (1988) 559-644.
- [175] M. Liao, H. Wang, Y. Zhu, R. Shang, M. Rafique, L. Yang, H. Zhang, D. Zhang, Q.K. Xue, Coexistence of resistance oscillations and the anomalous metal phase in a lithium intercalated  $\text{TiSe}_2$  superconductor, *Nat Commun*, 12 (2021) 5342.

- [176] K. Cho, M. Kończykowski, S. Teknowijoyo, M.A. Tanatar, J. Guss, P.B. Gartin, J.M. Wilde, A. Kreyssig, R.J. McQueeney, A.I. Goldman, V. Mishra, P.J. Hirschfeld, R. Prozorov, Using controlled disorder to probe the interplay between charge order and superconductivity in NbSe<sub>2</sub>, *Nature Communications*, 9 (2018).
- [177] J. Joshi, H.M. Hill, S. Chowdhury, C.D. Malliakas, F. Tavazza, U. Chatterjee, A.R. Hight Walker, P.M. Vora, Short-range charge density wave order in 2H-TaS<sub>2</sub>, *Physical Review B*, 99 (2019) 245144.
- [178] D. Zhang, Y. Wu, Y.-H. Su, M.-C. Hsu, C. Ó Coileáin, J. Cho, M. Choi, B.S. Chun, Y. Guo, C.-R. Chang, Charge density waves and degenerate modes in exfoliated monolayer 2H-TaS<sub>2</sub>, *IUCrJ*, 7 (2020) 913-919.
- [179] H. Liu, S. Huangfu, H. Lin, X. Zhang, A. Schilling, Superconductivity in hydrated Li<sub>x</sub>(H<sub>2</sub>O)<sub>y</sub>TaS<sub>2</sub>, *Journal of Materials Chemistry C*, 11 (2023) 3553-3561.
- [180] J. Shi, X. Wang, S. Zhang, L. Xiao, Y. Huan, Y. Gong, Z. Zhang, Y. Li, X. Zhou, M. Hong, Q. Fang, Q. Zhang, X. Liu, L. Gu, Z. Liu, Y. Zhang, Two-dimensional metallic tantalum disulfide as a hydrogen evolution catalyst, *Nature Communications*, 8 (2017) 958.
- [181] E. Kovalska, P.K. Roy, N. Antonatos, V. Mazanek, M. Vesely, B. Wu, Z. Sofer, Photocatalytic activity of twist-angle stacked 2D TaS<sub>2</sub>, *npj 2D Materials and Applications*, 5 (2021) 68.
- [182] M. Zhang, Y. He, D. Yan, H. Xu, A. Wang, Z. Chen, S. Wang, H. Luo, K. Yan, Multifunctional 2H-TaS<sub>2</sub> nanoflakes for efficient supercapacitors and electrocatalytic evolution of hydrogen and oxygen, *Nanoscale*, 11 (2019) 22255-22260.
- [183] Y. Feng, S. Gong, E. Du, X. Chen, R. Qi, K. Yu, Z. Zhu, 3R TaS<sub>2</sub> Surpasses the Corresponding 1T and 2H Phases for the Hydrogen Evolution Reaction, *The Journal of Physical Chemistry C*, 122 (2018) 2382-2390.
- [184] X. Zhang, R. Shu, H. Liu, A. Elskova, P.O.Å. Persson, A. Schilling, F.O. von Rohr, P. Eklund, Suppression of the transition to superconductivity in crystal/glass high-entropy alloy nanocomposites, *Communications Physics*, 5 (2022) 282.
- [185] H.S. Røising, G. Wagner, M. Roig, A.T. Rømer, B.M. Andersen, Heat capacity double transitions in time-reversal symmetry broken superconductors, *Physical Review B*, 106 (2022) 174518.
- [186] S.M. Thomas, C. Stevens, F.B. Santos, S.S. Fender, E.D. Bauer, F. Ronning, J.D. Thompson, A. Huxley, P.F.S. Rosa, Spatially inhomogeneous superconductivity in UTe<sub>2</sub>, *Physical Review B*, 104 (2021).



- [187] E. Piatti, G. Prando, M. Meinero, C. Tresca, M. Putti, S. Roddaro, G. Lamura, T. Shiroka, P. Carretta, G. Profeta, D. Daghero, R.S. Gonnelli, Superconductivity induced by gate-driven hydrogen intercalation in the charge-density-wave compound 1T-TiSe<sub>2</sub>, *Communications Physics*, 6 (2023).
- [188] B. Hildebrand, T. Jaouen, C. Didiot, E. Razzoli, G. Monney, M.L. Mottas, A. Ubaldini, H. Berger, C. Barreteau, H. Beck, D.R. Bowler, P. Aebi, Short-range phase coherence and origin of the 1T-TiSe<sub>2</sub> charge density wave, *Physical Review B*, 93 (2016).
- [189] J. Joshi, H.M. Hill, S. Chowdhury, C.D. Malliakas, F. Tavazza, U. Chatterjee, A.R. Hight Walker, P.M. Vora, Short-range charge density wave order in 2H-TaS<sub>2</sub>, *Physical Review B*, 99 (2019).
- [190] U.P. Sahoo, A. Mukherjee, P.K. Sahoo, Short-Range Charge Density Wave and Bandgap Modulation by Au-Implanted Defects in TiSe<sub>2</sub>, *ACS Applied Electronic Materials*, 4 (2022) 3428-3434.
- [191] J. Zhao, K. Wijayarathne, A. Butler, J. Yang, C.D. Malliakas, D.Y. Chung, D. Louca, M.G. Kanatzidis, J. van Wezel, U. Chatterjee, Orbital selectivity causing anisotropy and particle-hole asymmetry in the charge density wave gap of 2H-TaS<sub>2</sub>, *Physical Review B*, 96 (2017).
- [192] A.T. Divya Rawat, Ajay Soni, Symmetry breaking and structure instability in ultra-thin 2H-TaS<sub>2</sub> across charge density wave transition. (doi.org/10.48550/arXiv.2307.08418).
- [193] S. Pal, S.B. Roy, Understanding the magnetic response of the Quantum Spin Liquid compound 1T-TaS<sub>2</sub>, *Physica B: Condensed Matter*, 643 (2022) 414121.
- [194] B. Xiao, F. Hébert, G. Batrouni, R.T. Scalettar, Competition between phase separation and spin density wave or charge density wave order: Role of long-range interactions, *Physical Review B*, 99 (2019).
- [195] N. Harrison, C.H. Mielke, A.D. Christianson, J.S. Brooks, M. Tokumoto, Field-Induced Dynamic Diamagnetism in a Charge-Density-Wave System, *Physical Review Letters*, 86 (2001) 1586-1589.
- [196] K.Y. Chen, N.N. Wang, Q.W. Yin, Y.H. Gu, K. Jiang, Z.J. Tu, C.S. Gong, Y. Uwatoko, J.P. Sun, H.C. Lei, J.P. Hu, J.G. Cheng, Double Superconducting Dome and Triple Enhancement of T<sub>c</sub> in the Kagome Superconductor CsV<sub>3</sub>Sb<sub>5</sub> under High Pressure, *Physical Review Letters*, 126 (2021) 247001.
- [197] T.-H. Park, O.P. Uzoh, H.-Y. Choi, Maximal superconductivity in proximity to the charge density wave quantum critical point in Cu<sub>x</sub>TiSe<sub>2</sub>, *Physical Review B*, 104 (2021).
- [198] J.A.N. Bruin, H. Sakai, R.S. Perry, A.P. Mackenzie, Similarity of Scattering Rates in Metals Showing T-Linear Resistivity, *Science*, 339 (2013) 804-807.

[199] A. Rosch, Interplay of disorder and spin fluctuations in the resistivity near a quantum critical point, *Physical Review Letters*, 82 (1999) 4280.

## Publication List

### **Superconductivity in hydrated $\text{Li}_x(\text{H}_2\text{O})_y\text{TaS}_2$**

Huanlong Liu, S Huangfu, H Lin, X Zhang, A Schilling  
Journal of Materials Chemistry C 11 (10), 3553-3561

### **Suppression of the transition to superconductivity in crystal/glass high-entropy alloy nanocomposites**

Xiaofu Zhang, Rui Shu, Huanlong Liu, Anna Elsukova, Per OÅ Persson, Andreas Schilling, Fabian O von Rohr, Per Eklund  
Communications Physics 5 (1), 282

### **Two-gap to single-gap superconducting transition on a honeycomb lattice in $\text{Ca}_{1-x}\text{Al}_x\text{Si}$**

Dorota I Walicka, Zurab Guguchia, Jorge Lago, Olivier Blacque, KeYuan Ma, Huanlong Liu, Rustem Khasanov, Fabian O von Rohr  
Physical review research 3 (3), 033192

### **Superconductivity and charge density wave formation in lithium-intercalated $2H\text{-TaS}_2$**

Huanlong Liu, S Huangfu, X Zhang, H Lin, A Schilling  
Physical Review B 104 (6), 064511

### **Physical properties of amorphous molybdenum silicide films for single-photon detectors**

X Zhang, I Charaev, Huanlong Liu, TX Zhou, D Zhu, KK Berggren, A Schilling  
Superconductor Science and Technology 34 (9), 095003

### **Size dependent nature of the magnetic-field driven superconductor-to-insulator quantum-phase transitions**

Xiaofu Zhang, Adriana E Lita, HuanLong Liu, Varun B Verma, Q Zhou, Sae Woo Nam, Andreas Schilling  
Communications Physics 4 (1), 100

### **Strong suppression of the resistivity near the superconducting transition in narrow microbridges in external magnetic fields**

Xiaofu Zhang, Adriana E Lita, Konstantin Smirnov, HuanLong Liu, Dong Zhu, Varun B Verma, Sae Woo Nam, Andreas Schilling  
Physical Review B 101 (6), 060508

## **Curriculum Vitae**

### Personal Data

Name: Huanlong Liu

Date of birth: 27, October, 1990

Birthplace: Anhui, China

Address: Heerenschürlistrasse 25, 8051 Zürich

### Education

2006-2011: Anhui Lingbi Normal School & Anhui Lingbi No.1 Middle School

2011-2015: North University of China

2015-2018: University of Shanghai, China

2018-present: University of Zurich, Switzerland

## Acknowledgments

Time flies and five years go by in a flash. At this moment, I still have memories of my first visit to Zurich as if it were yesterday. Looking back, I have met many people and experienced many events over the years. They have all contributed in one way or another to the completion of this thesis.

First and foremost, I would like to express the tremendous gratitude to my supervisor Prof. Andreas Schilling for his trust and tolerance and for giving me the opportunity to complete my PhD study. His help, guidance and advice are greatly appreciated. Thank you again for giving me the freedom and continued support to choose a topic that interests me and to complete this thesis. Meanwhile, I would like to thank Dr. Xiaofu Zhang, Dr. Hai Lin, Prof. Fabian von Rohr and Prof. Marta Gibert for giving me a lot of support in my experimental measurements and discussions, of which they were or are members of my PhD committee.

Then, I am very grateful to Dr. Shangxiong Huangfu and Dr. Qisi Wang for giving me some of their ideas to enrich my scientific contributions. The members of the mechanical and electronic workshops supported my research by repairing our machines. I would especially like to thank Reto Maier, Daniel Florin, and David Wolf. I express gratitude to Monika Rollin and Brigitte Freund for their great supportive service and help in my life.

Next, I would like to thank all my colleagues, Stefan Siegrist, Dr. Ilya Charaev, Dong Zhu, and Noah Brugger for their help and support. I have many happy memories shared with them during my PhD study. They are Dr. Daniel Destraz, Dr. Lakshimi Das, Dr. López Paz Sara, Dr. Walicka Dorota, Witteveen Catherine, Dong Zhu, Dr. Jonathan Spring, and Simon Johr. I would also like to thank Chong Huang and Dr. Hang Chen for their help with the X-ray measurements, Dr. Olivier Blacque and Prof. Bernhard Spingler for the single crystal measurements and Dr. Jérémie Teyssier and Dr. Volodymyr Multian for the Raman measurements.

Last but not least, I would like to thank my family for their encourage and support. Thanks to all the people who gave me help and good memories in Switzerland.